Scrape-off layer ion temperature measurements on MAST by retarding field energy analyser

Thesis submitted in accordance with the requirements of the University of Liverpool for the degree of Doctor in Philosophy by

Sarah Dawn Elmore

August 2013

Abstract

Knowledge of the ion temperature (T_i) is important for tokamaks when determining plasma parameters from diagnostics which require knowledge of the ion and electron temperature (T_e) and also because ions of high energy could damage plasma facing components by sputtering on high power devices. In the tokamak edge there are limited data for T_i, however the few existing measurements show that, beyond the confined plasma, $T_i > T_e$, unlike in the confined plasma where ions and electrons are thermal coupled. A measurement technique using retarding field energy analyser (RFEA) probes to measure T_i has been implemented on the Mega Amp Spherical Tokamak (MAST) to allow measurements at the midplane and also at the divertor target which are two key areas in the scrape-off layer (SOL) plasma.

Measurements in ohmic low confinement (L-mode) plasma discharges have shown that $T_i \approx 2T_e$ at the midplane, while $T_i \approx T_e$ at the target. Additionally heated L-mode plasmas have shown that T_i can be greater than T_e at the divertor target. In inter-ELM high confinement (H-mode) plasmas, T_i is often found to be higher than T_e, with extremes in high power plasmas of $T_i/T_e \approx 3$ at the target. Initial measurements of the temperature of ions released by an average ELM show that T_i reduces with distance from the strike point at the target. The measured upper limit on T_i in an average ELM reduces from 60 eV to 30 eV over ~ 4 cm radially at the target. Measurements made by the target RFEA during ELMs show peak $T_i \sim 35$ eV compared to peak T_e measurements by Langmuir probes of ~ 25 eV. These initial measurements of T_i agree with modelling of the ELM evolution in the SOL which show hot electrons arriving at the target before the remaining particles released by the ELM.

Measurements by RFEA probes are subject to a correction in the presence of parallel flows in the SOL. It has been found from modelling of the MAST SOL that measurements made by the target RFEA should be multiplied by a correction factor between 0.65 and 0.7. Although this reduces the ratios measured of T_i/T_e, measurements in inter-ELM H-mode and additionally heated L-mode plasmas would still show $T_i > T_e$ at the target. In ohmic L-mode plasmas, however, the reduction in T_i would mean $T_i < T_e$.

Contents

List of Figures

List of Tables

Acknowledgements

The work presented here would not be possible without the guidance and assistance of many people who are gratefully acknowledged here. I would like to thank both my supervisors, Andrew Kirk and James Bradley, for their direction, assistance and valuable advice throughout the PhD and writing of the thesis.

I would also like to thank many people from CCFE who have contributed to this work, particularly Robert Stephen and Stuart Bray who have designed and developed the electronics for the RFEA probes, including numerous repairs. Rob Gaffka's ideas and assistance were invaluable in the design and installation of the DSF probe, along with the help of Ian Fitzgerald in the drawing office. Many thanks to Patrick Tamain for the initial design and ideas for the RFEA probes and also extensive advice on the probes. I am also grateful to Martin Kočan for his expert advice on all things RFEA and to Jamie Gunn for useful discussions. Scott Allan has been a great help with the installation and operation of the probes. I would like to thank the rest of the Divertor-SOL group on MAST, Geoff Fishpool for advice and assistance, and James Harrison for imparting some of his great knowledge of the MAST SOL and diagnostics. Andrew Thornton deserves a special mention for excellent session leading during my experiments, useful advice and assistance, and particularly for putting up with being on panic speed dial through the later part of the PhD. Further thanks goes to Eva Havlícková for patiently explaining how to use SOLF1D. I would like to thank all of the MAST Team who have helped me over the last four years to complete this work, it has been a pleasure working with them all.

On a personal note I would like to thank Richard Lake, Matthew Leyland and Nick Walkden for making my time as a student at CCFE enjoyable and whose humour has helped to get me through the last months of writing. Also many hanks to Caely Beecham and Edwina Vernon for their positive thinking and encouragement to get back to work. My deepest thanks go to my parents, without whose support and encouragement this work would never have been completed, and to Stuart and Helen for their support and encouragement through all the stages of work. Equal thanks goes to Stuart Henderson whose support and patience, particularly during the writing of this thesis, has been invaluable.

Declaration

I declare that the work presented in this thesis, other than contributions cited or acknowledged in the text, is my own.

Sarah Elmore, August 2013.

Chapter 1

Introduction

1.1 Introduction

For the majority of the 20th century fossil fuels have been the main choice for electricity production. However with diminishing reserves and increasing energy demands from a growing and developing world population alternative energy sources are necessary [1]. Nuclear fusion is one of the options being researched which can potentially provide large scale energy production without the issues associated with fossil fuels, such as CO_2 emission and limited fuel reserves. Nuclear fusion also has the advantage of no long-lived radioactive waste unlike current nuclear fission power stations.

To harness the energy from nuclear fusion reactions, ions and electrons must be confined for a sufficient time for the fuel ions and electrons to collide [2]. Two main approaches for confining nuclear fusion fuel are either by inertial confinement fusion (ICF) [3], which uses lasers or particle beams to heat frozen fuel pellets, or magnetic confinement fusion (MCF) [4]. MCF uses magnetic fields to confine fusion fuel in the form of a plasma, allowing reactions to occur when the plasma is adequately heated. Magnetic confinement can be achieved in several types of devices including stellarators [5], which use complex coil configurations to confine the plasma in steady state, and tokamaks [2, 6] which are pulsed devices. The work in this thesis will focus on tokamaks.

The large temperatures required for fusion, ~ 30 keV, mean that it is impractical to contain the plasma purely by a close fitting material. The magnetic fields used to confine the plasma hold the bulk plasma away from the walls of the tokamak. Due to perpendicular diffusion of ions and electrons at the edge of the plasma, some particles will still come into contact with first wall components of the tokamak. These plasma-surface interactions form an important part of nuclear fusion research since there is a risk to both the machine and the fusion plasma.

Characterising the boundary plasma and how these particles carry energy to plasma facing components is particularly important for providing information for future devices which will have higher power exhaust [7]. Hot particles in the edge

plasma will not only damage plasma facing components but also risk contaminating the core plasma with the resulting impurities [8, 9]. This problem can be reduced by maximising the temperature gradient between the confined plasma which must remain hot enough for fusion, and the point at which particles reach material surfaces. This complicated transport of particles and energy can be investigated by making measurements at positions of the edge plasma.

The Mega Amp Spherical Tokamak (MAST) [10] is well suited to making such measurements, in this instance of the ion temperature (T_i), due to its extensive diagnostic capabilities. The remote wall in MAST allows radially scanned measurements at the midplane via a reciprocating probe (RP) [11]. A further diagnostic facility positioned in the outer divertor target, the Divertor Science Facility (DSF) [12], allows the use of probes protruding into the edge plasma to make measurements of ions before they reach plasma facing target materials. This is possible in MAST due to the low heat flux at the divertor target [13]. These diagnostic facilities allow measurements at key locations for potential damage in future devices and allow studies of T_i as it changes along the edge plasma.

The relationship between the ion and electron temperature (T_e) at these two edge plasma positions is important for comparison to edge plasma modelling and when predicting the power exhaust in future large scale devices. The limited number of existing measurements made of T_i have shown that although in the core plasma $T_i = T_e$, in the edge plasma it can be found that $T_i \geq T_e$ [14]. Hotter ions have implications for existing diagnostics used to determine the power to plasma facing targets and also edge modelling which are often required to define T_i/T_e. This area of study will form the basis of the work presented in this thesis.

1.2 Thermonuclear fusion

Nuclear fusion is the process by which light atomic nuclei fuse together to form heavier nuclei and release large amounts of energy, known as the binding energy. The most favourable fusion reaction for use in producing thermonuclear fusion energy is between deuterium and tritium, since this reaction has the largest cross-section, particularly at lower kinetic energies. When deuterium, D, and tritium, T, fuse they produce an α-particle and a neutron with 17.6 MeV of excess energy, see equation 1.1 [2].

$$ {}^{2}_{1}D + {}^{3}_{1}T \rightarrow {}^{4}_{2}He(3.5MeV) + n(14.1MeV) \tag{1.1} $$

In order to use these fusion reactions as an efficient energy source the energy produced must outweigh the energy required to make the reactions happen. This can be achieved by allowing particles to overcome the coulomb barrier and fuse together. The best way to create fusion reactions in a reactor is to produce a plasma with a high density of $\sim 10^{20}$ m^{-3} and particle energies of ~ 30 keV. In

order to achieve these temperatures at this density, auxiliary heating is necessary to initiate fusion reactions. For the energy to be cost effective the plasma must ignite so that the energy produced by the fusion reactions compensates for the energy needed to produce the reactions.

Ignition is dependent on the confinement time, τ_E, of the plasma, which is the time for the thermal energy contained in the plasma to escape. In order for the α-particle heating to produce a sustained burn, τ_E needs to exceed several seconds [2]. When this is achieved the energy from the neutron produced in the fusion reaction can be extracted for production of electricity by conventional methods without the plasma requiring additional heating. The Lawson Criterion gives the requirements for igniting a fusion plasma, see equation 1.2 [2].

$$nT\tau_E > 10^{21} keV m^{-3} s \tag{1.2}$$

where n is the plasma density and T is the temperature.

1.3 The tokamak

A tokamak is a torus shaped device used in magnetic confinement fusion and originally proposed in the 1950s by Russian physicists [6]. A schematic of a tokamak can be seen in figure 1.1. A tokamak plasma is contained in a vacuum vessel, but held away from the material walls by the confining magnetic fields. The principle confining magnetic field, the toroidal field (B_ϕ), is generated by toroidal magnetic field coils outside the vacuum vessel. Confining the plasma by this field alone leaves the plasma susceptible to an instability known as the kink mode which results in a loss of confinement [15]. Since the tokamak vacuum vessel is the shape of a torus, the toroidal field coils are closely spaced on the inside of the vessel compared to the outside, causing the toroidal field strength to vary radially across the tokamak. The combination of this gradient in the magnetic field and the curvature of the toroidal field around the torus produces a drift of particles in the plasma, acting in opposite directions for the ions and electrons. The resulting charge separation across the top and bottom of the tokamak produces an electric field which, when combined with the external toroidal field, causes a radial ExB drift out of the confined plasma. To remove this problem an additional field is applied to create a resultant helical field which connects the top and the bottom of the tokamak, preventing any charge separation. The additional field is in the poloidal direction and is produced by driving a current through the plasma in the toroidal direction by the transformer action. The combination of both the poloidal and toroidal fields gives the helical field of a tokamak which confines the plasma and stops charge separation and therefore the particles drifting out of the confined region.

The number of times a field line must go around the tokamak toroidally (m) in order to return to the same poloidal position, i.e one poloidal revolution (n), is

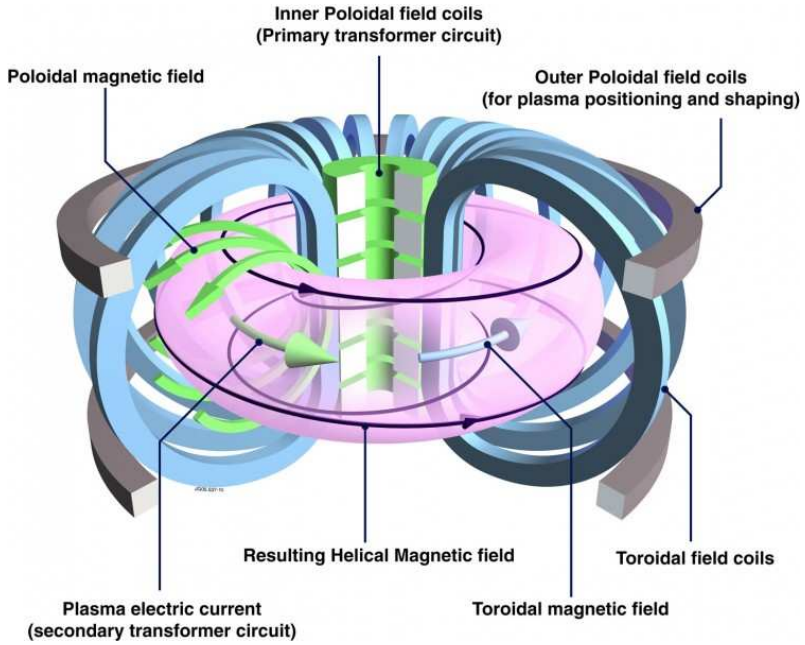

Figure 1.1: Schematic of a tokamak showing the magnetic coils and fields required to confine the tokamak plasma.

referred to as the safety factor, q, which determines the stability of the plasma. The definition for the safety factor is shown in equation 1.3 where a is the minor radius of the plasma, R is the major radius (see figure 1.2), B_ϕ is the toroidal magnetic field and B_θ is the poloidal magnetic field.

$$q = \frac{m}{n} = \frac{aB_\phi}{RB_\theta} \tag{1.3}$$

The plasma current which produces the poloidal magnetic field also serves as a form of ohmic heating for the plasma. Existing tokamak devices can achieve plasma currents of several MAs. For tokamaks which produce the plasma current by means of a transformer, the device is a pulsed plasma system. Plasma resistivity reduces with increased plasma temperature, since $\eta \propto T^{-3/2}$, which restricts the plasma current to only heating a tokamak plasma to temperatures of a few keV. Since these temperatures are not sufficient for a reasonable probability of fusion reactions, auxiliary heating is implemented on most tokamak reactors in the form of neutral particle beams or electromagnetic waves.

In a tokamak the magnetic field holds the plasma against the force of the plasma pressure. The force balance between the magnetic field, plasma current and pressure gradients can be found by considering the conservation of momentum. This gives the steady state expression shown in equation 1.4, with $\mathbf{j}$ the current density, $\mathbf{B}$ the magnetic field and P the plasma pressure.

$$\mathbf{j} \times \mathbf{B} = \nabla P \tag{1.4}$$

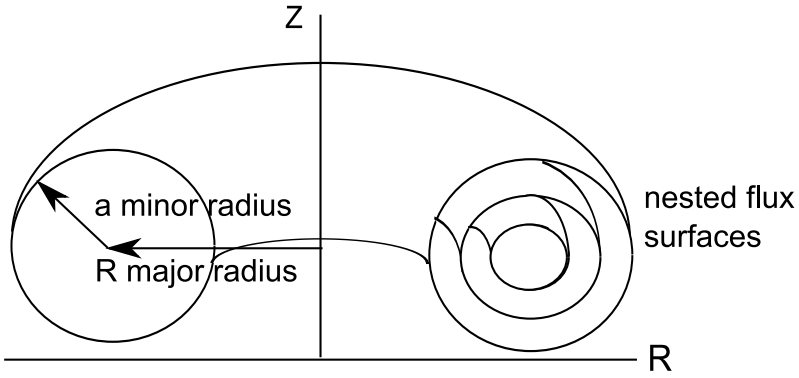

Figure 1.2: The nested flux surfaces of constant pressure which form in a tokamak.

This implies that the plasma current density and magnetic fields lie in surfaces of constant plasma pressure, on what is known as nested flux surfaces (see figure 1.2).

Particles in a confined tokamak plasma tend to follow the closed magnetic field lines, however some will diffuse outwards across the field lines and can reach the surfaces of the inner vacuum vessel wall. These particles interact with the first wall of the tokamak and cause impurities to enter the core plasma, diluting the plasma fuel and degrading the plasma performance. Additional problems arise when large heat fluxes interact with material walls because they can cause damage to plasma facing components of the vessel. The two main methods to control the interaction between the plasma and the vacuum vessel in tokamaks are limiters and divertors.

A limiter is the simplest way to separate the plasma from the vacuum vessel wall by inserting a solid material, either poloidally or toroidally, which will intercept the plasma. The field lines which are broken by the limiter material are deemed open field lines and those which do not intercept the limiter are called closed field lines. The outermost flux surface with closed field lines is termed the last closed flux surface (LCFS) and the region of open field lines is termed the scrape-off layer (SOL). By considering cross-field transport purely due to diffusion, the radial size of the SOL is found by:

$$\lambda_{SOL} = \sqrt{\frac{D_\perp L_\parallel}{c_s}} \tag{1.5}$$

where $D_\perp$ is the radial diffusion coefficient, $L_\parallel$ is the connection length which is half the distance along the SOL between the points where field lines intersect material surfaces, and c_s is the plasma sound speed, $c_s = \sqrt{\frac{T_i+T_e}{m_i}}$. For example if $T_i = T_e = 30$ eV, $L_\parallel = 25$ m and $D_\perp = 1$ m^{2}s^{-1} then $\lambda_{SOL} \approx 2.2$ cm.

Limiters, although simple, prove problematic for future devices since, due to the relative thinness of the SOL, the heat load interacting with the limiters are large and deposited over a small area, leading to potentially very high erosion of the limiter material. Additionally, since the region of plasma-surface interaction is near to the core plasma, the impurities coming from the limiter surface have a high probability of entering the core plasma. The other option is to use a divertor which has several

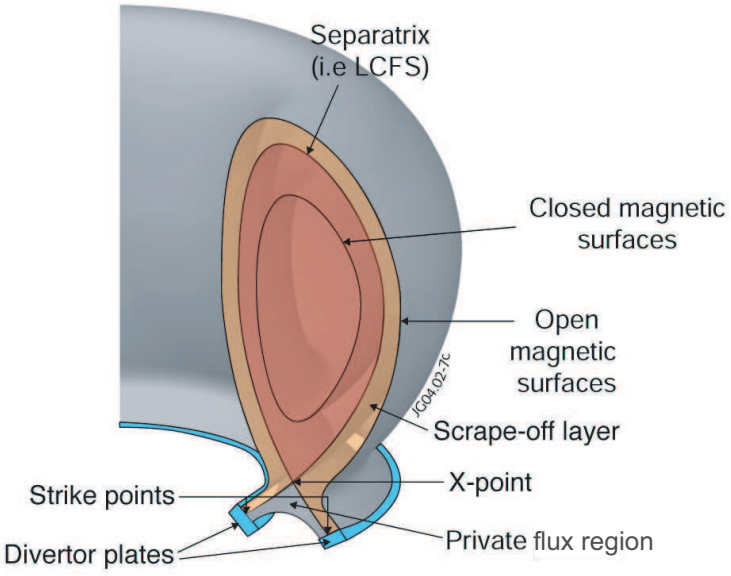

Figure 1.3: Schematic of the poloidal divertor configuration.

advantages over the limiter and will be expanded on in the following section.

1.3.1 Divertors

Tokamak divertors can be formed either toroidally or poloidally, however it is most common to use poloidal divertors, which is shown in figure 1.3. The divertor configuration is formed by the use of an extra coil in the divertor which carries a current in the same direction as the plasma current. These two currents cause a null in the poloidal magnetic field which is termed the 'X-point'. The magnetic flux surface passing through the X-point is termed the separatrix or as with the limiter configuration the LCFS. Outside of the separatrix the field lines are open and intersect plasma facing materials called divertor targets, making up the divertor SOL through which the plasma exhaust is managed. The open field lines which connect the X-point to the divertor targets are known as the strike points, with the SOL region between the strike points termed the 'private flux region', see figure 1.3.

The divertor tokamak configuration has a number of benefits; the main one being the ability to extend the distance hot particles from the core need to travel before they come into contact with divertor surfaces. Particles travelling along field lines move rapidly and this is known as parallel transport. In the divertor configuration the X-point field null means that there is a region of low poloidal field where the field lines will loop around the X-point many times in the toroidal direction. This looping increases the length of the field lines before they reach the divertor and therefore the parallel transport time is increased. This also increases the cooling before particles interact with divertor surfaces. Other benefits of the divertor include the ability to use this transport mechanism to remove helium ash, which has thermalized after fusion reactions, from the plasma so that it doesn't

contribute to core plasma impurities. The ability to control the power exhaust to the material surface by controlling the width of the strike point using divertor magnetic coils is also possible in this configuration. This creates the possibility of spreading the heat load over the target surfaces.

One of the most important advances due to the use of divertors in tokamaks is access to a higher confinement regime of the plasma, termed the H-mode. In the 1980s this operational regime was discovered in the ASDEX tokamak at IPP, Garching [16]. To enter H-mode from the standard operational mode (low-confinement regime or L-mode) the plasma must be above a critical power. This can be achieved on a number of machines, including MAST, in an ohmic plasma however in some plasma scenarios it is necessary to use auxiliary heating power. The critical power at which the H-mode transition occurs varies from machine to machine. H-mode is characterised by an increase in the temperature and density of the confined plasma through a doubling of the confinement time. Experimentally it can be identified by a decrease in visible emission from the edge plasma (D_α signals) and an increase in core density.

Unfortunately due to high pressure at the edge in this higher confinement regime an instability is triggered; the edge localised mode (ELM). These instabilities are explosions of hot, fast particles which are released into the SOL due to a build up of pressure at the edge of the plasma. They cause a transient increase in particle and energy flux to the divertor and plasma facing materials. Type III ELMs are small frequent ELM bursts which occur when the plasma resistivity is high. Type I ELMs are larger and occur at a lower frequency to type III ELMs. Type I ELMs are pressure driven and occur when the pressure reaches the stability limit. On MAST in H-mode we typically see type III ELMs at lower neutral beam heating which change to type I ELMs as the neutral beam heating is increased.

ELMs pose a large challenge to fusion research since these instabilities can cause significant damage to plasma facing components, particularly in future devices since the deposited ELM energy will be higher in higher power devices such as ITER [17]. Since it is the energy of ions, characterised by temperature, which will cause the most damage to plasma facing components, the ELM ion temperature will be investigated as part of this work.

1.3.2 Spherical tokamaks

Most tokamaks in operation since the development of the concept are conventional tokamaks of large aspect ratio, A = R/a, see figure 1.4. Spherical tokamaks were developed from an idea to use a tighter aspect ratio to improve on the β limit [18]. The β limit in tokamaks is set by the kink mode instability which is triggered by excessive plasma current [2]. A simple description of the kink mode is when the plasma deviates from the normal toroidal circle and folds in on itself. The plasma is unstable to these kink modes when q at the edge falls below 2. The β or stability

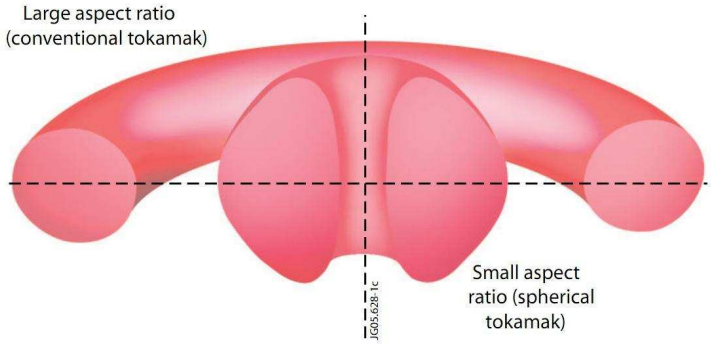

Figure 1.4: A schematic of a conventional tokamak of high aspect ratio compared to a spherical tokamak of low aspect ratio, courtesy of the JET image database.

limit can be linked to the plasma current by equation 1.6, where β_T is toroidal beta, I_P is the plasma current and B_ϕ is the toroidal magnetic field.

$$\beta_T \leq 3.5 \frac{I_P}{aB_\phi} \tag{1.6}$$

Equation 1.6 can be written in terms of q at the plasma edge (q_a) and therefore $\beta \propto \frac{1}{Aq_a}$ where A is the aspect ratio [2, 18]. This shows that by decreasing the aspect ratio the beta limit can be increased. Spherical tokamaks have low aspect ratios of 1.2 - 1.3 which is significantly lower than conventional tokamaks such as JET which has an aspect ratio of ~ 3.

The improved beta limit in spherical tokamaks (ST) results in a further advantage since the toroidal magnetic field required to confine the plasma is lower than in a conventional plasma. This allows STs to operate with a similar poloidal field to a conventional tokamak but with significantly reduced toroidal field strength. The variation of this toroidal field is also larger across the plasma radius than conventional tokamaks since the dependence of the magnetic field strength is 1/R and the major radius is smaller. Due to the ratio of the poloidal and toroidal fields, STs have a steeper pitch angle on the outside (outboard side) of the tokamak compared to that on the inside (inboard side). The shallow pitch angle on the inboard side confines particles to spend a longer time on this side of the tokamak plasma. The inboard side of the tokamak is a region of increased stability known as the good curvature region since here the centrifugal force acts against the pressure gradient to stabilise it. In contrast the outboard side is known as a region of bad curvature since here both the centrifugal force and the pressure gradient act to move particles out of confinement. The changing pitch angle is also stabilising since it increases q at the edge. Due to the compact size of STs there are disadvantages to the design; particularly the lack of protection for the centre column such as neutron shielding, since the plasma is much closer to the centre column than in conventional devices. The size also means that the area of the inner divertor leg which is in contact with divertor target plates is small, leading to large heat fluxes over a small

Table 1.1: Key MAST operational parameters [10, 22].

Parameter	Value
Plasma current	1 MA
Major radius	0.85 m
Minor radius	0.65 m
Toroidal field	0.55 T (@ 0.7 m)
Discharge length	0.5 s
NBI heating power	5 MW
Core electron temperature T_e	0.5-2 keV
Core electron density n_e	1 - 3 x 10^{19} m^{-3}
Plasma volume	10 m^3
Vessel volume	50 m^3
Aspect Ratio	1.3
Elongation (κ)	$1.6 \leq \kappa \leq 2.5$
Triangularity (δ)	$\delta \leq 0.5$

area which could be damaging in power plant scale STs.

The first ST was built in Culham in 1990 called the Small Tight Aspect Ratio Tokamak (START). START operated until 1999, in this time setting a record beta of $\beta = 40\%$ [19]. Following from this success a second ST was built at Culham, the Mega Amp Spherical Tokamak (MAST) which has been in operation since 1999 and will be the tokamak on which this work is based. Other STs exist around the world, MAST is one of the biggest two; the other is the National Spherical Torus Experiment (NSTX) in the Princeton Plasma Physics Laboratory, Princeton, USA [20, 21].

1.4 The Mega Amp Spherical Tokamak

The Mega Amp Spherical Tokamak (MAST) is based at Culham Centre for Fusion Energy (CCFE) in Abingdon, Oxfordshire. It is a mid sized tokamak whose design is similar to its predecessor, START. Both are spherical tokamaks without close fitting vacuum vessels. The vessel is 4.4 m high and 4 m in diameter. The central solenoid and toroidal field coils are constructed around the outside of the vacuum vessel whilst the poloidal field coils are inside the vessel. The toroidal field is produced by twelve toroidal field coils evenly spaced around the machine. The toroidal coils, poloidal coils and the central solenoid are water cooled to dissipate heating in the coils. A typical pulse length is between 0.5 and 0.6 s, which is limited by the finite inductive flux generated by ramping the current in the central solenoid, magnetohydrodynamic (MHD) and vertical instabilities [2]. On a normal operational day MAST can discharge around 4 plasma pulses per hour. MAST has two neutral beam injector (NBI) sources, as auxiliary heating, located at South West and South sectors of the vessel, see figure 1.5. A list of the key MAST machine parameters can be seen in table 1.1 [10, 22].

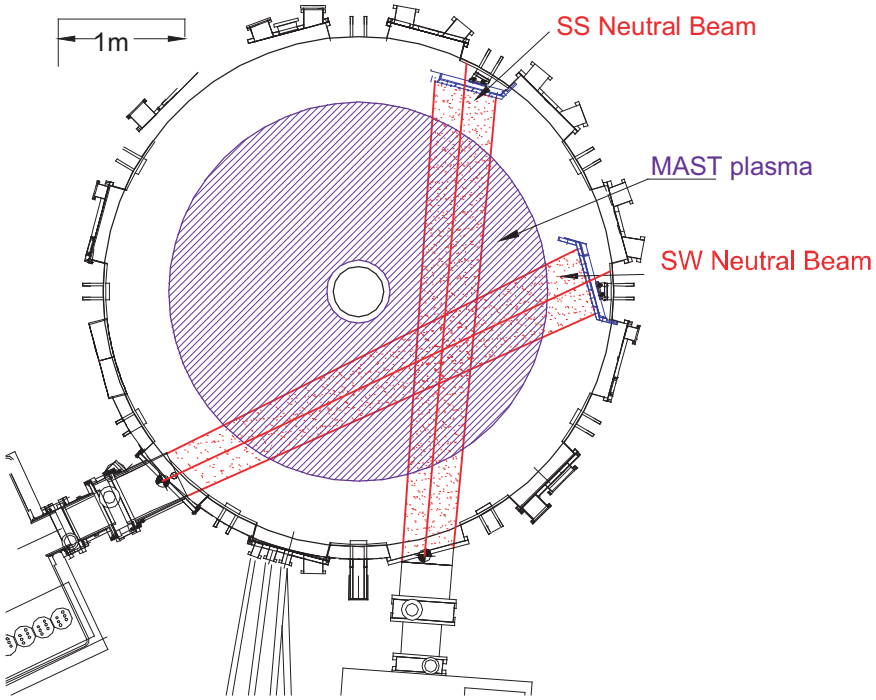

Figure 1.5: Aerial view of the MAST machine showing the position of the South West and South neutrals beams.

MAST plasmas can be operated in two magnetic configurations, either with a single null (SN) or two x-points in double null (DN) configuration. Single null plasmas have either a lower x-point with strike points only on the lower divertor targets (lower single null (LSN)) or upper single null (USN) with strike points only at the upper divertor targets. There are two configurations with DN plasmas, the two magnetic null points can either be on the same flux surface, these are connected double nulls (CDN), or there can be two separate nulls which are referred to as disconnected double nulls (DDN), see figure 1.6. Typically the inner divertor leg sits on the extremes of the centre column while the outer leg sweeps across the

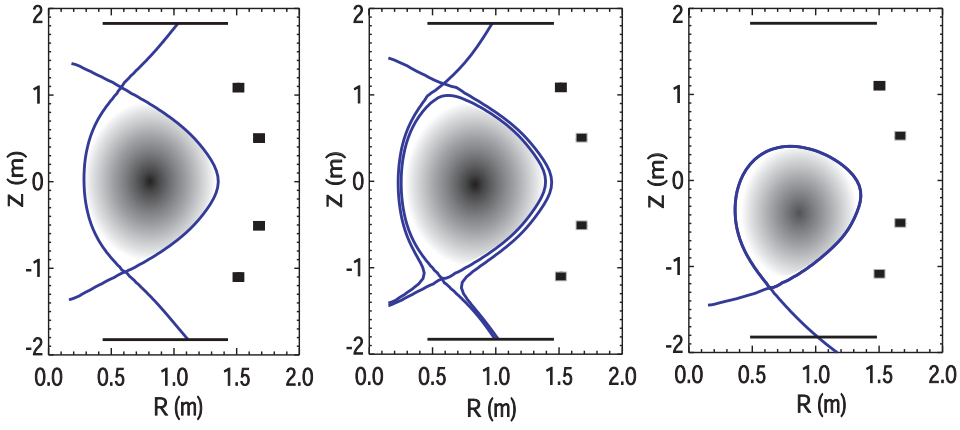

Figure 1.6: Magnetic configurations possible in the MAST tokamak: connected double null (CDN), disconnected double null (DDN) and lower single null (LSN).

divertor target plates during a discharge due to the change in magnetic flux from the sweeping solenoid current. The strike point is the part of the plasma edge which is in contact with the divertor target plates. The outer strike point in MAST moves typically at 1 ms^{-1} during a plasma discharge.

The current MAST divertor is toroidally symmetric made from 48 individual graphite elements with a gap between each. To protect the divertor target elements from incident heat flux on sharp edges the tiles have an incline of 4° toroidally [23]. This causes shadowing on the low side of the tile facing the incoming plasma at the divertor, which typically is incident at $\sim 9°$ to horizontal, but can vary from plasma to plasma and during discharges.

1.5 Edge diagnostics

1.5.1 Langmuir probes

Langmuir probes (LP) are one of the simplest plasma diagnostics which measure the electron temperature (T_e) and ion saturation current density (j_{sat}) of the plasma local to the probe surface. It is a simply designed electric probe consisting of a conducting material which is in contact with the plasma [24].

Measurements are made by biasing the probe to voltages less than the plasma potential and then sweeping the voltage to positive values whilst recording the current arriving at the probe. When a sufficiently negative bias is applied all electrons are repelled and the current measured at the probe is purely an ion current, known as the ion saturation current, $I_{i,sat}$. When a sufficiently positive bias is applied, all ions will be repelled giving a purely electron current, called the electron saturation current, $I_{e,sat}$. Generally it is the region between the ion saturation current and the plasma potential of the I-V characteristic which is of interest [25].

Langmuir probes are heavily used to diagnose the edge of tokamaks, either as probes which reciprocate into the plasma edge upstream, or stationary in divertors or limiters. Since they allow measurements of T_e and also a determination of the density of the SOL plasma they are useful diagnostics, however they are unable to measure the ion temperature. Without an equivalent T_i measurement the electron density (n_e) measurements will be inaccurate since normally for determination of n_e it is assumed that $T_i = T_e$, however this is not always the case in the SOL plasma where LP measurements are made.

MAST has Langmuir probes installed in the divertor at both the inner and outer divertor target plates with a radial spacing of 1 cm. In the outer divertor there are 92 probes in arrays along the radius of the divertor with resolution of 6-9 mm in three toroidal locations. In the inner divertor there are about 100 probes in one toroidal location. At any given time only 384 probes from the upper and lower divertors can be operated due to the restriction on available amplifiers and digitisers. 16 Langmuir probes are attached to each amplifier, with each probe being

sampled every millisecond. As well as the swept voltage configuration to give T_e, j_{sat} and therefore n_e measurements, the probes can be operated in a mode which measures only the ion saturation current, $I_{i,sat}$, as a function of time without the need of voltage sweeping. In this mode j_{sat} can be measured continuously from an individual probe at 1 MHz giving 1 μs time resolution compared to profiles of T_e and j_{sat} which are available every 1.04 ms.

1.5.2 Infra-red (IR) thermography

Infra-red (IR) thermography is a technique which is used to determine the heat flux to plasma facing components. It is used most widely to determine the heat loads and fluxes to divertor surfaces in physics studies. The infra-red camera measures the intensity of light emitted from the divertor targets as a photon flux which can be used to calculate the temperature and therefore the power arriving at the divertor targets [26].

MAST has two IR cameras, a long wave camera (LWIR), covering the wavelength range 7.6 - 9.0 μm, and a medium wave camera (MWIR), covering the wavelength range 2.5 - 5.0 μm, which can be set to view either the lower or upper divertors. The cameras are mounted outside the vacuum vessel and view the divertor target plates through vacuum windows on the machine. The cameras are usually set up to view the inner and outer divertor strike points of the upper and lower divertor. When the view is of the total strike point it can be used to measure the total power arriving at the divertor. The frame rate of the medium wave camera which is usually viewing the lower divertor is 315 Hz with a spatial resolution of 5 mm. The long wave camera which is usually viewing the upper divertor but has also been used on the lower divertor has a frame rate of 880 Hz and a spatial resolution of 7 mm.

1.5.3 Thomson scattering system

Thomson scattering (TS) can be used in plasmas to determine the temperature and density as a radial profile across the core plasma. To perform Thomson scattering measurements a high power laser is sent through the plasma. This causes the free electrons in the plasma to emit dipole radiation due to the oscillating electric field produced by the laser. The collected light from the laser is a broadened line centred on the laser waveform. The width of the broadening is related to the random thermal motion of the electrons and therefore can be used to determine the temperature of the plasma. The scattered light can be used to determine the density by calculating the area under the Thomson scattering spectrum [27, 28].

MAST has two Thomson scattering laser systems, each at a different wavelength. The ruby laser system can be used once per plasma discharge and gives 300 spatial points across the plasma radius. The second system is a Nd:YAG system, using neodymium-doped yttrium aluminium garnet as the laser medium, with a time resolution of 4.2 ms and 130 spatial points [29]. The Nd:YAG laser system can also

be operated in burst mode where a succession of up to 8 lasers can be fired with spacing of down to 5 μs and repeated every 33 ms throughout a plasma discharge. The Thomson scattering collection lens system is made up of two parts, one for the core and one for the edge of the plasma. The edge system provides an additional 16 data points from 1.29 m to 1.45 m radius.

1.5.4 Edge plasma diagnostics for T_i measurements

As early as 1980 measurements of the ion temperature at the edge plasma of a tokamak were attempted [30] using a surface collection probe based on finite gyro radii. Although this method allowed T_i to be measured in the high field limiter tokamak, TFR 600 [30], in order to use the same diagnostic in lower field edge of tokamaks, such as ASDEX, would mean reduced transmission of ions making the measurements difficult and noisy.

A well used method for measuring ion temperatures is charge exchange recombination spectroscopy (CXRS). This process involves a neutral fuel atom in the plasma transferring its electron to an impurity ion. The subsequent emission from the impurity ion allows the temperature to be determined from the Doppler width. CXRS has been used on a number of tokamaks; JT-60U [31], TEXTOR-94 [32] and ASDEX Upgrade [33]. CXRS is a reliable method for measuring ion temperatures in the core plasma however into the SOL the measured temperature of the impurity ions is not likely to represent the fuel ions, for example deuterium. In the SOL the impurities measured are not fully ionised and therefore are unlikely to be in thermal equilibrium with the deuterium ions in the SOL.

An electric probe was used to measure ion energies in the CASTOR tokamak [34]. It is an adaption of a Langmuir probe, called the segmented tunnel probe (STP), which benefits from the ability to measure both ion and electron temperatures simultaneously. A complication with use of STPs is that in order to calibrate the measurements it is necessary to have a 2-dimensional PIC code to obtain a fitting formula.

1.5.5 Edge T_i measurements by RFEA

Of the types of electrical ion energy analysers, the retarding field energy analyser is the most simple and successful for use in the SOL. One of the earliest uses of RFEAs in tokamaks was in 1986 by Wan et al [35] who used a multi-functional edge probe which included a retarding field energy analyser to diagnose the limiter shadow plasma in the Alcator C tokamak. The RFEA element of the edge probe measured energy distributions of both the ions and electrons which closely matched the expected distributions, however due to the inclusion of both a Langmuir probe and a calorimeter, the probe is perturbing to edge plasma. There were also measurements of ion energy and temperatures in the DITE tokamak, the first of which used a combined RFEA and E $\times$ B probe by Matthews (1984) [36]. Both probe types were

used to measure the ion temperature simultaneously which allowed a comparison of the two probes. The E × B probe has the benefit of measuring T_i continuously through a plasma discharge however the data is noisy and fluctuations were observed in the measured temperature even for relatively stable plasma discharges. On the other hand the RFEA probe only measured T_i around every 15-20 ms but produced data which is consistent with a Maxwellian plasma as expected. Further measurements with an RFEA have been made by Pitts (1991) [37] in the DITE tokamak to allow comparison of theoretical models of the SOL.

A retarding field energy analyser was developed for use on the SINP tokamak to measure ion temperatures in order to find the dependence of T_i on the safety factor, q [38]. The RFEA design is a two grid design unlike the RFEAs used more recently on tokamaks such as JET [39] and Tore Supra [14]. The first grid is left at the floating potential as an electron repeller, the second is the discriminator used to retard the ions and finally the collector plate is biased negatively. One problem with this configuration is that there is not a grid to repel secondary electrons which are released from the collector surface due to ion bombardment; this secondary electron emission can result in a stray positive collector current which can overestimate T_i.

An RFEA was used in the JET plasma boundary to measure ion energies [39]. This was one of the first attempts to include an RFEA in a large tokamak which meant further issues had to be addressed such as the length of time the probe could be exposed to the edge of the plasma. In JET the RFEA was installed on the reciprocating probe to allow periodic insertion into the plasma boundary for brief intervals. The probe has been used to attempt measurements of the ion temperature at the edge of JET during off normal events such as ELMs [17]. Unfortunately the probe was not equipped to sweep the voltage of the discriminating grid on the timescale of an ELM, a few 100 μs [40], so alternatively the RFEA was operated at a fixed voltage to select ions of energies above a given threshold. In order to obtain estimates of the ion temperature from the experimental data, comparisons have to be made with expectations from a transient model describing the loss of energy and particles by parallel transport out of the ELM [17].

Kočan et al [14] measured both ion and electron temperatures during an ohmic density scan using a retarding field energy analyser based on the probe originally used in JET by Pitts et al [39]. Instrumental effects of the RFEA and the influence on measured ion temperatures were investigated in Tore Supra [41]. The RFEA probe used by Kočan et al [41] has been tested on MAST to measure the ion temperature in the SOL [42] and it is on this design that the MAST RFEAs are based.

Measurements of transients such as ELMs and filaments from turbulent inter-ELM and L-mode plasmas have been measured by RFEA in the ASDEX-Upgrade SOL. First ELM measurements gave an estimate of $T_{i,ELM}$ determined by comparing the currents at the slit plate and the collector plate of the RFEA for different grid voltages [43]. Further ELM measurements have been made of type I, type

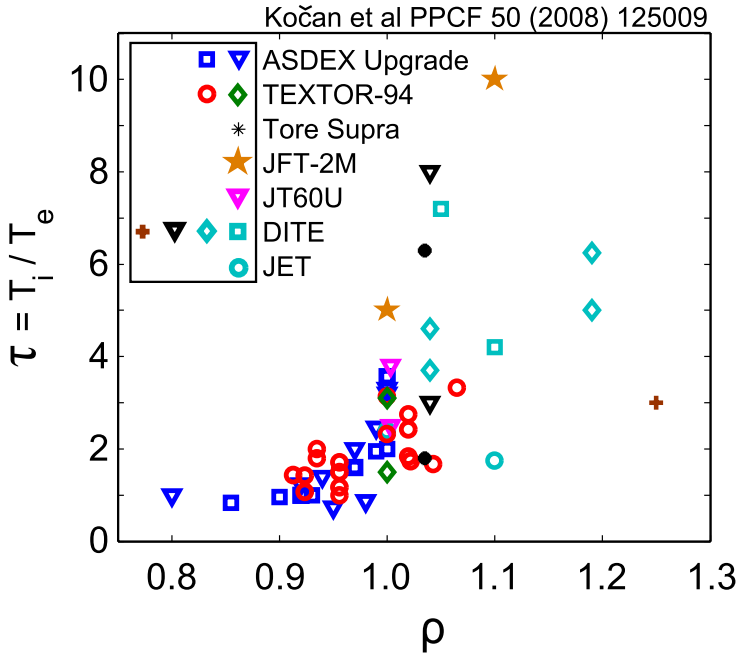

Figure 1.7: Measurements of ion to electron temperature ratio in various tokamaks [14].

III and mitigated ELMs by an averaging technique [44, 45]. Measurements on ASDEX-Upgrade of turbulent filaments in L-mode [46] and in inter-ELM H-mode [47] by RFEA have shown filaments of higher temperatures than the background ion temperatures in the SOL. An RFEA is installed on the Alcator C-Mod tokamak which has been used to make measurements of the ion temperature [48]. The most notable design feature of this RFEA is it's ability to survive high heat fluxes of > 100 MW/m^2 and make measurements up to the LCFS in the Alcator C-Mod tokamak.

From the measurements of ion and electron temperatures at the edge of fusion plasmas it has been found that $T_i \geq T_e$ at the midplane [14]. Figure 1.7 [14] is a compilation of measurements of the ion to electron temperature ratio, τ, in ohmic and heated L-mode plasmas from a range of different fusion devices, where measurements have been made by probes or CXRS. The ratio of T_i to T_e, $\tau = T_i/T_e$, has been plotted as a function of $\rho = r/a$, where $\rho = 1$ is the LCFS and it can be seen that the ratio can increase with distance into the SOL. In the SOL T_i/T_e is always found to be greater than unity ($T_i/T_e = 1.5 \rightarrow 10$) which confirms that assuming $T_i = T_e$ is unlikely to be an accurate assumption in the SOL of many fusion devices.

1.6 Motivation for study

The edge plasma is an important interface between the hot core plasma and material surfaces of the tokamak vessel which needs to be understood. High energy ions at the plasma edge can cause damage to plasma facing materials in a tokamak by erosion which means materials must be regularly replaced and also the resulting impurities

will degrade the core plasma performance. One of the main targets of tokamak edge physics research is to understand and characterise energy fluxes to the divertor and plasma facing components in tokamaks in order to understand potential damage suffered by divertor targets and impurity contamination. There has been significant previous work with electrostatic probes either on material surfaces and in the edge of the plasma however these have mainly measured T_e. Since it is more complicated to make measurements of the ion temperature and energy there is little data available in the SOL.

In the absence of data for the ion temperature it is assumed that $T_i = T_e$ when deducing such values as the electron density, n_e, and power to divertor, P_{div}, from Langmuir probe data using j_{sat} measurements. This assumption needs investigating since the few measurements which have been made in the SOL at the midplane of tokamaks has given T_i/T_e to be between 1.5 and 10 [14] and this can lead to the overestimation of n_e by over a factor of 2 [49].

Measuring the ion temperature is also important because it is the energy, characterised by temperature, of the ions which determines the level of damage on materials in the first wall and divertor of future devices. The physical sputtering yield of a material increases strongly with energy and will degrade material surfaces of tokamak vessels [24]. Measuring T_i will also give an indication of the amount of heat convected to the plasma facing components.

The purpose of this thesis is to study ion temperatures with the use of advanced Retarding Field Energy Analysers (RFEA) probes in the SOL which have been designed and implemented on MAST as part of the project. Two RFEA probes have been installed on MAST to allow simultaneous measurements of T_i both at the midplane via the reciprocating probe and at the divertor via the Divertor Science Facility. T_i will be ascertained in a variety of plasma modes; including L-mode, H-mode and during ELMs, as a function of distance from the separatrix. The data acquired for T_i will be compared to T_e data taken in the SOL by target Langmuir probes and the Thomson scattering system at the midplane in order to determine which mechanisms control the ratio of T_i to T_e.

Chapter 2

Divertor and scrape-off layer physics

2.1 The scrape-off layer

As noted in section 1.3 the scrape-off layer (SOL) is the region of unconfined plasma beyond the last closed flux surface (LCFS) where the field lines intercept material surfaces. MAST is a divertor tokamak with a divertor SOL formed by means of additional magnetic coils to divert the edge plasma towards the target plates, for more details refer to section 1.3.1. The scrape-off layer manages the exhaust of particles and energy from the main confined plasma to the divertor target plates and this area is important to understand because it affects the performance of the confined plasma. Also the plasma arriving at the material targets must be managed since it has the potential to cause damage. The following sections will explore divertor SOLs, modelling of the SOL and also diagnostics used in the SOL which will give useful comparisons to the measurements of T_i made by RFEA.

2.2 Divertor operating regimes

The divertor SOL operates in different regimes where, dependent on the SOL collisionality, ν^*_{SOL}, (given by equation 2.1 where λ_{eeii} is the mean free path of electrons and ions; n_u is the upstream density; and L is the connection length), different mechanisms control the exhaust of power through the SOL.

$$\nu^*_{SOL} = \frac{L}{\lambda_{eeii}} \approx \frac{10^{-16} n_u L}{T^2} \tag{2.1}$$

At low or moderate densities the temperatures at the divertor are sufficiently high so that volumetric processes and frictional forces are negligible and the plasma is attached to the target. For attached plasmas a distinction between two regimes can be made based on the presence of temperature gradients along the SOL, $\nabla_\parallel T$; namely the *sheath-limited regime*, where no temperature gradients exist, and the

conduction-limited regime. At higher densities a detached divertor regime can be reached which is a beneficial regime for tokamak devices of large power exhaust since more power is lost from the SOL by radiation instead of depositing on the divetor targets. These three regimes will be explored in the following section.

2.2.1 Sheath-limited regime

At low upstream SOL collisionalities, $\nu^*_{SOL} < 10$, the SOL plasma is in the sheath-limited regime. This SOL regime is characterised by the following properties [24]:

1. There are no temperature gradients along the length of the SOL, parallel to the magnetic field, i.e $\nabla_{\|} \mathrm{T}_{e,i} \approx 0$.

2. The only particle source for the SOL is cross-field transport from the main plasma.

3. The electrostatic sheath at the divertor targets act as the only particle and heat sinks. Recycling at the divertor target is at moderate levels since the upstream density is low.

4. Volumetric recombination and neutral friction forces are small enough to be ignored.

These simple conditions for the sheath-limited SOL mean that it can be well approximated by the two point model of the SOL which will be considered in detail later [24]. For the same reason the sheath-limited regime is known as the *simple scrape-off layer*. The absence of strong recycling at the divertor targets and the result of no charge exchange along the SOL leads to the constant temperatures along the SOL. This is because both these processes lead to cooling of ions and electrons along the length of the SOL. If the temperature along the SOL is constant, as in this simple regime, the only heat removal before the plasma facing components at the divertor is the sheath, hence the term *sheath-limited*. This regime is the worst operational regime for a tokamak because the temperatures are not reduced before the divertor targets, leading to potentially large amounts of sputtering in high power devices.

2.2.2 Conduction limited regime

In contrast to the sheath-limited or simple SOL, the conduction limited regime has temperature gradients parallel to magnetic field lines. The temperature gradients are always negative from the upstream SOL to the target which has obvious benefits for the divertor surfaces. In order for these temperature gradients to be sustained the dominant heat transfer must be conduction instead of convection, as in the simple SOL, and hence the term *conduction limited regime*. For the conduction limited regime, unlike the sheath-limited regime where the majority of particles enter the

SOL upstream of the targets, there is a strong particle source close to the targets due to recycling, therefore the main heat transfer is conduction. It also follows that in order to transfer the heat, there must be temperature gradients along the SOL.

In a tokamak SOL, the particle source at the target is neutral recycling. The recycling rate is related to the particle flux at the target and therefore this is linked to the upstream density. In order to control the SOL regime between the sheath-limited to conduction-limited, the upstream density can be used as the control parameter.

2.2.3 Detachment

The detached regime is a beneficial regime for tokamak operation and a key regime for future devices such as ITER because it can be used to reduce the heat flux to the divertor target. By increasing the upstream density the target temperature can be reduced to the point where volume recombination and ion-neutral friction drag on the parallel plasma flow becomes important, reducing the target density and effectively *detaching the plasma from the targets* [24]. In this regime large parallel pressure gradients are seen resulting in the low plasma power and ion flux to the targets [50]. Detached plasmas are characterised by the following:

1. Increased radiative power at the divertor targets.
2. Parallel pressure gradients along the SOL.
3. Low target temperatures and low target densities resulting in a drop in ion saturation currents at the target.
4. Reduction of power and particle fluxes to the target.

As previously mentioned, these divertor regimes can be reached by changing the upstream density. The divertor regime of a tokamak SOL can be seen by the relationship between the density upstream and at the target, see figure 2.1 for the relation between n_u and n_t.

As the density is increased upstream, the SOL changes from the sheath-limited or simple SOL to the conduction limited or complex SOL. In the conduction limited regime the ion flux to the divertor target scales roughly as $\Gamma_t \propto n_u^2$, but as the density is further increased the flux to the target reaches the *roll-over* and the plasma detaches from the target. This behaviour has been seen on JET and other devices. An example of JET can be seen in figure 2.2 [51].

2.3 Ion to electron temperature ratio

Although it is expected in the confined plasma that $T_i = T_e$ because ions and electrons are in thermal equilibrium, due to high collisionalities, this is not always the case beyond the LCFS of the plasma. It has been found that the ratio $\tau =$

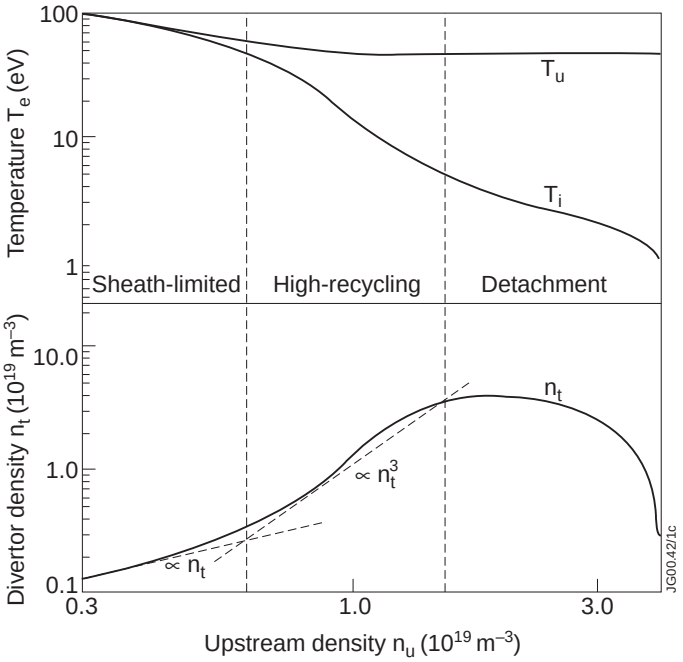

Figure 2.1: Upstream density plotted against the target density and temperature showing the different regimes of the divertor SOL courtesy of the JET image database.

T_i/T_e is greater than 1 in the SOL [14, 52] and there are several reasons why this would occur. The most important reason arises due to the difference in mobility between ions and electrons. Due to the higher mobility of electrons, they will cool more quickly as they stream along open field lines away from the confined plasma towards the targets which act as plasma sinks. This creates an electric field between the ions and electrons which slightly accelerates the ions causing extra heating and increasing the tendency for $T_i > T_e$ since, whilst the electrons cool in travelling to the targets, the ions retain more of their thermal energy. This can be seen by treating the ion and electron power channels separately. The power entering the SOL by ions, q^i, and electrons, q^e, by cross-field conduction and convection is assumed to be equal so that $q^i_{in} = q^e_{in}$. If it is assumed that equipartition collisions are negligible, $T_i \neq T_e$ is possible in the SOL. Then in the case:

$$\begin{aligned} q^e_{in} &= q^e_{se} \\ q^i_{in} &= q^i_{se} \end{aligned} \tag{2.2}$$

where *se* represents at the sheath edge, it follows [24]:

$$q^e_{se} = 5.5kT_e\Gamma_{se} = \left(\frac{5}{2}kT_i + \frac{1}{2}m_ic_s^2\right)\Gamma_{se} = q^i_{se} \tag{2.3}$$

where k is Boltzmann's constant and Γ_{se} is the power flux at the sheath edge. This gives $\tau = T_i/T_e = 5/3$, so we may expect $\tau \geq 2$ [24] and this is seen in a number of devices [14].

There is a further reason why ion temperatures greater than electrons tempera-

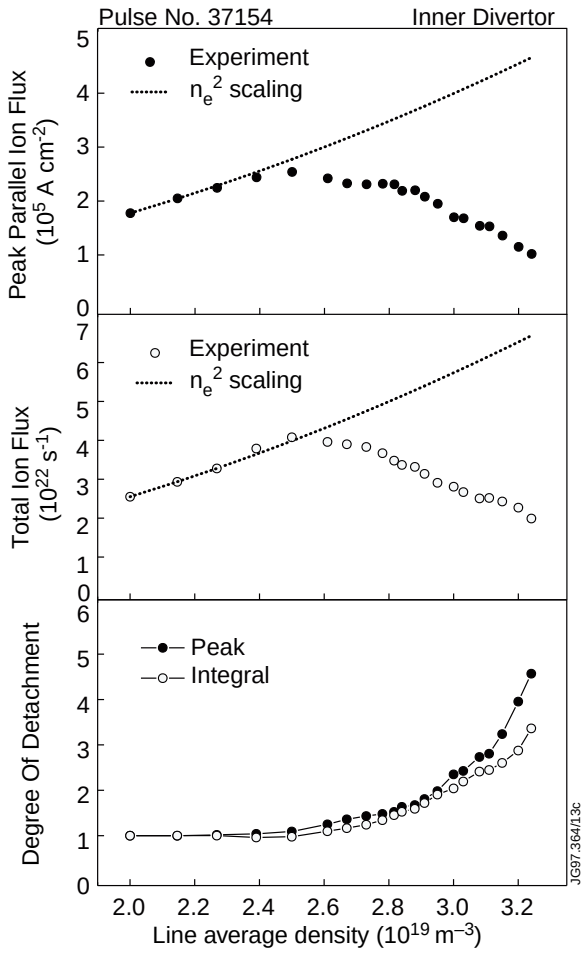

Figure 2.2: Evolution of a discharge on JET. The upstream density was continually ramped throughout the discharge, producing a 'rollover' in the ion flux measured at the inner divertor target, courtesy of the JET image database [51]. The degree of detachment is defined as the ratio of the extrapolated ion flux to the measured ion flux.

tures may be measured in the near SOL. Collisions at the edge plasma may knock ions off of closed field lines onto the open field lines of the SOL causing an additional source of ions. These ions are likely to be hotter than those in the SOL since they are not on field lines connected to the target sinks. This process is more likely to occur to confined ions than confined electrons due to the larger ion Larmor radius, see equation 2.4.

$$\begin{aligned} \rho_e &= \frac{v_{\perp e}}{\omega_{ce}} = \frac{(2m_e T_e)^{1/2}}{eB} \\ \rho_i &= \frac{v_{\perp i}}{\omega_{ci}} = \frac{(2m_i T_i)^{1/2}}{eB} \end{aligned} \tag{2.4}$$

Therefore measurements of the ion temperature would measure these ions of higher temperature in the SOL region and therefore $T_i > T_e$. Also very close to the LCFS in the SOL it can appear that $T_i > T_e$ due to ions gyrating around the LCFS. Since the ion Larmor radius is larger than the electron Larmor radius, ions on the LCFS will spend a portion of their orbit within the SOL close to the LCFS. This will have an effect on ion temperature measurements in the SOL although only in the near SOL since typically on MAST $\rho_i \sim 5$ mm, whereas the width of the SOL, λ_{SOL} (given by equation 1.5 in chapter 1), is of the order of a few cm.

2.4 Edge physics modelling

2.4.1 The two point model

The two point model is a simplified model of the scrape-off layer which relates upstream plasma parameters at the midpoint between two targets, T_u and n_u, to those at the divertor target, T_t and n_t, without a concern for the plasma behaviour parallel to the SOL [24]. This model is directly applicable to measurements made by the midplane and divertor RFEAs since they measure $T_{i,u}$ and $T_{i,t}$. As with most models for the scrape off layer the SOL is straightened out, as shown in figure 2.3. There is no attempt to model the temperature as a function of distance along the SOL as with other 1D models of the SOL, i.e $T_e(s_\parallel)$, but rather to simply relate the plasma conditions at the target to the plasma conditions upstream, hence this simple model is sometimes referred to as a 0D model of the SOL.

Assumptions

1. *Particle balance* It is assumed that particle balance is confined to individual flux tubes on the basis that any neutral resulting from ion impact on the target will re-ionise along the same magnetic field line on which it was originally travelling, with no cross-field particle flow. It is assumed that there is a thin ionisation layer in front of the target and that all recycling neutrals are ionised in this region. This results in effectively no parallel flow throughout the length

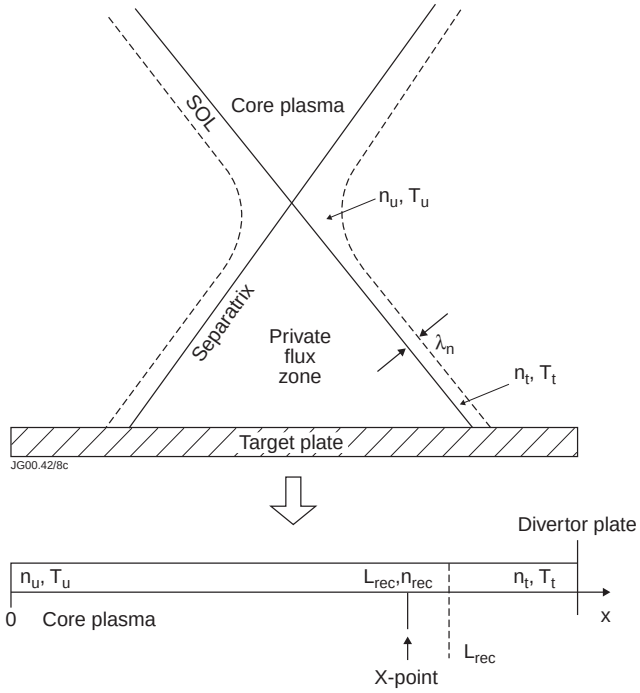

Figure 2.3: Schematic of the straightened out SOL, courtesy of the JET image database.

of the SOL, with the only parallel plasma flow in the thin ionisation region where ions have zero velocity at the start of this region, increasing up to the sound speed at the sheath entrance.

2. *Pressure balance* It is assumed that there is no friction between plasma flows in the ionisation region and no viscous effects. Therefore in the length of the SOL the total pressure is constant.

$$p + nmv^2 = constant \tag{2.5}$$

The static pressure, p is:

$$p = nkT_e + nkT_i = nk(T_e + T_i) \tag{2.6}$$

The dynamic pressure is $p_{dyn} \equiv nmv^2$, however throughout the SOL, except in the ionisation region in front of the target, it is assumed that $v = 0$. Therefore $v_u = 0$ and $v_t = c_{st} = (2k(T_e + T_i)_t/m_i)^{1/2}$. This gives a relation between the pressure upstream and at the target:

$$n_t(k(T_e + T_i)_t + mv_t^2) = n_u k(T_e + T_i)_u \tag{2.7}$$

Therefore:

$$2n_t(T_e + T_i)_t = n_u(T_e + T_i)_u \tag{2.8}$$

3. *Power balance* Since over almost the entire length of the SOL there is no par-

allel flow, there will only be parallel heat conduction and no heat convection. If it is assumed all the heat enters at the upstream and is removed at the target after distance L, then from classical parallel heat conduction [24]:

$$T_u^{7/2} = T_t^{7/2} + \frac{7}{2} q_{\parallel} \frac{L}{\kappa_{0e}} \tag{2.9}$$

where κ_{0e} is the electron parallel conductivity coefficient, and it is assumed ions and electrons are thermally coupled. Using T_t as the temperature at the sheath edge, we also have that:

$$q_{\parallel} = q_t = \gamma n_t k T_t c_{st} \tag{2.10}$$

where q_t is the heat flux density entering the sheath and γ is the sheath heat transmission coefficient:

$$\gamma = 5 + 2T_i/T_e \tag{2.11}$$

which is generally taken to be $\gamma \approx 7$ since $\mathrm{T}_i = \mathrm{T}_e$ is assumed [24, 53].

In the two point model there are three unknowns, T_t, T_u and n_t which can be solved by the following summary of equations:

$$\begin{aligned} 2n_t(T_e + T_i)_t &= n_u(T_e + T_i)_u \\ T_u^{7/2} &= T_t^{7/2} + \frac{7}{2}\frac{q_{\parallel} L}{\kappa_{0e}} \\ q_{\parallel} &= \gamma n_t k T_t c_{st} \end{aligned} \tag{2.12}$$

L, $\gamma \approx 7$ and κ_{0e} given by equation 2.13 are specified constants and n_u (m^{-3}) and $\mathrm{q}_{\parallel}$ (WM^{-3}) are considered control parameters.

$$\kappa_{0e} = \frac{30692}{Z_i \ln \Lambda} \approx 2000 \tag{2.13}$$

where Z_i is the ion species charge and $\ln\Lambda$ is the Coulomb logarithm, which can be taken as approximately 15-17 [24].

2.4.2 Edge modelling codes

More sophisticated modelling of the SOL can be performed in 1D along the field lines of the SOL using a fluid treatment. Such models of the SOL ignore toroidal magnetic curvature so that in effect the SOL is straightened out as with the two point model, see figure 2.3, and then analysed one dimensionally, or two dimensionally by including cross-field transport coefficients. An example of a 2D fluid edge model is SOLPS, which is the fluid code B2 coupled to a Monte-Carlo neutrals code Eirene [54, 55], however this is beyond the scope of this thesis. Neo-classical effects are ignored since they arise from 'toroidicity'. This can be justified by the high level of

collisionality in the SOL which characterises cold plasmas. The self-collisional mean free paths are:

$$\lambda_{ee} \approx \lambda_{ii} \approx \frac{10^{16} T^2}{n_e} \tag{2.14}$$

and the collisionality is given by:

$$\nu^*_{SOL} = \frac{L}{\lambda_{eeii}} \tag{2.15}$$

and L is the connection length. High collisionality in the SOL means that the fluid approximation, as opposed to a full kinetic model of the SOL, is adequate [24].

Onion skin modelling

The Onion Skin Model (OSM) is based on the onion skin method by Stangeby [24]. This method treats the transport along the SOL as nested flux tubes, reducing distributions of plasma fluid properties to 2D. The parallel and cross-field transport can be essentially decoupled allowing a simpler 1D treatment where the 2D element is determined by boundary conditions. This method will not be used in modelling of the experiments carried out in this thesis, however a similar 1D modelling method, SOLF1D [56], which models individual flux tubes, will be used.

SOLF1D model

SOLF1D is a 1D fluid code solving plasma transport equations along the SOL parallel to field lines between two targets [56]. The equations used are generalised Braginskii-like equations [57], generalised to account for gradients of the magnetic field parallel to the field lines in the SOL. The equations solved by the code are the continuity and momentum equations for plasma density and parallel ion velocity and the energy equations for electron and ion temperatures. This code will be used by defining the particle source upstream, based on experimental measurements, and then using SOLF1D to solve the plasma parameters along the parallel SOL distance between two targets for several flux tubes. Each flux tube solved will be equivalent to the measurements made at a radial location through the SOL so that these measurements can be compared to target measurements made by the RFEA in chapter 6. A comparison between SOLF1D and the two point model will be discussed in chapter 6 also.

2.5 Sheath physics

The transport of ions to surfaces in contact with the plasma is dominated by the presence of an electrostatic sheath which affects the transfer of particles, energy and momentum from the plasma to the surface. The sheath originates from the higher

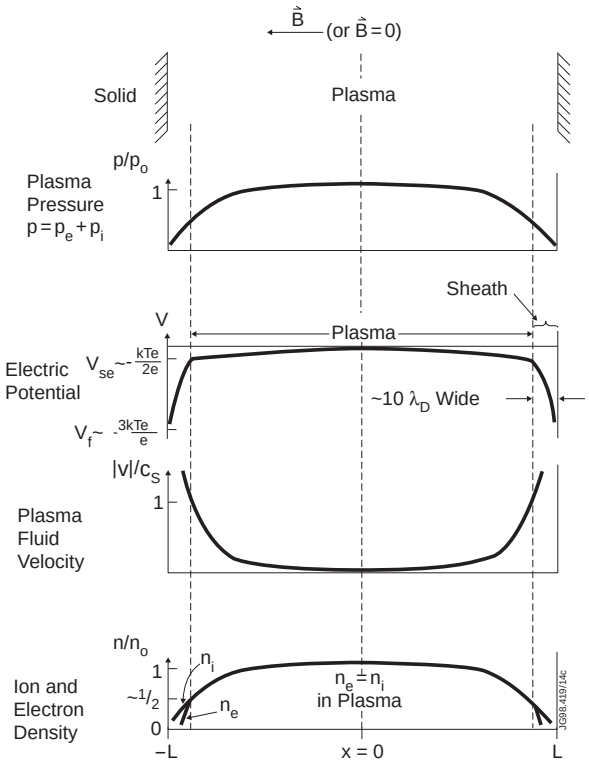

Figure 2.4: System description in a simplified derivation of the Bohm criterion, courtesy of the JET image database.

mobility of electrons compared to ions, a factor of $\sqrt{\frac{m_i}{m_e}}$. The increased number of electrons, compared to ions, at the surface in contact with the plasma produces a negative charge on the surface. This build up of negative charge causes an electric field which acts to equalise the fluxes of ions and electrons to the surface. This field is known as the *ambipolar electric field* which accelerates ions towards the surface but retards electrons in an attempt to maintain quasi-neutrality. The Bohm criterion says that ions must reach a velocity of $v \geq c_s$, the plasma sound speed, at the edge of the sheath [24]. This result can be obtained by taking a plasma in 1D along the SOL with cold ions. Within the sheath, which forms near the target, we have a net negative charge due to the higher mobility electrons, see figure 2.4. The electrons can be considered Maxwellian and therefore the density can be defined by the Boltzmann relation:

$$n_e = n_{se} e^{\frac{e(V-V_{se})}{kT_e}} \tag{2.16}$$

where V_{se} and n_{se} are the potential and density at the sheath edge. Using conservation of energy it follows:

$$\frac{1}{2} m_i v_{se}^2 = -e\Delta V_{pre-sheath} = -eV_{se} \tag{2.17}$$

From particle conservation one obtains $n_i v_i$ = *constant*. Combining this with Poisson's equation gives:

$$\nabla^2 V = -\frac{e}{\epsilon_0}(n_i - n_e) \tag{2.18}$$

This gives in 1D along the SOL:

$$\frac{d^2V}{dx^2} = -\frac{e}{\epsilon_0} n_{se} \left(\sqrt{\frac{V_{se}}{V}} - e^{\frac{e(V-V_{se})}{kT_e}} \right) \tag{2.19}$$

Looking just inside the sheath the following parameter can be defined:

$$\boldsymbol{\Delta} = V_{se} - V \tag{2.20}$$

Where $\boldsymbol{\Delta}$ is taken to be positive the following expansions can be used:

$$\left(\frac{V_{se}}{V}\right)^{1/2} \approx 1 + \frac{1}{2}\frac{\boldsymbol{\Delta}}{V_{se}} = 1 - \frac{1}{2}\frac{\boldsymbol{\Delta}}{|V_{se}|} \tag{2.21}$$

$$\exp[e(V - V_{se})/kT_e] \approx 1 - \frac{e\boldsymbol{\Delta}}{kT_e} \tag{2.22}$$

Giving the equation:

$$\nabla^2 \boldsymbol{\Delta} \approx \frac{e n_{se} \boldsymbol{\Delta}}{\epsilon_0} \left(\frac{e}{kT_e} - \frac{1}{2\,|V_{se}|} \right) \tag{2.23}$$

Since an oscillatory solution to equation 2.23 is unphysical we can therefore assume:

$$\begin{aligned} \frac{e}{kT_e} &\geq \frac{1}{2\,|V_{se}|} \\ m_i v_{se}^2 &\geq kT_e \\ v_{se} &\geq \sqrt{\frac{kT_e}{m_i}} = c_s \end{aligned} \tag{2.24}$$

Therefore it follows that ions exiting the sheath must do so with a speed greater than the ion sound speed, c_s. A further deduction can be made from equation 2.23 about the size of the sheath [24]:

$$\begin{aligned} \frac{\boldsymbol{\Delta}}{L_{sheath}^2} &\approx \frac{en\boldsymbol{\Delta}}{\epsilon_0}\frac{e}{kT_e} \\ L_{sheath} &\approx \left(\frac{\epsilon_0 kT_e}{e^2 n}\right)^{1/2} \approx \lambda_D \end{aligned} \tag{2.25}$$

which is know as the debye length, the length over which electrostatic potentials are screened out by a process called Debye screening [24]. Taking target conditions in MAST of $T_e = 20$ eV and $n_e = 1 \times 10^{18}$ m^{-3}, we find $\lambda_D \approx 40$ μm. Therefore the sheath is very thin compared to the parallel length of the SOL which in MAST is of the order of ~ 20 m.

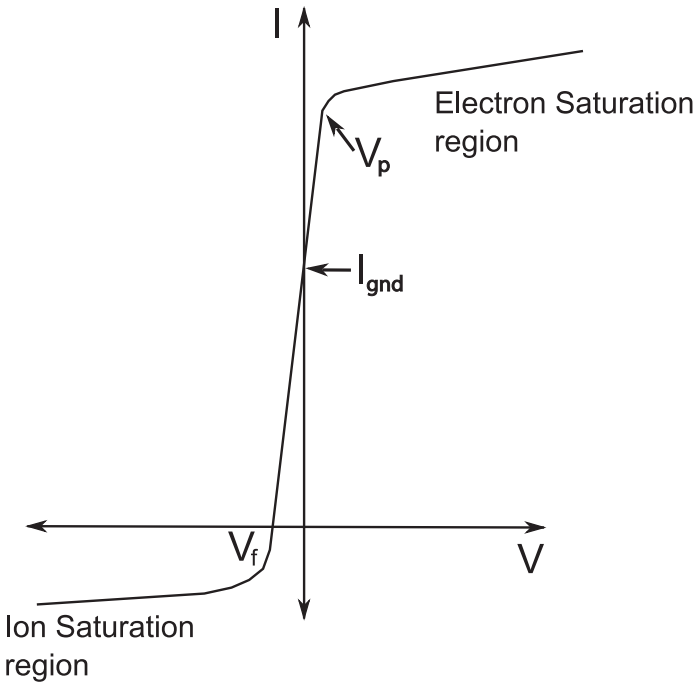

Figure 2.5: Typical I-V characteristic for a Langmuir probe.

2.6 Diagnostic theory

2.6.1 Langmuir probes

Modelling requires values of T_e and n_e to describe the scrape-off layer. A useful diagnostic which can determine these parameters is the Langmuir probe (LP) which is used in tokamak SOLs either at the divertor targets or on reciprocating probes to measure the upstream SOL parameters. Langmuir probes measure the electron temperature (T_e) and ion saturation current density (j_{sat}), which can be used to determine n_e, at the edge plasma. The Langmuir probe acts as a material sink for the SOL plasma and therefore due to the higher thermal velocity of electrons compared to ions a sheath is set up at the probe surface. When the probe is held at zero bias with respect to the divertor a non-zero current flows to the Langmuir probe, I_{gnd} [58]. When the Langmuir probe is left floating with no external bias, the voltage reached by the probe is the floating potential, V_f, and the electrostatic sheath acts to equalise the particle fluxes to the LP so that no net current is drawn at this point [25]. The random Maxwellian flux to a probe is given by:

$$\Gamma = \frac{1}{4} n \overline{v} = \frac{1}{4} n \sqrt{\frac{8kT_e}{\pi m_e}} \tag{2.26}$$

Where $\overline{v}$ is the mean particle velocity and n is the particle density. Using the Boltzmann relation for electrons, the electron flux is given by:

$$\Gamma_e = \frac{1}{4} n_{se} c_s e^{\frac{eV_f}{kT_e}} \tag{2.27}$$

Where n_{se} is the density at the sheath edge $\approx \frac{1}{2}n_e$, roughly half the bulk electron density. The ion flux is approximated by equation 2.26. Therefore for a floating probe where $\Gamma_e = \Gamma_i$, and without secondary electron emission:

$$\frac{eV_f}{kT_e} = \frac{1}{2}\ln\left[\left(\frac{2\pi m_e}{m_i}\right)\left(\frac{T_i}{T_e}+1\right)\right] \tag{2.28}$$

Measurements by Langmuir probes of T_e and j_{sat} are made by the interpretation of current-voltage (I-V) characteristics, see figure 2.5. The measurement is made by biasing the probe to voltages less than the plasma potential and then sweeping the voltage to positive values whilst recording the current arriving at the probe. When a sufficiently negative bias is applied all electrons are repelled and the current measured at the probe is purely an ion current, known as the ion saturation current $I_{i,sat}$. When a sufficiently positive bias is applied, all ions will be repelled giving a purely electron current, called the electron saturation current $I_{e,sat}$. Generally it is the region between the ion saturation current and the plasma potential of the I-V characteristic which is of interest. There are many effects which can prevent the probe reaching a clear electron saturation current, making it difficult to analyse. Also drawing a large electron current from the plasma can be perturbing to the plasma and can cause excessive heating and therefore damage to the probe surface.

In the region between the floating potential, V_f, and the plasma potential, V_p, the current arriving at the probe consists of electrons and ions, and it is here that the electron energies are sampled. In the region closest to ion saturation only electrons of the highest energies will arrive at the probe surface, but as the bias increases positively so does the number of electrons collected.

The total current to the LP is approximated by [59]:

$$I_p = I_{i,sat}\left[\exp\left(\frac{e(V_{bias}-V_f)}{T_e}\right)-1\right] \tag{2.29}$$

Where V_{bias} is the external bias applied to the LP. The values of V_f and $I_{i,sat}$ can be determined from the I-V characteristic in figure 2.5, allowing T_e to be determined from fitting. The electron density, n_e, can be determined using the relation:

$$j_{sat} = en_e c_s \tag{2.30}$$

where $j_{sat} = \frac{I_{i,sat}}{A_{coll}}$ and A_{coll} is the area of the collecting surface of the LP. Generally $T_i = T_e$ is assumed to calculate n_e however if $T_i > T_e$ then this will give incorrect values of n_e since:

$$n_e = \frac{e}{j_{sat}}\sqrt{\frac{k(T_i+T_e)}{m_i}} \tag{2.31}$$

Therefore, it is important to determine the correct value of T_i in order to give accurate measurements of n_e from Langmuir probes. The plasma potential, V_p, can be approximated by [60]:

$$V_p \simeq V_f + 2.5\frac{T_e}{e} \tag{2.32}$$

where V_f is the floating potential and T_e is the electron temperature, see figure 2.5.

2.6.2 Infra-red (IR) thermography

Infra-red (IR) thermography can be used to measure the heat flux to plasma facing components and the power to the divertor. The infra-red camera measures the intensity of light emitted from the divertor targets as a photon flux. The flux of photons from a black body in a given wavelength range can be found by dividing Planck's Law [61], for the power emitted from a black body, by the energy of a photon and integrating over the wavelength range of the camera. This gives the black body temperature of the divertor tiles. The degree to which an object can be considered a black body is expressed as its emissivity. Since the MAST divertor titles are graphite an emissivity of $\epsilon = 0.7$ is used because it is a grey body [62].

The change in measured surface temperature can be used to give the heat flux at the divertor target by Fourier's Law:

$$\mathbf{q} = -k\nabla T \tag{2.33}$$

Where $\mathbf{q}$ is the heat flux, k is the thermal conductivity and T is the surface temperature. The heat transfer equation relates the heat flux to the temporal evolution of the surface temperature. The IR camera measures the left hand side of equation 2.34.

$$\rho C_p \frac{\partial T}{\partial t} = -\nabla \cdot \mathbf{q} \tag{2.34}$$

Where ρ is the density of the material, C_p is the heat capacity of the material and $\mathbf{q}$ is a function of depth into the material. Substituting in equation 2.33 the equation becomes:

$$\rho C_p \frac{\partial T}{\partial t} = -k\frac{d^2T}{dx^2} \tag{2.35}$$

Where x is the depth into the divertor tiles. The heat transfer code THEODOR [63] is used to solve these equations since k and C_p are also functions of temperature.

The power to the divertor targets can be calculated as the heat flux integrated over the surface area of the target. Therefore the power to the divertor can be found as a function of time through a MAST discharge. One problem with these measurements is that in a tokamak, surface layers form on divertor targets and can give false readings of $\mathbf{q}$ so this must be accounted for during analysis [26].

2.7 Summary

The scrape-off layer and divertor operating regimes have been discussed since these are important for determining which processes are dominant in the SOL, particularly

when comparing to models of the SOL. Reasons for $T_i > T_e$ in the SOL have been considered because these will be investigated using the measurements made by RFEA. SOL modelling of varying complexity has been discussed, however only the two point model and the 1D fluid model, SOLF1D, will be further explored in chapter 6. Finally the theory of diagnostics that will be used for analysis have been detailed, excluding RFEA theory which will be discussed in detail in chapter 3.

Chapter 3

Retarding field energy analysers

3.1 RFEA principle

Retarding Field Energy Analysers (RFEA) are considered to be the most reliable and least perturbing method of measuring ion temperatures in the scrape-off layer of tokamaks [39, 41, 64]. An RFEA probe can access the SOL plasma ion velocity distribution directly and is designed to measure the component of the velocity parallel to the magnetic field. Charged particles, in this case ions, are transmitted through an aperture in the RFEA and are analysed by retardation in the electric field established in the analyser through potentials applied to a number of grids, see figure 3.1. The entrance slit to the RFEA probe is aligned along the magnetic field so that the parallel component of the ion velocity distribution can be sampled. The entrance must be sufficiently wide to allow adequate flux transmission but small enough to ensure the aperture is shielded from the plasma. The front slit plate is negatively biased to repel most of the thermal electrons in the plasma. The ions transmitted through the slit plate encounter the first grid and are retarded by the swept positive voltage, V_{grid1}, applied to it. Grid 2, the suppressor grid, is held at a constant negative potential to suppress secondary electrons either emitted from the collector, or from the rear of the slit plate due to ion impact. The collector plate at the back of the analyser measures the ion current, I_{col}, which can be found as a function of V_{grid1}. A schematic of the RFEA, the biasing scheme and typical voltages used in steady state measurements are shown in figure 3.1.

For grid 1 voltages in the range $V_{grid1} = 0 \rightarrow |V_s|$, where V_s is the sheath voltage, the collector current will stay at the maximum current measured at the collector, I_0, since all ions gain a parallel energy of $eZ_i |V_s|$ (where eZ_i is the ion charge) in the collisionless Debye sheath. For $V_{grid1} > |V_s|$ the ion current measured at the collector will decrease. Assuming the ion flux is dominated by deuterium plasma ions with charge eZ_i, the ion collector current can be expressed as:

$$I_{col} = AeZ_i \int_u^\infty v_{||} f(v_{||}) \xi(v_{||}) \mathrm{d}v_{||} \tag{3.1}$$

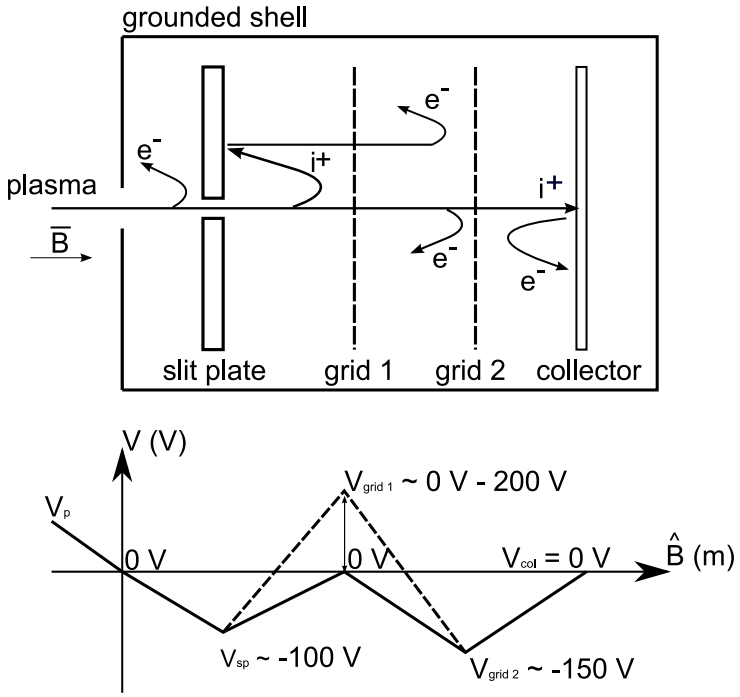

Figure 3.1: Schematic of an RFEA module showing the function of the slit plate, grids and collector plate. The biasing scheme is shown with typical voltages for steady state operation. All voltages are with reference to the plasma potential.

where A is the effective area of the slit plate, eZ_i is the ion charge, $\xi(v_{||})$ is the total transmission factor including the transmission of the slit and grids, $u = \sqrt{2eZ_iV_{grid1}/m_i}$ (m_i is ion mass) and $f(v_{||})$ is the parallel ion velocity distribution. Assuming that $f(v_{||})$ is Maxwellian, T_i can be obtained for $V_{grid1} \geq V_s$ by a fit to the exponential decaying part of the collector current as a function of the discriminating voltage;

$$I_{col} = I_0 \exp\left[-\frac{Z_i}{T_i}(V_{grid1} - |V_s|)\right] \tag{3.2}$$

where T_i (in eV) is the effective ion temperature of the distribution and I_0 is the maximum current on the collector. Since the plasma is deuterium we take $Z_i = 1$ for our measurements. An example I-V characteristic obtained for the divertor RFEA in MAST can be seen in figure 3.2 where the transition between the constant current at $V_{grid1} < |V_s|$ and the exponential decay occurring at $V_{grid1} > |V_s|$ can be seen.

As shown by Valsaque et al [65], the effective ion temperature measured on each side of a double sided RFEA probe, where two modules (see figure 3.1) are arranged back to back (bidirectional), are different, therefore it matters whether the measurements is facing the flow direction, the upstream temperature (T_i^u), or the direction facing away from the plasma flow, the downstream temperature (T_i^d). The Maxwellian distribution is distorted in the pre-sheath plasma on both sides so that $T_i^{*u} > T_i^{*d}$. Assuming a collisionless pre-sheath, an accurate estimation of T_i

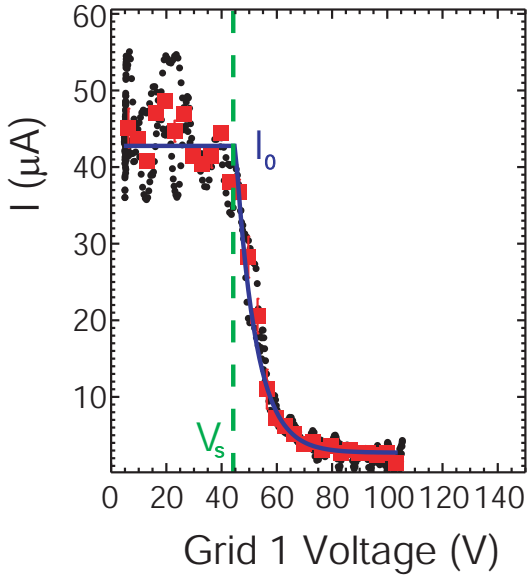

Figure 3.2: Example I-V characteristic showing V_s and I_0.

is given by $(T_i^{*u} + T_i^{*d})/2$ for bidirectional RFEA probes [41, 65, 66]. Since the target RFEA is unidirectional, measurements will be affected by flows close to the target. Valsaque's analysis [65] can be used to estimate the necessary correction factor for target T_i measurements. This effect will be studied in chapter 6 along with estimates from modelling of the flow at the entrance to the target RFEA. A correction of between 0.65 and 0.7 has been found necessary for measurements by the target RFEA.

3.2 RFEAs in MAST

On MAST two RFEA probes are used; one at the outer midplane and one in the outer divertor target. Figure 3.3 shows the location of both RFEA probes as well as the line of sight of the Thomson scattering system in a poloidal cross-section.

3.2.1 RFEA modules

The assembly of a slit plate, discriminating and suppressor grids, and the collector plate is termed a 'module'. For bidirectional RFEA probes, two modules are used and arranged back to back; for uni-directional probes one module is used facing the plasma flow direction. The MAST RFEA design is based on the RFEA built and operated at Tore Supra, CEA in Cadarache, France and tested on MAST [41, 42]. A schematic of a module can be seen in figure 3.4.

Slit plate

The slit plate is made of nickel, with a thickness of 150 μm on the midplane RFEA and 200 μm on the divertor RFEA. Slit plates were made using a photoelectro

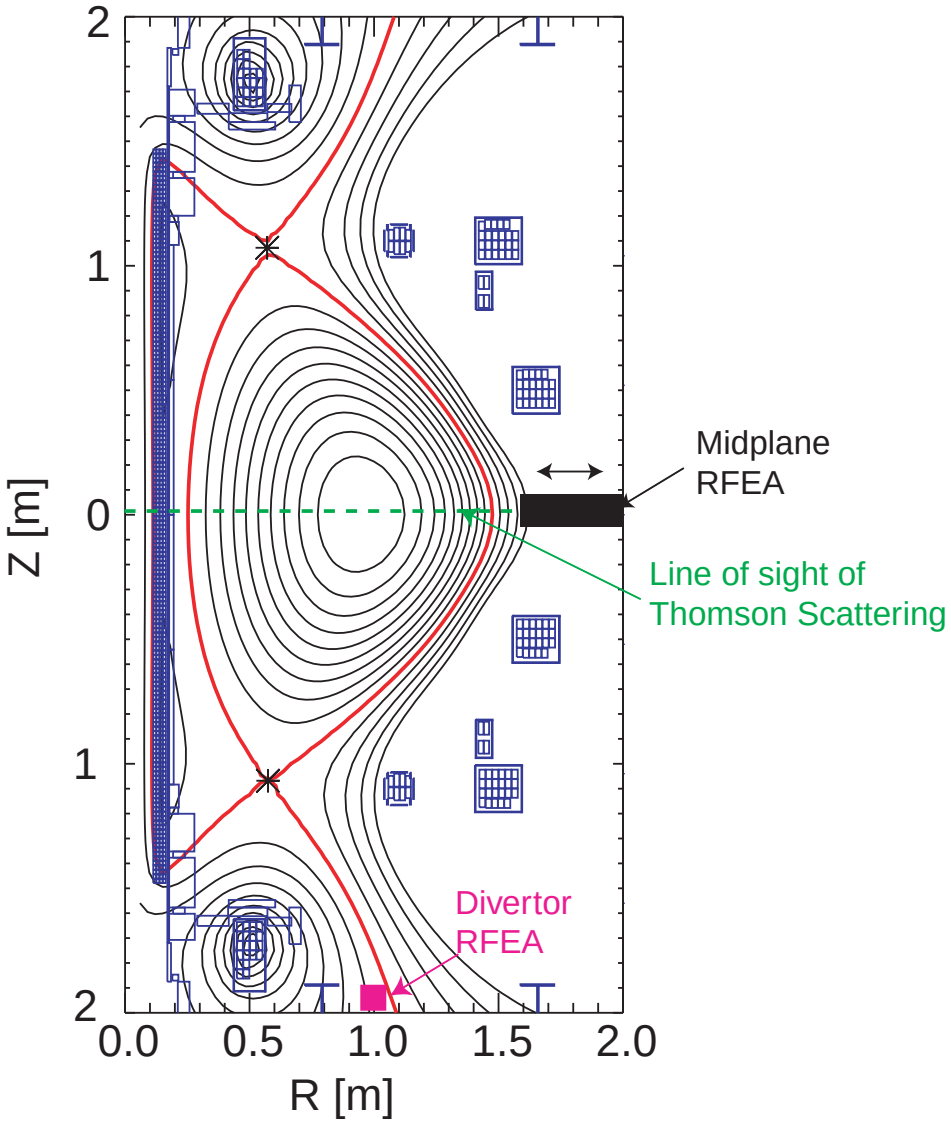

Figure 3.3: Cross-section of MAST showing the location of both the midplane and divertor RFEA and the line of sight of the Thomson scattering in a double null plasma equilibrium.

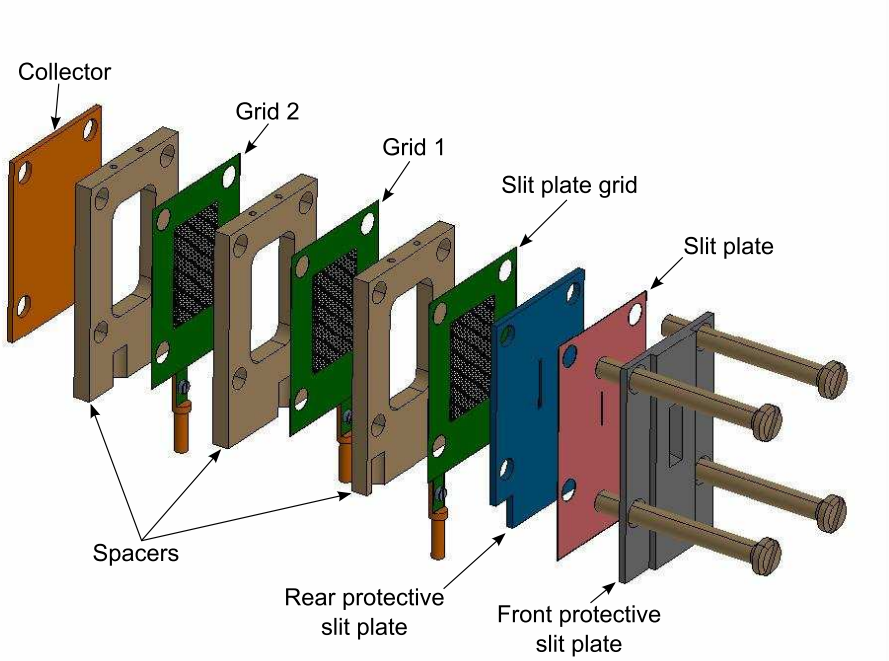

Figure 3.4: Exploded image of an RFEA module showing three grids, slit plate with front and rear protective plates, collector plate and boron nitride insulating spacers.

forming process. They are held between two protective plates both made from stainless steel. Each protective plate has a slit with dimensions 1 × 7 mm allowing access of the ions to the slit plate. The slit plate has a rectangular slit with a length of 5 mm and a width of 20 μm which must be of the order of the debye length, $\sim \lambda_D$, to ensure continuity of the sheath potential surface across the slit [39, 52]. The debye length can be calculated for both the divertor and the midplane using equation 3.3.

$$\lambda_D = \sqrt{\frac{\epsilon_0 k_B T_e}{n_e e^2}} \simeq 7.43 \times 10^6 \sqrt{\frac{T_e[eV]}{n_e[m^{-3}]}} \tag{3.3}$$

where the Debye length is in mm. $\lambda_{Dmidplane}$ is calculated for T_e = 50 eV and n_e = 10^{19} m^{-3} which gives $\lambda_{Dmidplane} \approx 16$ μm. For the divertor, where $T_e \sim 10$ eV and $n_e = 10^{18}$ m^{-3}, $\lambda_{Dtarget} \approx 24$ μm. The slit width used (20 μm) is of the order of both these estimated debye lengths.

Grids and collector plate

Nickel foils of thickness 50 μm are used for the grids, see figure 3.5. Grid wires with width, Δ = 50 μm are separated by D = 0.4 mm. The grids, like the slit plates, were made using a photoelectro forming process. The grid transmission is calculated by $\zeta_{opt} = (D - \Delta)^2/D^2 = 0.77$ [52]. The area of the grid is 15 × 10 mm, meaning that the length of the grid area exceeds the 5 mm long slit plate aperture by 5 mm on each end of the aperture. This distance is larger than the ion Larmor

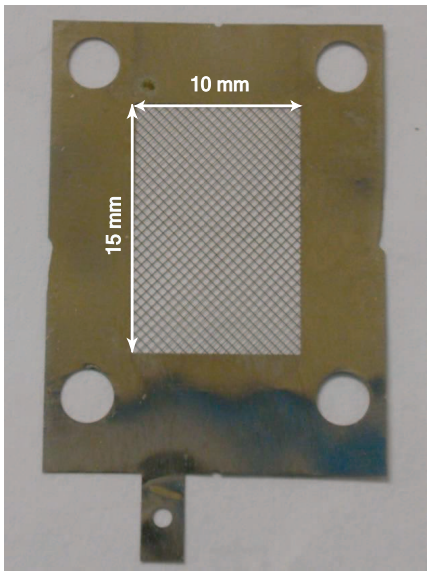

Figure 3.5: A grid used in the midplane RFEA. The area of the grid (10 × 15 mm) and the diagonal wires creating the grids can be seen.

radius in the MAST SOL which is in the range r_L = 1-4 mm. Therefore the grid transmission factor is not affected by the collection of ions outside the grid area. The grid wires are diagonal to the orientation of the slit to ensure that no single grid wire will entirely block the particle trajectories into the analyser. In addition to grids 1 and 2, there is a further grid attached to the rear of the slit plate (see figure 3.4) designed to ensure the electric field between the slit and grid 1 is as planar as possible [67]. The collector at the rear of the RFEA module is copper to give good electrical conductivity.

The grids and collectors are separated by 2.5 mm thick boron nitride spacers. The stack of grids and plates is held together in a structure made from Polyether ether ketone (PEEK) which is designed to fit the spatial constraints and structural requirements of the individual probe heads. The attenuation by the slit in the slit plate can be determined by equation 3.4 where I_0 is the maximum current at the collector [52].

$$\xi_r^{exp} \cong \frac{I_0}{j_{sat} h w \xi_{opt}^3} \tag{3.4}$$

In the case of the MAST RFEAs $\zeta_r^{exp} = 0.1 - 0.3$. Combining this with the transmission through three grids each with $\zeta_{opt} = 0.77$ means an estimated 0.09 of the ions incident on the slit plate are transmitted to the collector plate.

3.2.2 Space charge limitations

Space charge is the build up of charge in the analyser head which causes a potential which can repel plasma entering the analyser. In the RFEA the voltage on grid 1, V_{grid1}, is assumed to be the highest voltage in the system and therefore grid 1

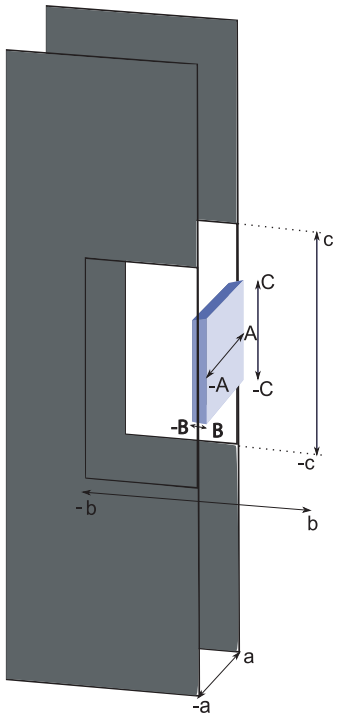

Figure 3.6: Diagram of volume in RFEA analyser used to calculate space charge with definitions for A,B,C,a,b and c. The grey plates represent the grid plates with the clear section the grided area. The pale blue box represents the volume of the incoming ion beam

reflects transmitted ions with energies less than $Z_i eV_{grid1}$. If the highest voltage in the system is not defined by V_{grid1}, but instead by the vacuum potential plus the positive space charge potential in the analyser, then measurements obtained from the RFEA I-V characteristics are affected. The space charge potential and the limiting current in the analyser can be calculated from Nachtrieb's space charge formula (equation 3.5) [52, 68].

$$\frac{V_{sc}(x,0,0)}{\rho/\epsilon_0} = \sum_{l,m,n}^{\infty} \frac{8cosk_l x}{k_l^2 + k_m^2 + k_n^2} \frac{(-1)^2}{k_l a} \frac{sink_m B}{k_m b} \frac{sink_n C}{k_n c} \tag{3.5}$$

where $k_l = (l + \frac{1}{2})\pi/a$ and $k_m = (m + \frac{1}{2})\pi/b$ and $k_n = (n + \frac{1}{2})\pi/c$ and $\rho \cong I^*/(v_T 4BC)$. I^* is the current between grid 0 (at the back of the slit plate) and grid 1. See figure 3.6 for definitions of parameters A,B,C,a,b and c in the RFEA analyser.

Equation 3.5 can be expressed as

$$V_{sc}(x,0,0) = \frac{I_0}{\sqrt{T_i}} KS \tag{3.6}$$

where I_0 is the collector current for $V_{grid1} \leq |V_s|$, $K = \left(4\xi_{opt}^2 \epsilon_0 BC\sqrt{e/m_i}\right)^{-1}$ and S is the summation term in equation 3.5.

The space charge limited current, I_{max}, can be found for the case:

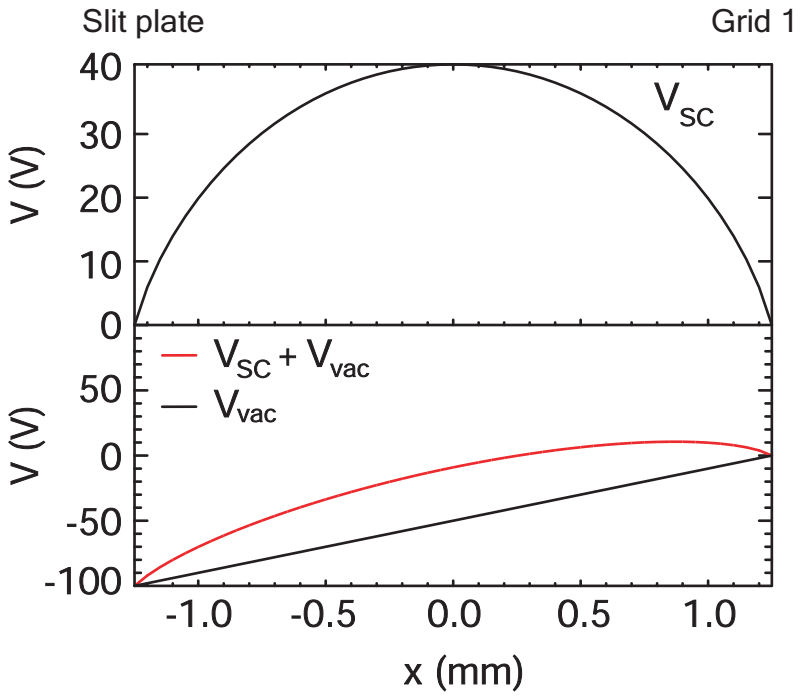

Figure 3.7: Profile of positive space charge potential between the back of the slit plate (grid 0) and grid 1 for 1D along x, the direction parallel to B. Also shown is the maximum vacuum potential compared to the result of the vacuum and space charge potential between the slit plate and grid 1. The space charge potential is calculated for $I_0/\sqrt{T_i} \cong 3 \times 10^{-5}$ [AeV$^{-1/2}$], with $V_{SP} + V_s$=-100 V, $V_{grid1} = 0$ V, a = 1.25 mm, b = 7.5 mm, c = 5 mm, A = 1.25 mm, B = 2.5 mm and C = 10μm using equation 3.5.

$$\frac{eV_{sc}(0,0,0)}{T_i} = \frac{e}{T_i}\frac{a^2}{2\epsilon_0}\frac{I_{max}}{4BC}\sqrt{\frac{m_i}{T_i}}F(a,b,c,A,B,C) \approx 1 \tag{3.7}$$

where F(a,b,c,A,B,C) is the sum term in equation 3.5 multiplied by $2/a^2$.

For steady state operation of the RFEA we take the case with T_i = 10 eV. Figure 3.7 shows the space charge potential between the slit plate and grid 1 for the direction parallel to the magnetic field. The space charge has been calculated using equation 3.6 with $I_0/\sqrt{T_i} \cong 3 \times 10^{-5}$ AeV$^{-1/2}$. When there is no voltage applied to the slit plate it can be seen in figure 3.7 that the analyser would be space charge limited since $V_{sc} \sim 40$ V. The maximum current that can be accepted by the analyser in this case is I $\leq$ 22 μA which is too small for SOL measurements on MAST. Measurements by the RFEA are only analysed when there is at least -100 V applied to the slit plate since with the additional negative vacuum potential, the potential in the analyser is reduced as shown in figure 3.7. In the case with $V_{sp} \leq$ -100 V the analyser is able to accept currents of I $\sim$ 90 μA.

The maximum current which can be accepted by the analyser is proportional to the ion temperature as shown in figure 3.8. The benefit of this relation is that at higher temperatures the analyser can accept more current. For measurements during ELMs where the slit plate voltage is held lower, V_{sp} = -250 V, a higher current can be accepted into the analyser since there is both a larger negative vacuum potential

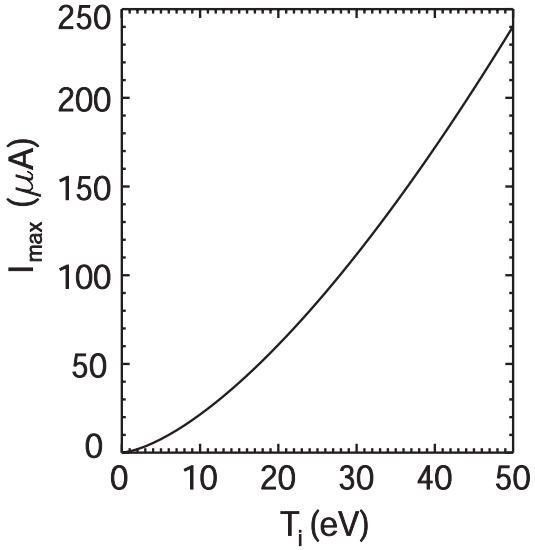

Figure 3.8: Space charge limited current, I_{max}, as a function of T_i, calculated from equation 3.7 for dimensions of the MAST RFEA module; a = 1.25 mm, b = 7.5 mm, c = 5 mm, A = 1.25 mm, B = 2.5 mm and C = 10μm.

and the ions are hotter. For the case during ELM measurements the space charge potential has been calculated with $I_0/\sqrt{T_i} \cong 2 \times 10^{-5}$ AeV$^{-1/2}$ as $V_{sc} \sim 30$ V. When this is combined with the vacuum potential in the analyser it is clear that it is not space charge limited and grid 1 is the dominate potential in the system, as shown in figure 3.9. In this case the RFEA can accept currents of ~ 190 μA which is sufficient for ELM measurements at the target.

The model used by Nachtrieb [68] for the space charge calculation can be considered a 'worse-case' scenario since it neglects radial divergence of the ion beam due to finite ion Larmor radii which would reduce the space charge. The RFEAs are space charge limited without sufficiently negative potential applied to the slit plate however the analyser can accept the currents incident on the probe provided the appropriate voltages are applied to the slit plate. All data measured by the RFEAs without sufficient slit plate voltage are disregarded and therefore all the data presented in this thesis are not affected by space charge limits.

3.2.3 Midplane system

The midplane RFEA, shown in figure 3.10, has two modules arranged back to back within the probe head allowing measurements in both flow directions of the upstream scrape off layer. There is additional shielding in the probe head over the double sided module. An electrically grounded copper cap is fixed over the double module to reduce electrical noise and a boron nitride cap is positioned either side for electrical insulation. The probe head is encased entirely in a grounded graphite shell which protects the modules and electrical components from the plasma. The slot in the graphite shell which allows the plasma access to the slit plate has an area of ~ 30 mm^2.

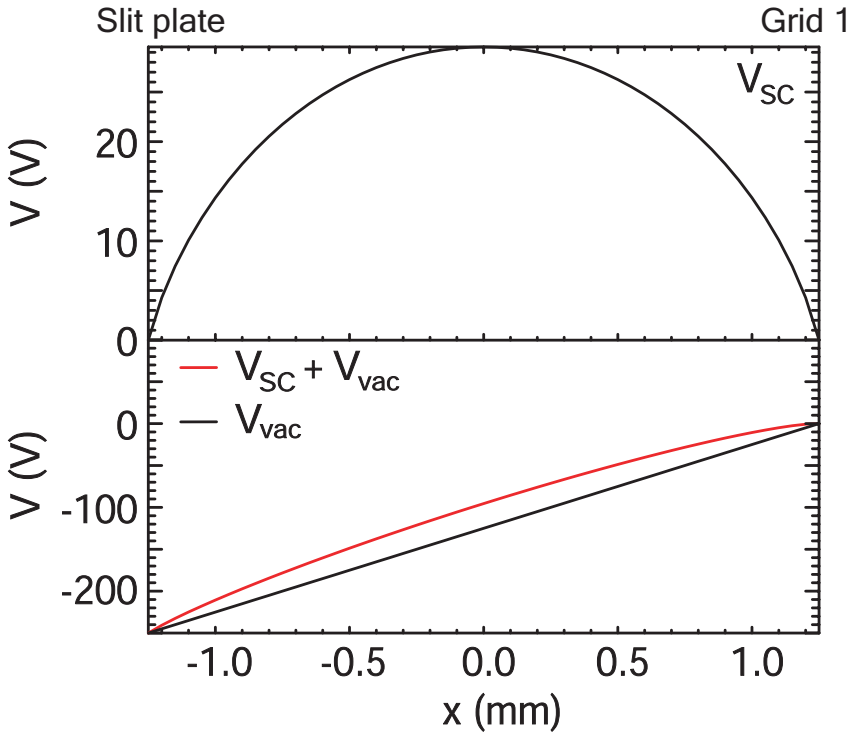

Figure 3.9: Profile of positive space charge potential between the back of the slit plate (grid 0) and grid 1 for 1D along x. Also shown is the maximum vacuum potential compared to the result of the vacuum and space charge potential between the slit plate and grid 1. The space charge potential is calculated for $I_0/\sqrt{T_i} \cong 2 \times 10^{-5}$ [AeV$^{-1/2}$], with V_{SP} + V_s=-250 V, V_{grid1} = 0 V, a = 1.25 mm, b = 7.5 mm, c = 5 mm, A = 1.25 mm, B = 2.5 mm and C = 10μm using equation 3.5. It is clear that for these measurements the analyser is not space charge limited.

Figure 3.10: Midplane RFEA probe head with the graphite shell removed to reveal the front slit plate of the double sided module.

The midplane RFEA is mounted on the reciprocating probe (RP) at the outer midplane of MAST. The upstream side (side A) of the analyser is connected to the lower-outer divertor, and the downstream side (side B) is connected to the upper-outer divertor in double-null (DN) plasmas. For lower single null (LSN) plasmas the downstream side is connected to the lower inner divertor.

One reciprocation into the plasma edge is possible in a single MAST discharge. The RP can reciprocate with a maximum speed of 0.9 m/s over a range of up to 10 cm [11]. A typical reciprocation of $\sim$ 7 cm, used in the discharges analysed here, can be seen in figure 3.11. For each discharge the start position of the reciprocating probe, the penetration depth into the plasma edge and the reciprocation start time can be varied. The RP can also be held stationary at different positions to allow ELM statistics to be collected whilst at a safe distance from high heat loads.

The alignment of the probe head with the magnetic field is achieved by rotating the outer reciprocating probe shaft. The magnetic field pitch angle in MAST can change by about $\pm$ 10°, however the plasmas in which midplane measurements have been obtained did not change more than $\sim$ 5° which is well within the necessary alignment previously determined by Kočan [41]. An appropriate angle can be chosen for each experiment session, however the probe is normally set to $\sim$ 30°; the average pitch angle at the MAST midplane.

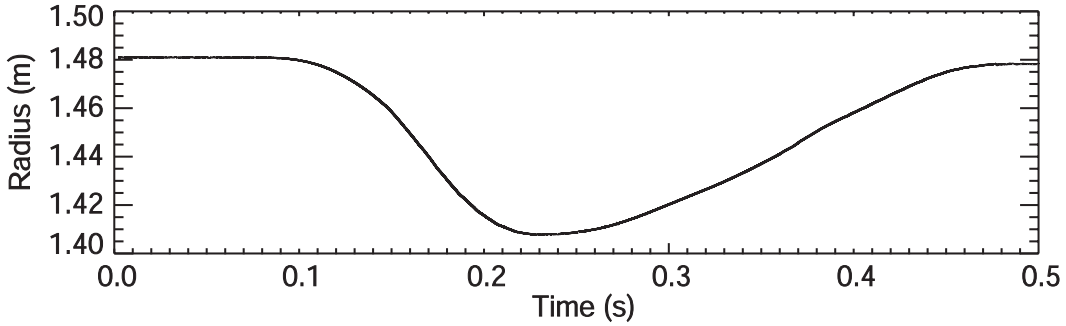

Figure 3.11: Typical reciprocating waveform for the RP RFEA during one plasma discharge. The start position, penetration depth and reciprocation start time can be chosen for each plasma discharge. Measurements are typically made up to 2 cm inside the LCFS at the midplane.

3.2.4 Target system

The divertor RFEA is installed on the Divertor Science Facility (DSF), an assembly designed to manipulate samples and various probe heads into a gap in the MAST lower outer divertor target at R= 0.985 m [12]. The module is protected by a graphite shell on the protruding part of the RFEA which is exposed to plasma, see figure 3.12. The slot in the graphite shell which allows the plasma access to the slit plate has an area of ~ 30 mm^2. The divertor RFEA has a single module facing the direction of plasma flowing towards the divertor targets. A boron nitride cap is included in the module assembly between the RFEA module top and the graphite shell to reduce the likelihood of electrical arcing between the shell and the grids. When fully inserted the DSF RFEA protrudes 25 mm above the target plate. The slit is arranged to intercept ions which would be incident on the target. The point at which the incident ions hit the collector plate is almost level with the top of the divertor target plate as shown in figure 3.13.

It is possible to alter the height of the probe so that it can be flush with the divertor tile for protection, however the probe can only take measurements when it is fully inserted. The positioning of the RFEA in the target plate can be changed from run day to run day. The slit in the front face of the RFEA is at 9° to vertical so that the RFEA module and slit entrance are aligned with the average magnetic field for MAST plasmas. This ensures the parallel velocity distribution is sampled by the RFEA. The actual value for the angle at the target can vary over discharges in the range $4 - 12$ °, however this is within the acceptable range of angles $\sim \pm 10°$ that should not affect the measurement of T_i [41].

The use of a protruding probe at the divertor, such as the target RFEA, is limited by the heat flux it can stand. The two limiting factors are the maximum load and the duration this load is incident on the probe head. The use of the divertor probe is possible on MAST because there is a low power incident on the divertor and sweeping of the outer strike point reduces the duration this peak power is incident on the probe. The front face of the RFEA probe shell is exposed to a parallel

Figure 3.12: Divertor RFEA probe head attached to the DSF bracket. The graphite head shows the single slit entrance to the probe which is aligned along the average total magnetic field at the divertor target. Only the graphite shell section of the probe head is exposed to the plasma since it is the top most section of the probe which protrudes above the divertor tiles, see figure 3.13.

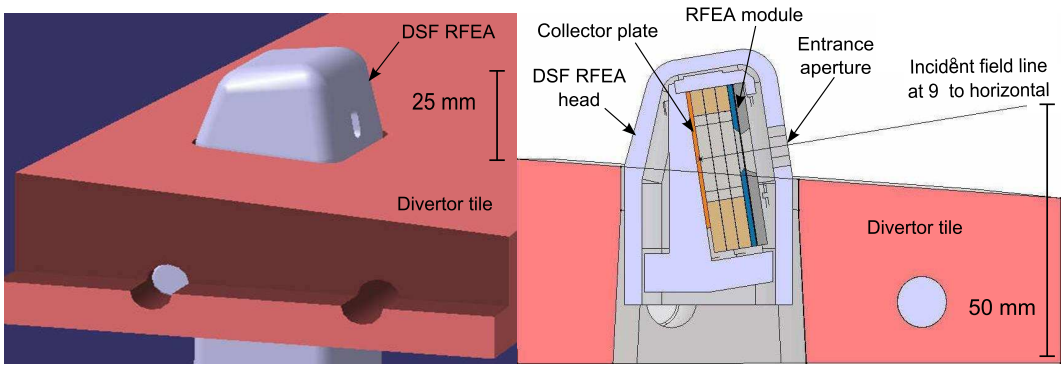

Figure 3.13: Divertor RFEA *in situ* at the divertor tile showing the maximum protrusion above the divertor tile which is required for ion temperature measurements. Also shown is a cross-section through the divertor RFEA probe head as positioned in the divertor tile. The magnetic pitch angle at the RFEA can be seen. The magnetic pitch angle line shows the point at which the field line intercepts the collector plate, $\sim$ 2 mm above the divertor tile; this is where the I_{col} is measured.

power flux density $q_{||} < 6.5$ MW/m^2 at the divertor for 400 kA discharges; based on infra-red thermography measurements of the target power fluxes, and the local field line angle at the target. The context for this low parallel power density can be understood using equation 3.10 which estimates the effective outboard midplane parallel power density from the power entering the SOL (equation 3.8 where P_{ohmic} and P_{NBI}^{abs} are the ohmic and NBI heating power respectively, P_{rad} is the power lost by radiation, and $\dot{W}$ is the change in stored energy as a function of time). The power is split, in this case, 50:50 to the upper:lower divertors and 10:90 to the inner:outer divertors. Equation 3.11 relates the parallel power density to the local field (which is dominated by the toroidal field) and can give the equation for the power flux density at the divertor, equation 3.12.

$$P_{SOL} = P_{ohmic} + P_{NBI}^{abs} - P_{rad} - \dot{W} \tag{3.8}$$

$$P_{in} = P_{SOL} \times up/downfraction \times in/outfraction \tag{3.9}$$

$$q_{||}^{omp} \approx \frac{P_{in}}{2\pi R_{omp}(B_\theta/B_\phi)_{omp}\lambda_q^{omp}} \tag{3.10}$$

$$q_{||}^{div}/q_{||}^{omp} \approx R^{omp}/R^{div} \tag{3.11}$$

$$q_{||}^{div} = \frac{P_{in}}{2\pi R_{div}(B_\theta/B_\phi)_{omp}\lambda_q^{omp}} \tag{3.12}$$

For $R_{omp} = 1.4$ m, $R_{div} = 0.985$ m, $(B_\theta/B_\phi)_{omp} \approx 0.35$ and $\lambda_q^{omp} = 8$ mm (measured at the target in a low density plasma, with $\bar{n}_e = 1.2$ x 10^{18} m^{-3}, by the infra-red camera and mapped to the midplane using Eich's formula [69]); a parallel power density at the RFEA of 6.5 MW/m^2 then corresponds with a loss power from the plasma of P_{heat} - $P_{rad}^{core} \approx 250$ kW. This is consistent with the expected ohmic heating and radiated power for 400 kA plasmas in MAST. For higher power discharges the parallel power density is higher, ~ 25 MW/m^2, since values are about $P_{in} \sim 560$ kW and $\lambda_q^{omp} = 1$ cm.

In MAST the change in solenoid flux throughout the shot causes the divertor leg to move across the divertor plates. The natural sweeping of the outer divertor leg makes it possible to get a radial profile of measurements as a function of distance from the separatrix at the target while measurements are taken at the fixed point of the DSF.

3.2.5 RFEA electronics

Power supplies have been designed and built in-house at CCFE specifically to drive the slit plates and grids of the RFEA. There are three different power supplies which drive and measure the voltage and current of the slit plate, grid 1, and grid 2 respectively. Each RFEA module has a set of three power supplies with different current and voltage capabilities. The slit plate power supply can drive voltages in the range 0 to -300 V and can be used to measure currents up to 3 A. In the

measurements presented in this thesis a current was never measured above ~ 0.23 A due to short high current bursts on the power supply triggering a safety shut down. Both grid power supplies are low current and able to measure a maximum of 0.2 A; the discriminating grid (grid 1) can sweep between 0 and +800 V in 20 μs and the electron repelling grid (grid 2) can drive voltages in the range 0 to -300 V. The power supplies are connected to the RFEA probes by 20 - 25 m of triaxial cables with a capacitance of 94 pF/m, however this has been compensated for in the design of the power supplies.

Low current signals measured on the RFEA collector plate ($\sim$ 1 - 100 μA) will be lost in noise when transferring between the probe and the data acquisition system. To reduce noise on such low signals, the original measured signal is amplifier by a micro-current amplifier close to the probe head and converted into a voltage signal which can be read by data acquisition systems. The signal recorded by data acquisition can be converted into the correct units by the conversion 1 V = 30.3 μA.

3.3 Data analysis and interpretation

3.3.1 Steady state T_i measurements

Steady state T_i measurements are made by voltage sweeps every 0.5 ms. A typical slit plate, grid 1 and grid 2 voltage time trace can be seen in figure 3.14. Density fluctuations, which have been shown to be due to localised filaments [70], mean that for a static grid voltage spikes are observed as a function of time in the collector current measured by the midplane RFEA. For a swept grid these spikes can occur at any time during the voltage sweep, see figure 3.14 for the collector response at the midplane (I_{col}^{mid}). In order to produce a fit to the data which represents the mean ion temperature in the SOL plasma rather than one dominated by fluctuations, four voltage sweeps have been combined and binned to produce an I-V characteristic with an approximately exponential form. Four sweeps in voltage have been used for measurements at the midplane because it is the minimum number that allows fits with $\chi^2/ndf \sim 1$ on average, where ndf is the number of degrees of freedom and χ^2 is the statistic determining how far in terms of standard deviations the fit is from the experimental data [71], whilst maximising the time resolution of the measurements. With a sweep rate of 0.5 ms measurements of T_i and V_s are available at the midplane every 2 ms which is equivalent to a maximum movement of 5 mm of the reciprocating probe.

At the divertor the measured current signals (see I_{col}^{div} in figure 3.14) appear smoother than at the midplane RFEA. This is most likely due to the toroidal smoothing of spatially localised filament structures through transport in the flux-expanded region close to the x-point [72]. Two sweeps of the grid 1 voltage are combined and binned before fitting to increase the quality of the fitted T_i measurements, providing T_i and V_s measurements every 1 ms. The radial profiles at the

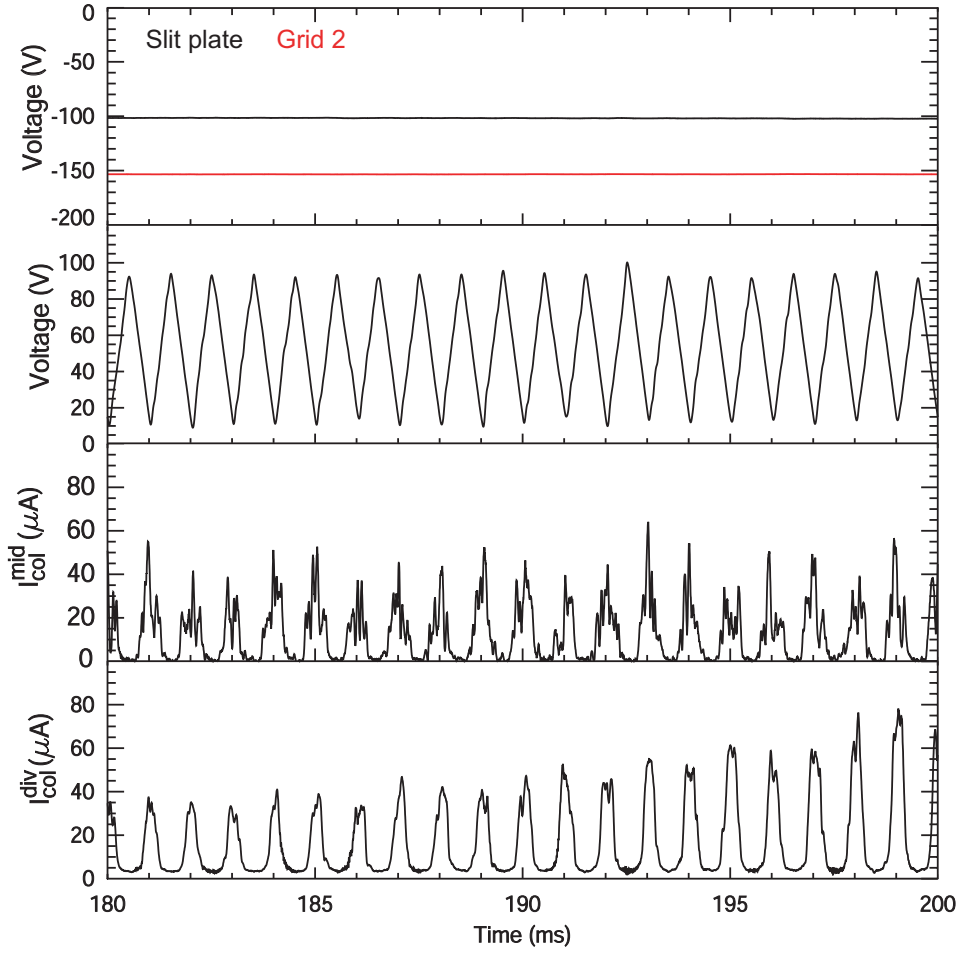

Figure 3.14: Typical time traces for the slit plate, grid 1 and grid 2 voltages along with the collector current response for the midplane RFEA, I_{col}^{mid}, and the divertor RFEA, I_{col}^{div}. The response to the grid 1 voltage sweeps can be seen by the envelopes of current on the I_{col} signals. The 'noisy' response in I_{col}^{mid} is due to the filamentary structures at the midplane SOL. For I_{col}^{div} signals the envelopes of current are noticeably smoother than I_{col}^{mid}.

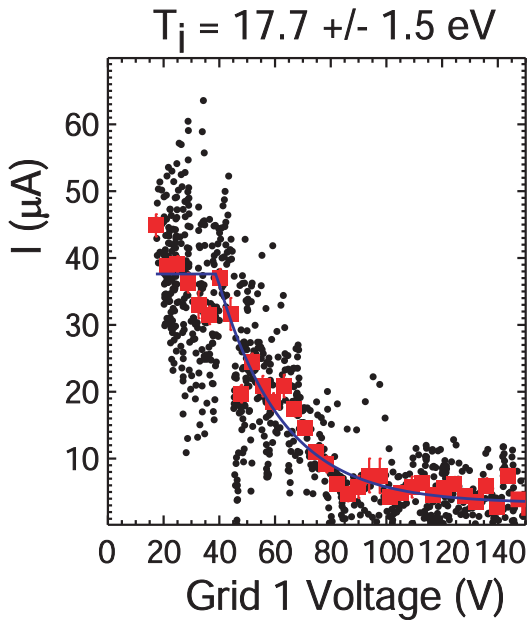

Figure 3.15: Typical current-voltage (I-V) characteristic as measured at the midplane. The scatter in the fit is due to the filamentary structures at the midplane over four combined voltage sweeps.

target are obtained from the natural movement of the strike point ($\sim$ 1 m/s) which allows a resolution of $\sim$ 1 mm across the target. This is more than adequate for T_i profiles which are binned at 1 cm due to scatter in the radial profiles.

Typical collector currents as a function of grid 1 voltage can be seen in figure 3.15 and figure 3.16 for the midplane and divertor respectively. For $V_{grid1} \leq V_s$ a linear fit has been used for the data to aid finding the correct beginning of the exponential fit, because this is only valid for $V_{grid1} > V_s$. A constant has also been added to the fit, I_{off}, to account for any current offsets due to the electronics of the system ($\leq$ 5 μA). The equation used to fit experimental measurements is shown in equation 3.13.

$$I_{col} = \begin{cases} I_0 + I_{off}, & \text{if } V_{grid1} \leq V_s \\ I_0 exp\left(\frac{-(V_{grid1}-V_s)}{T_i}\right) + I_{off}, & \text{if } V_{grid1} > V_s \end{cases} \tag{3.13}$$

Midplane T_i profiles

Profiles of T_i are obtained from the movement of the RP during the plasma shot. The reciprocation allows measurements during the motion towards and away from the plasma during a stationary phase. The position of the real radius of the probe is translated into ΔR_{LCFS} by using the position of the outer radius of the plasma in time from reconstruction of the magnetic equilibrium using the EFIT code on MAST [73, 74]. For midplane measurements several repeated shots are performed with different reciprocations to increase profile statistics.

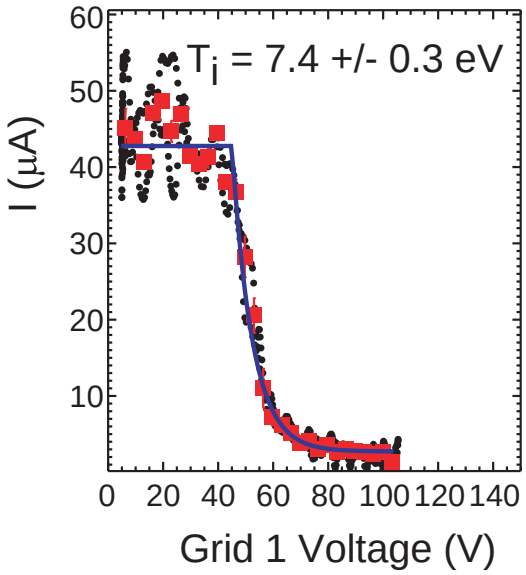

Figure 3.16: Typical current-voltage (I-V) characteristic as measured at the divertor. There is less scatter in the data in the exponential region since there are only two voltage sweeps and the filamentary structures are only seen for $V_{grid1} \leq V_s$.

T_e comparison from Thomson scattering

T_e measurements by Thomson scattering are extracted at the location of the RP as a function of time in the discharge to allow a direct comparison of T_i and T_e. T_e measurements are translated in ΔR_{LCFS} space by the same method as T_i measurements. For temperature profiles, T_e measurements in repeated shots are combined as with the T_i measurements so that average trends of T_i/T_e across ΔR_{LCFS} can be investigated.

Divertor T_i profiles

Since profiles of T_i are obtained from a fixed position in the divertor target by the strike point moving in time, measurements as a function of time need to be changed to ΔR_{LCFS} space. To give accurate profiles the position of the strike point in time must be well known. In MAST the position of the strike point can be determined from EFIT [73, 74], however it is known that there are discrepancies in the strike point position relative to the peak location determined from target Langmuir probes (LP) or IR thermography. We have chosen to determine the LCFS at the target as the peak in j_{sat} as measured by the LP. Figure 3.17 shows the difference between EFIT and LP measurements of the position of the strike point.

We define ΔR^{tgt}_{LCFS} to be the distance between the RFEA (0.985 m) and the peak of the radial j_{sat} profile measured by the radial array of target Langmuir probes. It is likely that the actual strike point will be up to ~ 1 cm further into the private flux region than the position found by the peak in j_{sat} measured by LP since particles diffuse into the private flux region. However, since radial profiles of both T_e by LP and T_i by RFEA are constructed with the same definition of ΔR^{tgt}_{LCFS} the

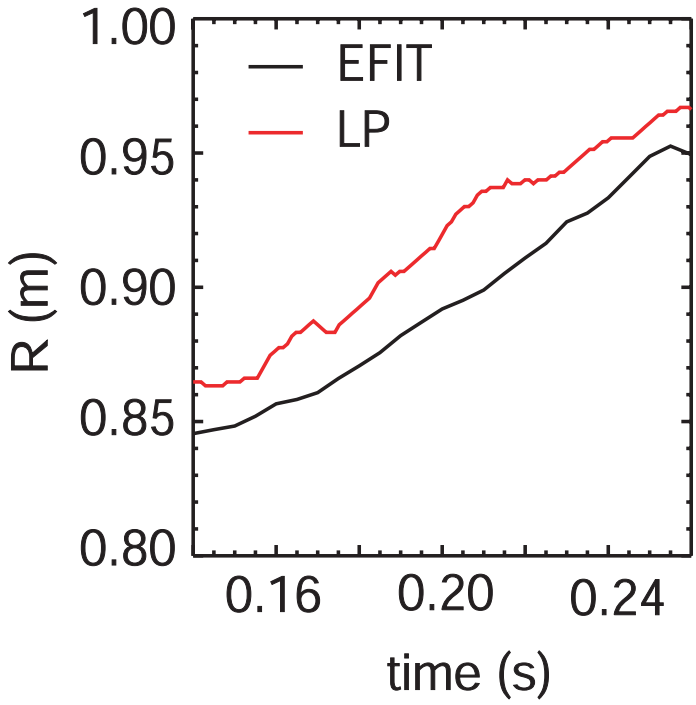

Figure 3.17: Motion of the strike point in time as measured by magnetic reconstruction using EFIT. This is compared to the position of the strike point defined by the maximum j_{sat} measured by LP. It can be seen that the two methods can disagree by ~ 2 cm.

measurements are comparable. Since the LP are in radial arrays in the divertor it is possible to measure profiles of j_{sat} in time during a plasma discharge. From these profiles the position of the peak j_{sat} can be found in time and used to give what we have defined as ΔR^{tgt}_{LCFS} by subtracting the position of the DSF (R = 0.985 m). This gives T_i data in the form of a radial profile in ΔR^{tgt}_{LCFS} space. The j_{sat} measurement from the RFEA slit plate is also translated into ΔR^{tgt}_{LCFS} space so it can be used as a comparison to j_{sat} profiles from LP to confirm the measurements of T_i and T_e are relatively aligned.

T_e comparison from divertor Langmuir probes

For comparison to T_i measurements, T_e measurements by LP are used to make a composite profile over the time period in which RFEA measurements are taken. Profiles of j_{sat} and T_e are averaged in 10 ms time windows. The peak in j_{sat} for each averaged profile, R^{peak}_{jsat}, is taken to be $\Delta R^{tgt}_{LCFS} = 0$ m and each 10 ms average profile is shifted by the corresponding R^{peak}_{jsat} so that all averaged profiles are centered on j^{peak}_{sat} in ΔR^{tgt}_{LCFS} space. The centred profiles of j_{sat} and T_e (also shifted by R^{peak}_{jsat}) are binned at 1 cm to give averaged profiles of T_e and j_{sat} for T_i comparison.

A check is made to ensure that averaged profiles are valid in the time windows measured by the RFEA. Two Langmuir probes radially either side of the DSF are averaged together and plotted in time, then translated to ΔR^{tgt}_{LCFS} profiles by the same method as the RFEA data. An example of individual probe measurements

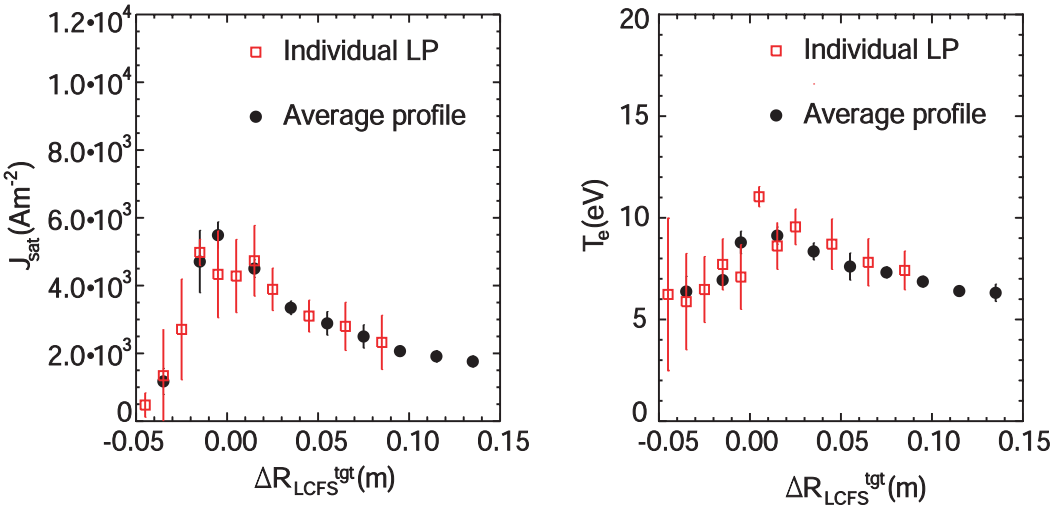

Figure 3.18: Measurements of the T_e and j_{sat} profiles from both the averaging method and measured by individual Langmuir probes close to the position of the DSF. The averaging method can be seen to agree well with the probes at the DSF position showing that the profiles do not change dramatically over the time window in which the RFEA data is taken.

(T_e and j_{sat}) compared to averaged profiles can be seen in figure 3.18. Using the averaged profile method, j_{sat}^{RFEA} matches to j_{sat}^{LP} confirming the profiles of T_i and T_e are relatively correct. The measurements of j_{sat} from both diagnostics will be shown along side T_i and T_e profiles in chapters 4 and 5.

3.3.2 Average ELM T_i analysis

An ELM is a transient event which lasts several 100 μs but is composed of filaments that would pass a probe at the midplane in $\sim$ 20 μs. This makes the energy and temperature of ions in ELM filaments difficult to measure due to the fast timescales. At the divertor, filamentary effects to some extent are smeared out due to the X-point and parallel transport timescales so that changes due to the ELM arrive slower than filaments pass the midplane RFEA. Despite this factor the RFEA probe is still required to sweep quickly to capture the evolution of the ELM arriving at the target.

Although the grid 1 RFEA power supplies are capable of producing one sweep every 20 μs this induces a large capacitive signal in the cables which can be challenging to remove. For this reason an average ion temperature measurement for the peak of ELMs arriving at the target can be measured to give an upper bound on the ELM T_i using a similar technique to that used by Kočan for measurements of ELM T_i at the midplane on ASDEX Upgrade [45]. A different waveform is used for the discriminating grid so that the voltage on grid 1 is swept at a slow rate, $\sim$ 40 Hz. We assume that on the timescale in which an ELM occurs the voltage change on grid 1 is negligible and therefore the voltage can be considered to be constant during the ELM. Assuming we measure a number of similar ELMs arriving at the

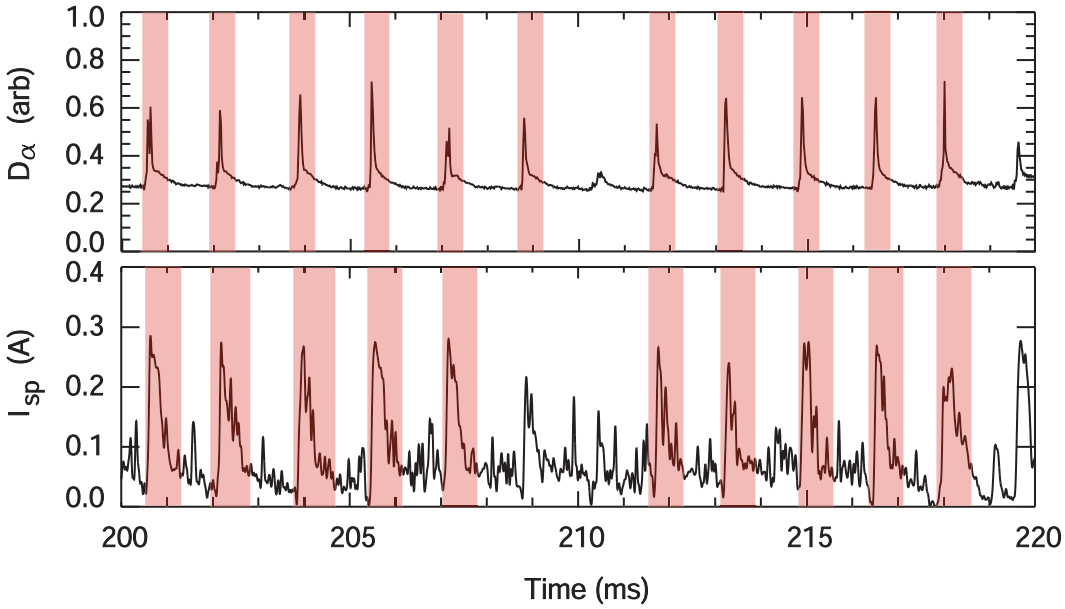

Figure 3.19: Time traces to show how similar ELMs are identified. The top trace is the D_α signal which signifies the presence of an ELM. The red highlighted areas shows similar sized ELMs. The second trace shows the current signal on the RFEA slit plate, I_{SP}. Peaks in current correspond to ELMs arriving at the RFEA slit plate. The red highlighted sections on this trace identify ELMs which are similar in D_α and similar at the RFEA probe. These ELMs can be used to give an average T_i^{ELM}.

target RFEA during an ELMy H-mode period of the plasma, the temperature for an average ELM arriving at a particular target radius can be determined from an I-V characteristic made from a number of I_{ELM}^{peak} signals at the collector. Similar ELMs are defined by the D_α signal at the target and the current signal on the RFEA slit plate, I_{SP}. Signals for typical traces of D_α and I_{SP} as a function of time are shown in figure 3.19; the red highlighted sections on the top D_α trace show similar ELMs arriving at the target. Similar ELMs arriving at the RFEA are determined by peak I_{SP} values. The second time trace in figure 3.19 shows the current signal on the RFEA slit plate, I_{SP}; the highlighted peaks show the similar ELMs arriving at the RFEA. These ELMs are used to give the average T_i^{ELM} from a composite I-V characteristic.

To produce a composite I-V characteristic from similar ELMs during an ELMy H-mode period of the plasma, the position of the strike point with respect to the RFEA must be fixed. The plasma scenario is adapted, by changing the current in the divertor coils, to allow a fixed position of the strike point during the time the data is collected. By fixing the position of the outer divertor leg at different target radii, a number of average T_i^{ELM} measurements can be determined to give radial information for the average ELM temperature. Figure 3.20 shows the time traces of the slit plate current (I_{sp}) which is used as an ELM marker; the voltage on grid 1 which is swept slowly; the collector current response (I_{col}); and the position of the strike point (ΔR_{LCFS}^{tgt}) from IR camera data. The peak ELM signals are visible as

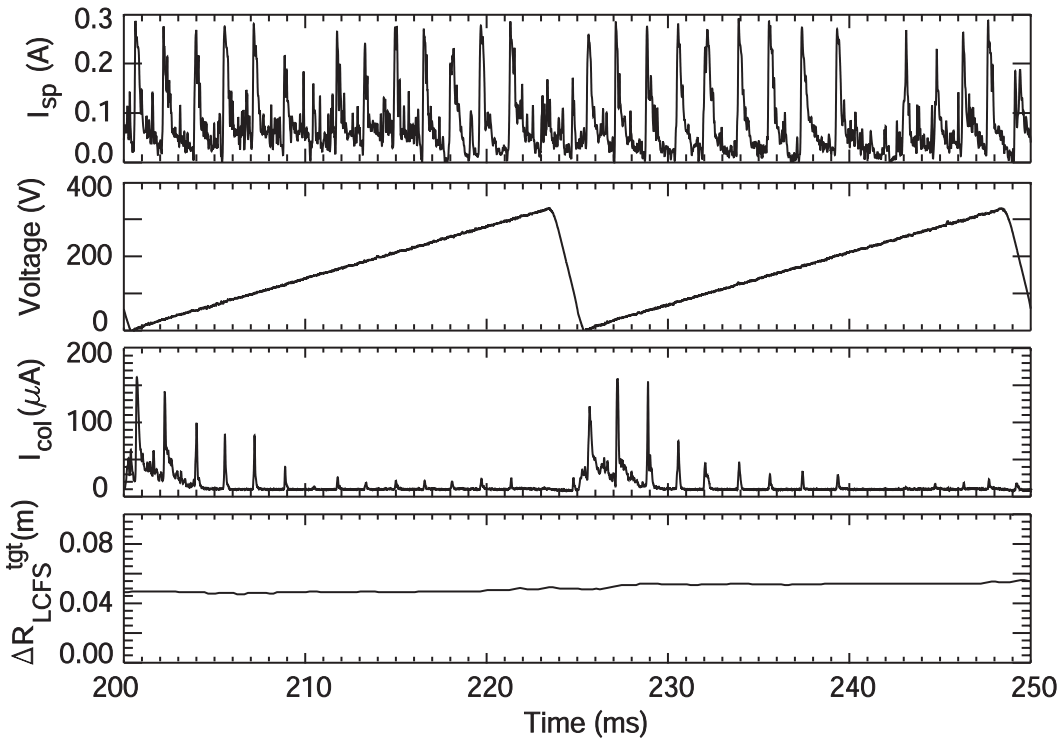

Figure 3.20: Time traces of the signals used to measure average ELM ion temperatures. The slit plate current, I_{sp}, is used to determine similar ELMs at the RFEA; the voltage on grid 1 is shown with a slow sweep to +300 V. The response of the ELM ions to the grid 1 voltage can be clearly seen as the peak I_{col} signals associated with ELMs reduces at higher grid 1 voltages until almost all the ions associated with ELMs arriving at the RFEA are suppressed. Also shown is the relative position of the RFEA to the strike point. This is fixed for the period of measurements taken, in this case $\sim$ 5 cm from the strike point.

spikes in I_{col} and can be seen in figure 3.20. The magnitude of I_{col} at the ELM peak reduces as the voltage on grid 1 increases until all currents corresponding to ELMs reaching the RFEA are suppressed.

For similar ELMs the peak I_{col} during the ELM, I_{col}^{ELM}, is plotted against the corresponding V_{grid1} value. Provided a sufficient number of similar ELMs are measured, I-V points are fit to give an average ion temperature of the ELMs at the target for the given distance from the strike point.

3.3.3 Fast-time ELM T_i analysis

The RFEA has been operated in the 'fast swept' voltage mode in an attempt to measure V_s and T_i during an ELM arriving at the target. The fast sweeping of grid 1, $\sim$ 20 kHz, causes capacitive effects on the collector signal because the swept grid and the collector plate act as a parallel capacitor. In order to fit the I-V characteristics the capacitive signal must be removed from I_{col}. The capacitance can be estimated from $C = \frac{\epsilon_0 A}{d}$, where A is the surface of grid 1 or the collector, d is the separation between the them and the permittivity of free space, $\epsilon_0 = 8.85 \times 10^{-12}$ $m^{-3}kg^{-1}s^4A^2$, which gives C $\sim$ 1 pF. This capacitance matches well to the

capacitive signal seen on the collector when using $I = C\frac{dV}{dt}$, however due distortion of the voltage waveforms by the power supplies this capacitive function is not accurate enough to leave the pure plasma signal response when removed from the measured I_{col} signal. The alternative approach is to remove the average I_{col} signal from the previous five 'up-down' sweeps before the ELM. The analysed ELM signal at the collector is stronger than the removed background signal by a factor of about three. This leaves the current at the collector due to the ELM contribution only since the background plasma current is removed with the capacitive signal. During one voltage sweep the SOL plasma is not in steady state due to the ELM arrival, therefore up and down sweeps are fitted separately to maximise time resolution. Depending on the analysable signal of the ELM, two to eight I-V characteristics are analysed through the ELM rise and peak.

The slit plate power supplies have experienced problems during ELM measurements because of the high divertor currents [17]. The current that can be measured by the slit plate is limited and when this limit is reached the power supply's safety feature temporarily turns off the voltage supplied to the probe. When the voltage on the slit plate is not sufficiently high the RFEA can become space charge limited (see section 3.2.2) and therefore measurements by the RFEA cannot be used. ELMs measured by the fast-time analysis technique have been carefully selected to ensure sufficient voltage is applied to the slit plate during the I-V characteristics analysed.

3.4 Summary

Two RFEAs have been designed and installed on MAST at the midplane and divertor to allow measurements of the ion temperature in the SOL. The limitations and various operational modes of the probes have been discussed. The probes will be used to make measurements in the MAST SOL in L-mode and inter-ELM H-mode plasmas results of which will be discussed in chapters 4 and 5 respectively. Methods of making the first ELM ion temperature measurements at the divertor have been discussed and results from these methods will be discussed in chapter 5.

Chapter 4

Results from low plasma confinement studies

Three sets of discharges have been studied in the low confinement (L-mode) regime; four densities in ohmic plasmas with plasma current, I_P = 400 kA; three heating powers at high density with I_P = 900 kA; and three ohmic plasmas with different plasma currents. All plasmas are deuterium with vacuum magnetic field at $R = 0.7$ m of $B_t = 0.58$ T. The plasma current, line-averaged core density, $\bar{n}_e$, and neutral beam heating power, P_{NBI}, were varied over the discharges studied. These values along with the upstream LCFS values for T_e and n_e can be seen in table 4.1 for all the L-mode discharges studies. An example time trace for the plasma current, I_P, and the line average density, $\bar{n}_e$, can be seen in figure 4.1 for the lowest and highest density plasmas measured at I_P = 400 kA. All discharges are in a double-null magnetic configuration.

All target data profiles are compared to measurements made by target Langmuir probes (LP) of T_e and j_{sat}. Measurements made by the midplane RFEA of upstream T_i are compared to T_e measurements made by the Thomson Scattering (TS) system. Divertor ion temperature profiles can be measured due to the sweeping of the strike point at the divertor known as the 'divertor leg', however measurements are restricted to the radial range swept by the strike point relative to the RFEA position.

Table 4.1: L-mode discharge parameters for the range of discharges studied.

Shot #	I_P (kA)	P_{NBI} (MW)	$\bar{n}_e$ (m^{-3})	T_e^{LCFS}	n_e^{LCFS} (m^{-3})
26798	400	0	1.2×10^{19}	25.2	3.1×10^{18}
26800	400	0	1.4×10^{19}	23.8	5.4×10^{18}
26801	400	0	1.6×10^{19}	23.1	6.6×10^{18}
26802	400	0	2.2×10^{19}	14.0	8.8×10^{18}
26805	900	0	2.6×10^{19}	22.8	5.4×10^{18}
26786	900	1.2	2.6×10^{19}	17.7	9.0×10^{18}
27734	900	2.0	2.6×10^{19}	19.7	7.7×10^{18}
26803	600	0	1.6×10^{19}	22.8	8.1×10^{18}
27736	750	0	1.6×10^{19}	26.0	5.5×10^{18}

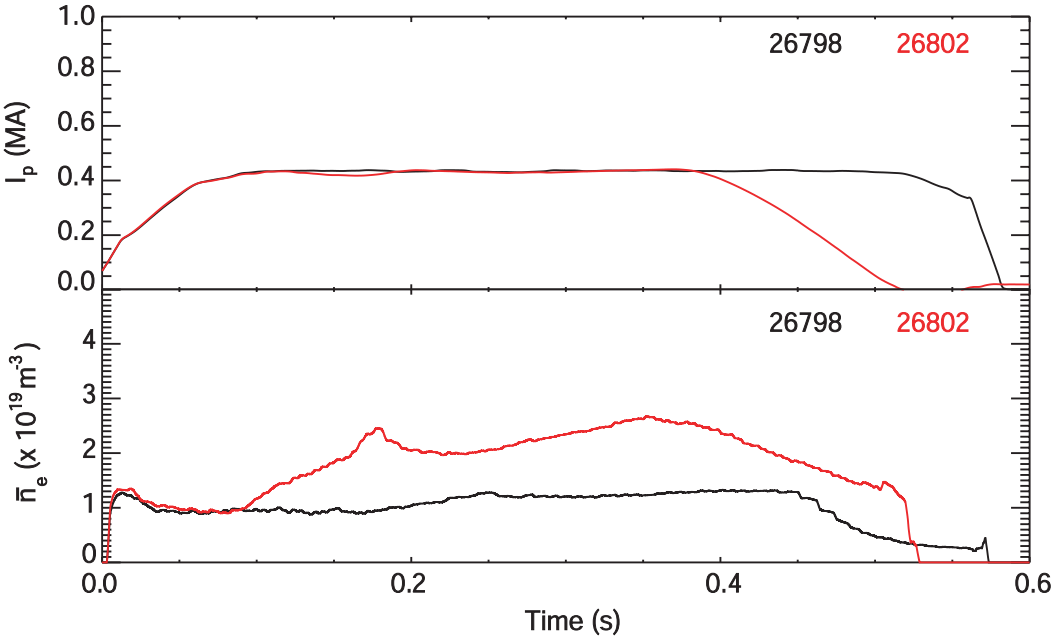

Figure 4.1: (a) Plasma current (I_P) traces for the L-mode discharges discussed and (b) average density ($\bar{n}_e$) traces for the lowest and highest density plasmas studied at I_P = 400 kA.

From the available radial profile, any data taken whilst the slit plate is not applying sufficient negative voltage ($\sim$ -100 V) must be disregarded since the analyser is space charge limited. Further discussion of the space charge limitations can be found in section 3.2.2. All RFEA and LP measurements are binned in radial profiles weighted by the error associated with the goodness of fit of the temperature. The displayed error bars are the standard deviation from each radial binned measurement. J_{sat} error bars are from the standard deviation of the radial bins.

4.1 Divertor T_i profiles

4.1.1 Density Scan

The densities used for the ohmic I_P = 400 kA scan can be seen in table 4.1 and figure 4.1 for the lowest and highest densities. Measurements are made of T_i and T_e as a function of distance from the LCFS at the target. The LCFS location as a function of time is defined as the peak in the j_{sat} profile measured by the LP. Figure 4.2 shows the target profiles in the lowest density discharge, $\bar{n}_e = 1.2 \times 10^{19}$ m^{-3}, measured as a full radial profile (ΔR^{tgt}_{LCFS} = -0.05 $\rightarrow$ 0.15 m) of T_i and T_e. Peak values of $T_i \sim 15$ eV around the strike point are seen. Higher values are measured in the far SOL, however, there are larger error bars on this data. Through all of the SOL $T_i \geq T_e$. T_e near the strike point is slightly lower than the peaked T_i in this region. Both electron and ion temperatures peak further into the SOL relative to the peak in j_{sat}; offset from one another radially by $\sim$ 2 cm. There is a broader peak in the T_i profiles and T_i remains higher than T_e into the private plasma.

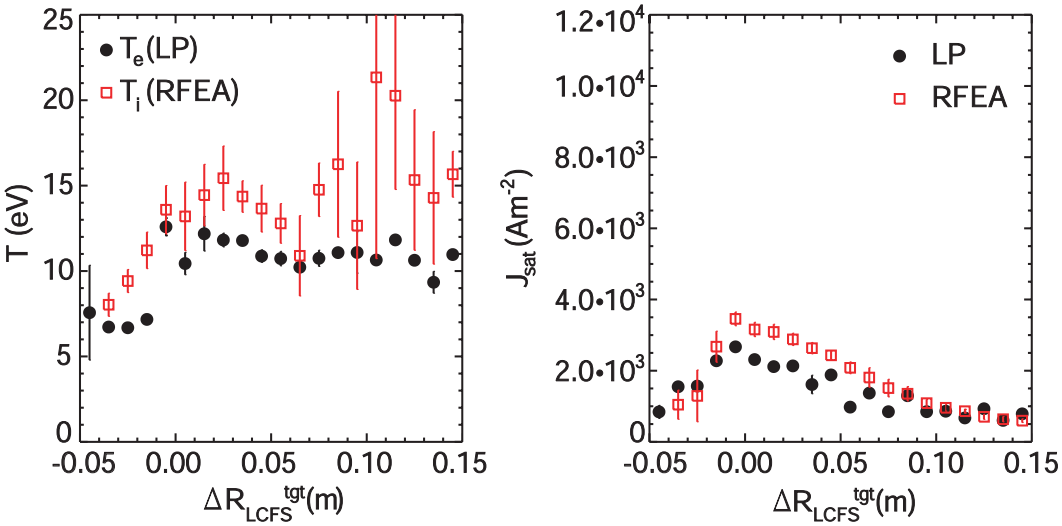

Figure 4.2: Low density ($\bar{n}_e = 1.2 \times 10^{19}$ m^{-3}) discharge with T_i measurements from RFEA shown by red squares and T_e measurements by LP shown by solid black circles. Also shown are j_{sat} measurements by LP (solid black circles) and j_{sat} measured by the slit plate of the RFEA (red hollow squares).

Figure 4.3 shows that as the plasma density is increased to $\bar{n}_e = 1.4 \times 10^{19}$ m^{-3} the temperatures at the target reduce to ~ 10 eV with T_i remaining greater than T_e. Profiles of T_i and T_e are flat in the SOL with marginally higher ion temperatures ($T_i \sim 10$ eV) than electron temperatures ($T_e \sim 8$ eV). In the private plasma $T_i \geq T_e$, with the peak in T_i further into the private plasma than the peak in T_e. Values of both ion and electron temperatures are lower than in the previous plasma discharge with lower density. This is expected since, due to pressure balance along the SOL, the target temperature, T_t, scales with the upstream density, n_u, as $T_t \propto n_u^{-2}$.

Increasing the density further to $\bar{n}_e = 1.6 \times 10^{19}$ m^{-3}, both T_i and T_e reduce as shown in figure 4.4. T_i and T_e have very flat profiles across both the SOL and private plasma with no real peak at the strike point. Average ion and electron temperatures are ~ 6 eV with $T_i/T_e \sim 1$. The section of the radial profile without T_i measurements is due to space charge limiting as mentioned previously, see section 3.2.2. There are measurements missing in figure 4.5 for the same reason.

Figure 4.5 shows results from the highest density discharge with $\bar{n}_e = 2.2 \times 10^{19}$ m^{-3}. The measurements of T_i in the far SOL are low, $T_i \leq 5$ eV, and $T_i/T_e \sim 1$. The T_e profile is flat without peaking at the strike point. Again both T_i and T_e values are lower compared to the lower density plasmas.

A comparison of T_i profiles for the range of densities measured ($\bar{n}_e = 1.2 \rightarrow 2.2 \times 10^{19}$ m^{-3}) is shown in figure 4.6. A clear trend can be seen of decreasing temperature with increased core plasma density. This has also been seen on Tore Supra where T_i decreases more strongly with n_e than T_e [49]. The ratio of ion to electron temperature for all 400 kA discharges is shown in figure 4.7. For all densities, $1 \leq T_i/T_e \leq 1.5$ in the SOL with T_i/T_e tending to unity at higher

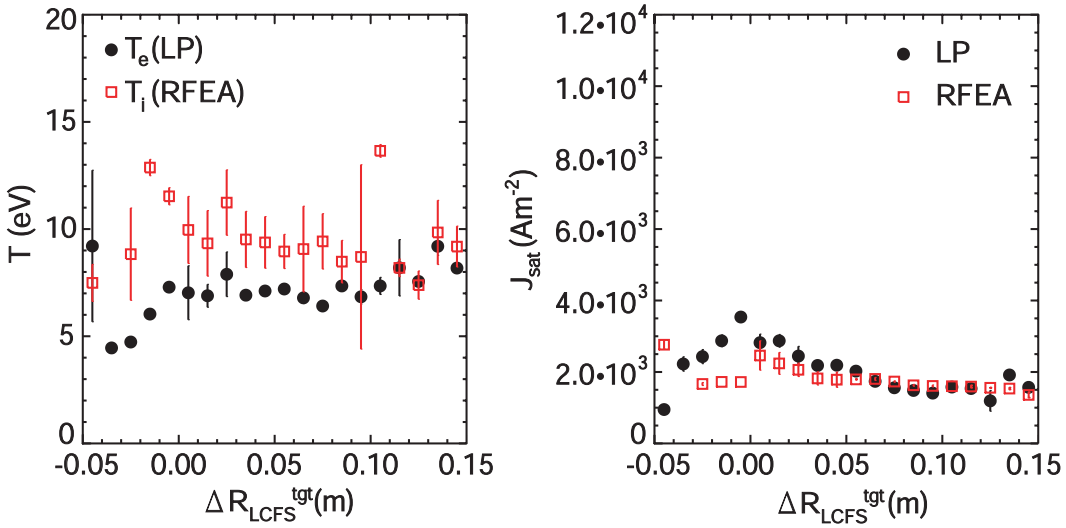

Figure 4.3: Low medium density ($\bar{n}_e = 1.4 \times 10^{19}$ m^{-3}) T_i measurements from RFEA shown by red squares and T_e measurements from target LP shown by black circles. J_{sat} measurements are shown for the LP (black circles) and as measured by the RFEA slit plate (red squares).

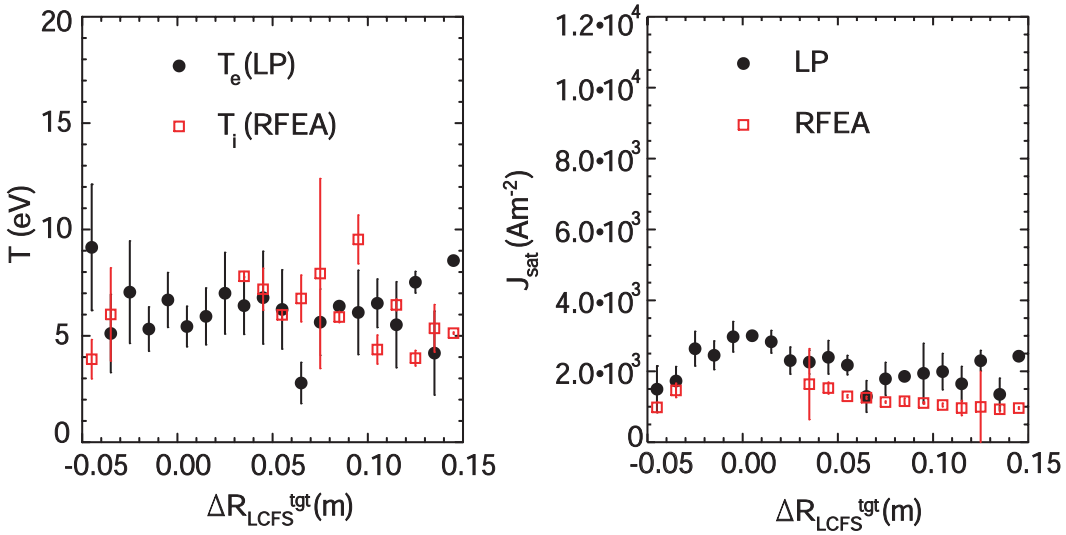

Figure 4.4: High medium density ($\bar{n}_e = 1.6 \times 10^{19}$ m^{-3}) T_i measurements from RFEA shown as red squares and T_e measurements from target LP shown as black circles. J_{sat} measurements are shown for the LP (black circles) and as measured by the RFEA slit plate (red squares).

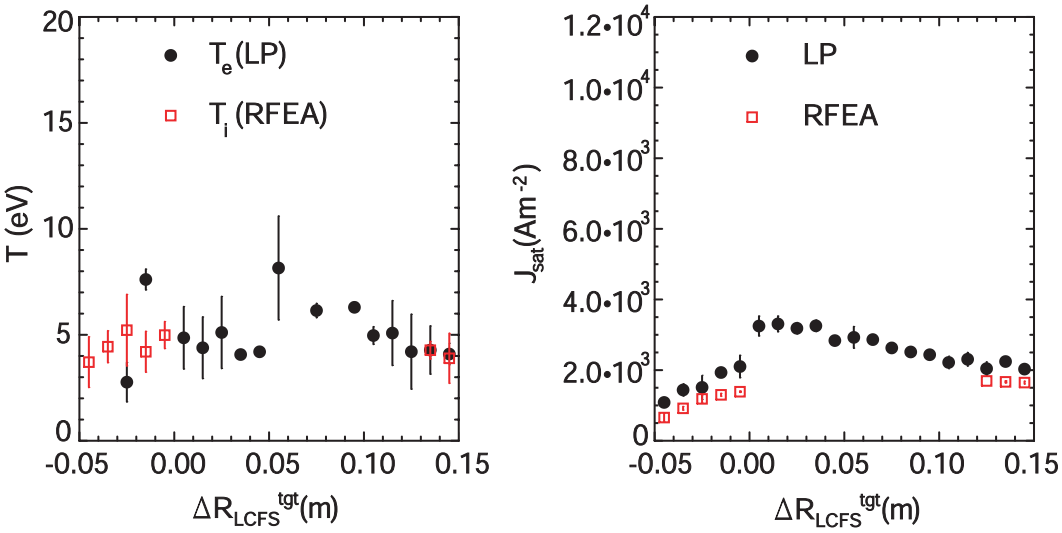

Figure 4.5: High density ($\bar{n}_e = 2.2 \times 10^{19}$ m^{-3}) T_i measurements from RFEA shown by red squares and T_e measurements from target LP shown by black circles. J_{sat} measurements are shown for the LP (black circles) and as measured by the RFEA slit plate (red squares).

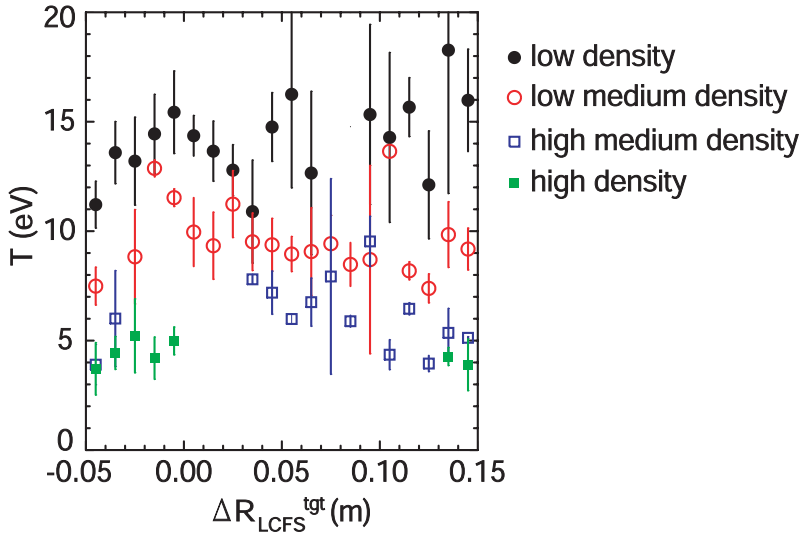

Figure 4.6: T_i profile measurements for 400 kA discharges at $\bar{n}_e = 1.2 \times 10^{19}$ m^{-3} (black solid circles), $\bar{n}_e = 1.4 \times 10^{19}$ m^{-3} (red hollow circles), $\bar{n}_e = 1.6 \times 10^{19}$ m^{-3} (blue hollow squares), and $\bar{n}_e = 2.2 \times 10^{19}$ m^{-3} (green solid squares).

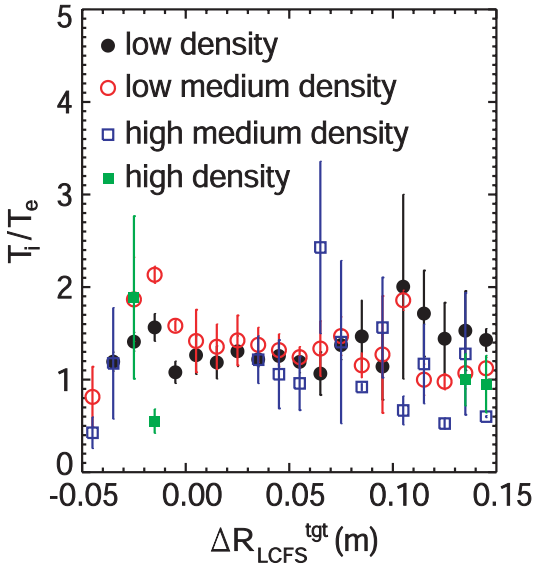

Figure 4.7: T_i/T_e profiles for 400 kA discharges at $\bar{n}_e = 1.2 \times 10^{19}$ m^{-3} (black solid circles), $\bar{n}_e = 1.4 \times 10^{19}$ m^{-3} (red hollow circles), $\bar{n}_e = 1.6 \times 10^{19}$ m^{-3} (blue hollow squares), and $\bar{n}_e = 2.2 \times 10^{19}$ m^{-3} (green solid squares).

densities. The reduction in T_i/T_e with increasing n_e has been seen on a number of other tokamaks [32, 34, 75, 76, 77]. For these low power L-mode plasma discharges, $T_i \sim T_e$ is a good assumption at the target in both the SOL and the private flux region on MAST.

4.1.2 Beam heating power scan

A scan of neutral beam heating power has been conducted to compare target temperatures in an ohmic plasma and two beam heated plasmas with different beam powers. These plasmas have a density of $\bar{n}_e = 2.6 \times 10^{19}$ m^{-3} and $I_P = 900$ kA, see table 4.1 for plasma scenario parameters. The target temperature profiles for the ohmic plasma scenario can be seen in figure 4.8. The electron temperature profile has a shallow temperature fall off with distance from the LCFS at the target with temperatures in the range $T_e = 6$ - 10 eV. In both the near SOL and the private plasma $T_i > T_e$. The ion temperature increases with proximity to the LCFS at the target with a maximum $T_i \sim 13$ eV. In the private plasma T_i decreases with distance from the LCFS at the target. Similarly to the ohmic measurements in plasmas with $I_P = 400$ kA, $1 \leq T_i/T_e \leq 1.5$ across the SOL. The absence of T_i measurements at the strike point is due to the RFEA becoming space charge limited and therefore measurements cannot be used, as with figures 4.4 and 4.5. See section 3.2.2 for details on when the RFEA is space charge limited.

Two plasmas with $I_P = 900$ kA have been measured with different neutral beam heating of $P_{NBI} = 1.2$ and 2 MW but with the same power entering the SOL, P_{SOL}, to determine the effect neutral beam heating has on target ion and electron temperatures. Figure 4.9 shows ion and electron temperature profiles for

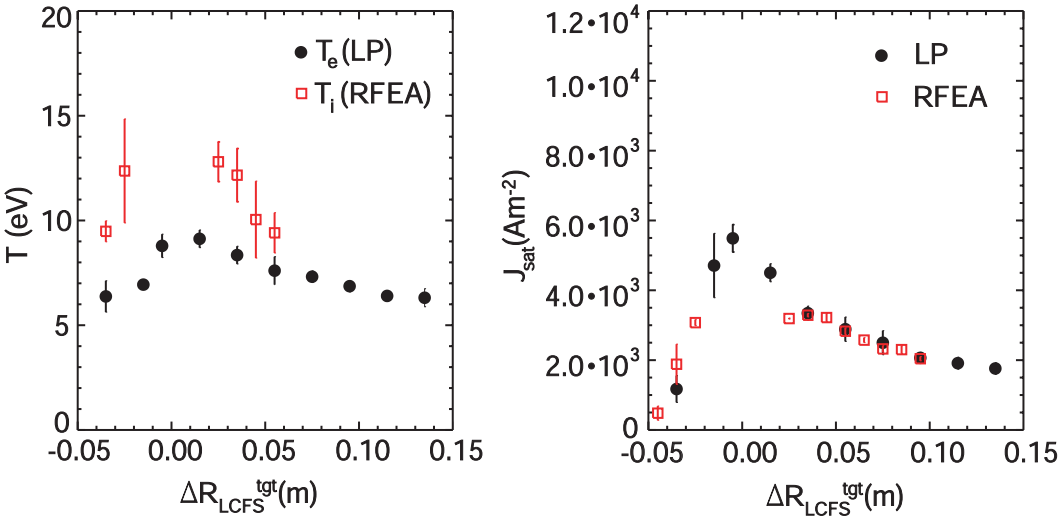

Figure 4.8: High density ohmic T_i measurements by RFEA shown by red squares and T_e measurements from target LP shown by black circles. Also shown are j_{sat} measurements by LP (black circles) and the measurement of j_{sat} from the RFEA slit plate for comparison (red squares).

the discharge with beam heating power of $P_{NBI} = 1.2$ MW. The additional heating power, compared to the ohmic discharge in figure 4.8, causes an increase in both electron and ion temperatures across the majority of the profile. There is marginally more pronounced peaking of the electron temperature at the strike point with a maximum temperature of $T_e = 12$ eV. In the far SOL, however, there is only a marginal increase in electron temperature compared to the ohmic discharge. In the region with T_i measurements it is clear that $T_i > T_e$ with similar fall off lengths for both temperatures of $\lambda_{T_e} = 0.21$ m and $\lambda_{T_i} = 0.22$ m.

Target temperatures measured with a further increase in heating power, at $P_{NBI} = 2$ MW and the same $P_{SOL} \approx 1.8$ MW as the discharge shown in figure 4.9 can be seen in figure 4.10. The T_e profile is similar to the lower beam heating power, with a slight increase of T_e at the strike point. The T_i profile is similar to the discharge with $P_{NBI} = 1.2$ MW. Both ion and electron temperatures have the same fall off length with $\lambda_T = 0.15$ m which is comparable to those measured at the lower beam power. Again in a beam heated L-mode plasma $T_i > T_e$ in the SOL at the target.

The ion temperature profiles for the three discharges with varying beam heating power are shown for comparison in figure 4.11. The effect of the additional heating power can be clearly seen to give an increase in T_i compared to the ohmically heated discharge. This is consistent with other experiments which show additional heating has a more marked effect on T_i than T_e [32, 49, 67, 75]. All three discharges show a clear trend of increasing temperature with proximity to the LCFS at the target, however in the ohmic discharge there is a slightly steeper temperature fall off length of $\lambda_{T_i} = 0.10$ m. Assuming these trends continue as a function of radius towards the strike point, the peak T_i would be larger with beam heating than in the ohmic discharge. Ion temperatures in the ohmic discharge are in the range $T_i = 9$ - 13 eV

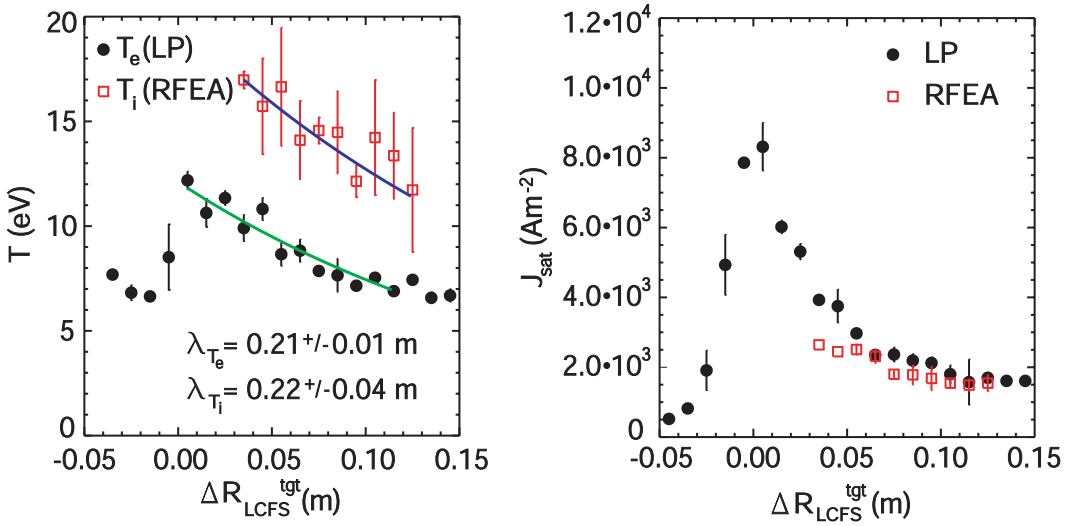

Figure 4.9: High density beam heated (1.2 MW) T_i measurements (red squares) from RFEA and T_e measurements from target LP (black circles). J_{sat} measurements by LP are shown (black circles) along with j_{sat} measurements from the RFEA slit plate (red squares).

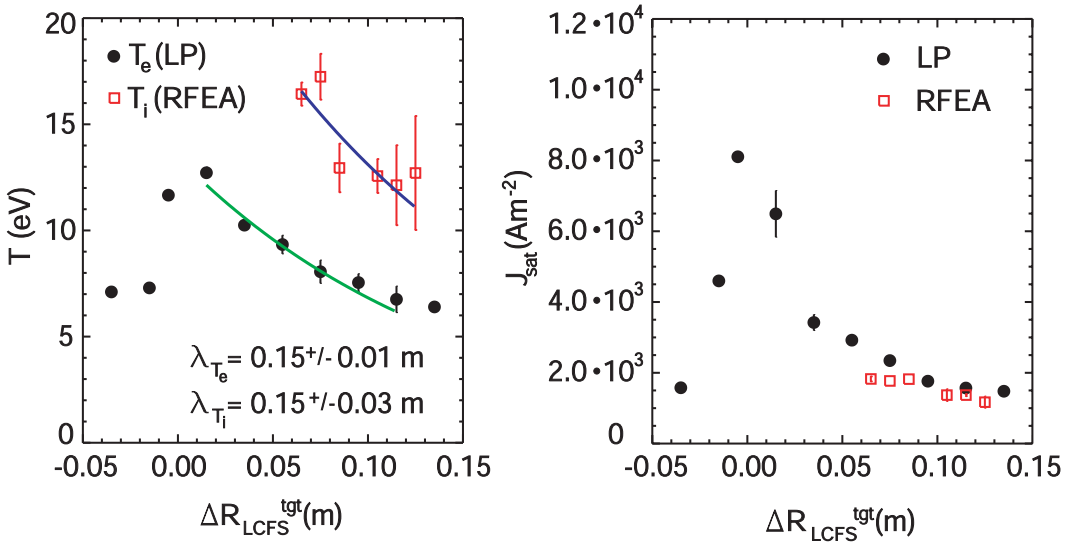

Figure 4.10: High density beam heated (2 MW) T_i measurements (red squares) from RFEA and T_e measurements from target LP (black circles). J_{sat} measurements by LP are shown (black circles) along with j_{sat} measurements from the RFEA slit plate (red squares).

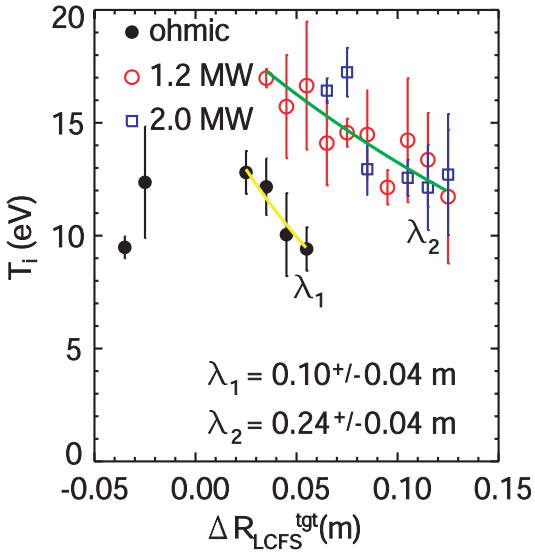

Figure 4.11: T_i measurement profiles for 900 kA high density discharges with ohmic heating (black solid circles), 1.2 MW beam heating power (red hollow circles), 2 MW beam heating power (blue hollow circles).

whereas in the beam heated discharges temperatures are in the range of T_i = 12 - 18 eV. There is no noticeable difference in T_i between the two beam heating powers, P_{NBI} = 1.2 MW and P_{NBI} = 2 MW, which suggests that it is the power entering the SOL which affects the target temperature rather than the fraction of neutral beam heating power compared to ohmic heating. This result shows an increase of T_i at the target when P_{SOL} is increased since in the ohmic discharge $P_{SOL} \approx 0.9$ MW whereas in the two discharges with additional NBI heating P_{SOL} is doubled, $P_{SOL} \approx 1.8$ MW. Therefore the power entering the SOL has a stronger effect on the target temperature than the fraction of neutral beam heating. This has also been seen in Tore Supra even when the additional heating preferentially heats either ions or electrons [78]. It could be that rather than preferential ion heating there is weaker ion to electron coupling because of the increased temperatures [49].

A comparison of T_i/T_e as measured at the target in each of the 900 kA discharges is shown in figure 4.12. In the ohmic discharge $1 \leq T_i/T_e \leq 1.5$ in the SOL. However, for the two discharges with additional heating power (P_{NBI} = 1.2 MW and P_{NBI} = 2 MW) there is a constant value of $T_i/T_e \sim 2$ across the radial profile. This suggests that the additional power to the SOL is carried by the ions. The higher value of T_i/T_e measured in the SOL for the beam heated plasma discharges compared to the ohmic discharge may be related to Larmor orbit effects resulting from the neutral beam heating. The discharges with neutral beam heating have higher temperatures just inside the LCFS (r/a $\sim$ 0.95) of $T_e \approx 70$ eV compared to $T_e \approx 40$ eV for the ohmically heated discharge. Inside the confined plasma it is assumed that ions and electrons are thermally equilibrated so that $T_i = T_e$, therefore, since $\rho_i \propto \sqrt{T_e}$ this means the neutral beam heated discharges will have larger Larmor radii than the ohmic discharge; $\rho_i^{ohmic} \approx 3.8$ mm and $\rho_i^{NBI} \approx 5.0$ mm. Although the size

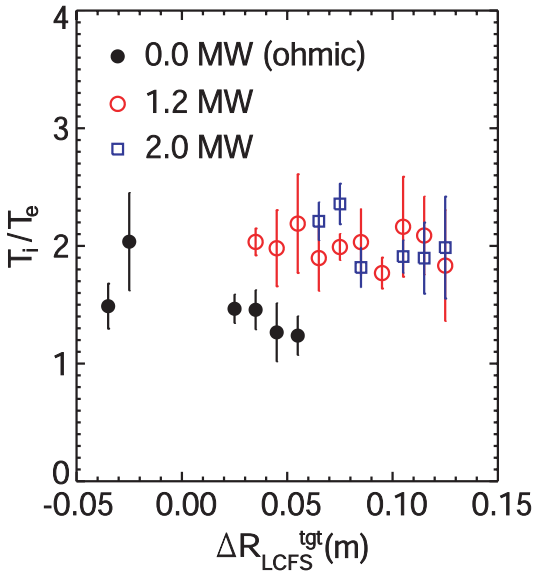

Figure 4.12: T_i/T_e profiles for high density 900 kA discharges with ohmic heating (black solid circles), 1.2 MW beam heating power (red hollow circles), 2 MW beam heating power (blue hollow circles).

of the Larmor radius isn't large enough to extend the hot ions inside the confined plasma into the SOL, the discharge with neutral beam heating is more likely to have hot ions, from the neutral beam heating, entering the SOL without many cooling collisions than the ohmic discharge.

4.1.3 Current scan

Three plasma discharges at the same density ($\bar{n}_e = 1.6 \times 10^{19}$ m^{-3}) have been measured at plasma currents of $I_P = 400$, 600 and 750 kA to investigate the effect of increasing plasma current. The target temperature profiles for the discharge with $I_P = 400$ kA is shown in figure 4.4 and discussed in section 4.1.1. Figure 4.13 shows measurements of ion and electron temperatures for the plasma with $I_P = 600$ kA. The electron temperature profile has a more defined peak in T_e around the strike point with temperatures up to 10 eV than the measurements made in the discharge with $I_P = 400$ kA (figure 4.4). T_i follows the general trend in decreasing temperature with distance from the LCFS at the target with $T_i \geq T_e$ in the region with RFEA measurements. T_i/T_e is marginally higher for the discharge with $I_P = 600$ kA than the discharge with $I_P = 400$ kA on average.

The temperature profiles for the plasma with the highest plasma current, $I_P = 750$ kA, measured at this density can be seen in figure 4.14. The electron temperatures measured in the far SOL are comparable to T_e in the far SOL of the plasma discharge with $I_P = 600$ kA, however the temperature peak is more pronounced at the strike point, reaching $T_e \sim 12$ eV. The profile of T_e in the private flux region has a steeper decrease than the other discharges at this density, reducing to temperatures < 5 eV. Ion temperatures in the near SOL increase with

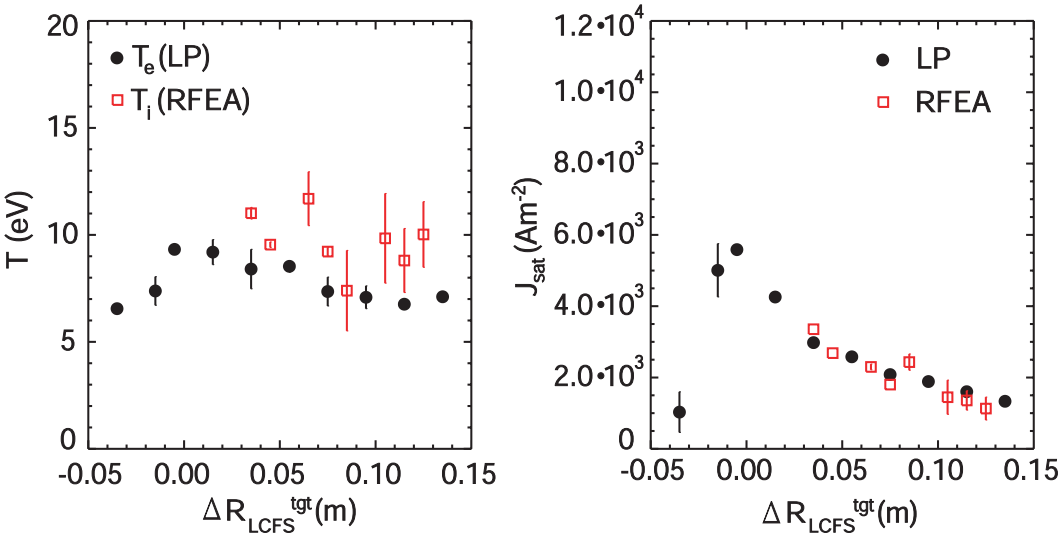

Figure 4.13: Medium high density plasma at $I_P = 600$ kA profile of T_i measurements from RFEA shown in red squares and T_e measurements from target LP shown in black circles. J_{sat} measurements are shown for the LP (black circles) and as measured but the RFEA slit plate (red squares).

proximity to the LCFS at the target. The high value for $T_i \sim 16$ eV in the private flux region may be because temperatures near the strike point peak higher than the SOL values and remain slightly higher than T_e into the private flux region. $T_i \leq T_e$ in the near SOL but in the private flux region $T_i > T_e$.

The ion temperature profiles for the three plasma currents can be seen in figure 4.15. There is no noticeable scaling of temperature with increasing plasma current. T_i profiles for the discharges with $I_P = 400$ and 600 kA are both flat and T_i increases at the higher I_P in the SOL over these two discharges. The highest plasma current measured shows an increase in ion temperature close to the strike point. At the strike point however it is likely that the highest plasma current will have the highest ion temperatures. Also shown in figure 4.15 are T_e and n_e profiles for the three discharges at different plasma currents. The electron temperature does appear to increase marginally with plasma current showing the most noticeable increase at the strike point. It may be that a similar trend would be visible in the ion temperature if measurements closer to the strike point could be made. The target density for the two highest plasma currents are similar however the lowest plasma current, $I_P = 400$ kA, has a lower target density. If the lowest plasma current discharge had the same target density as the two discharges with higher plasma currents then it is likely that the target temperatures would be even lower. This is because at high density the increased number of collisions should reduce target temperatures, enhancing the trend of increasing T_e with increasing I_P.

The ratio of T_i/T_e can be seen as a profile for each plasma current in figure 4.16. On average all discharges show $T_i \sim T_e$ with large errors in the SOL. In the plasma discharge with $I_P = 600$ kA, T_i/T_e is slightly higher across the measured

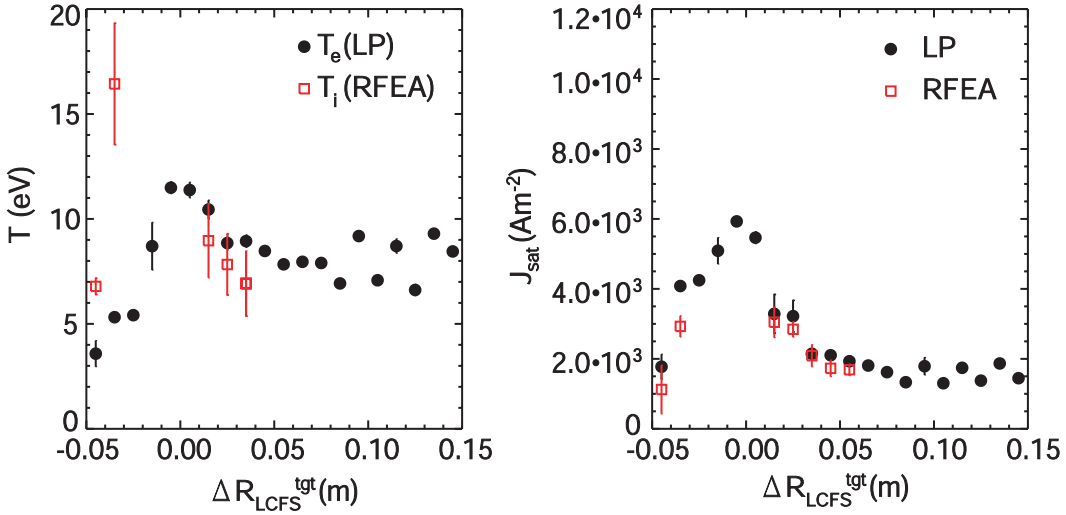

Figure 4.14: Medium high density plasma at I_P = 750 kA profile of T_i measurements from RFEA shown in red squares and T_e measurements from target LP shown in black circles. J_{sat} measurements are shown for the LP (black circles) and as measured but the RFEA slit plate (red squares).

profile with $T_i/T_e \sim 1.3$. In the private flux region T_i/T_e appears to reduce with distance from the LCFS at the target for both discharges measured in this region.

4.2 Comparison with midplane T_i

Measurements at the midplane of T_i by RFEA have been made in the lowest and highest density discharges of the ohmic double null density scan with I_P = 400 kA. This allows a comparison between the T_i/T_e ratio at the midplane (upstream) and at the target for two densities. Figure 4.17 shows midplane T_i measurements made by only side A of the RFEA in both densities compared to T_e measured by Thomson scattering. It can be seen that for both densities T_i/T_e = 1.6 - 3 when accounting for scatter in the measurements.

This confirms previous initial measurements on MAST made with an RFEA borrowed from CEA in Cadarache which showed T_i/T_e = 1 - 2 in ohmic L-mode plasmas [42]. Onion skin modelling (OSM) calculations have shown that if $(T_i/T_e)^{tgt}$ = 1, then $(T_i/T_e)^{up}$ = 2.4 for the low density discharge and $(T_i/T_e)^{up}$ = 1.8 for the high density discharge [40] which is consistent with the measurements made here.

The thermal coupling of SOL ions and electrons, R_{th}, is calculated from the ratio of the parallel SOL transit time, $\tau_{\|}$, to the ion-electron thermalization time, τ_{ie}^{th}, as $R_{th} = \tau_{\|}/\tau_{ie}^{th}$, where

$$\tau_{\|} = \frac{3}{2}\frac{L_{\|}}{c_s} \approx \frac{3}{2}\frac{L_{\|}}{\sqrt{e(T_i + T_e)/m_i}} \tag{4.1}$$

and

$$\tau_{ie}^{th} = \frac{m_i}{2m_e}\nu_{ei}^{-1} = \frac{6\pi^{3/2}\epsilon_0^2 m_i}{\sqrt{2}Ze^4 m_e^{1/2}\ln\Lambda}\left(\frac{T_e^{3/2}}{n_e}\right) \tag{4.2}$$

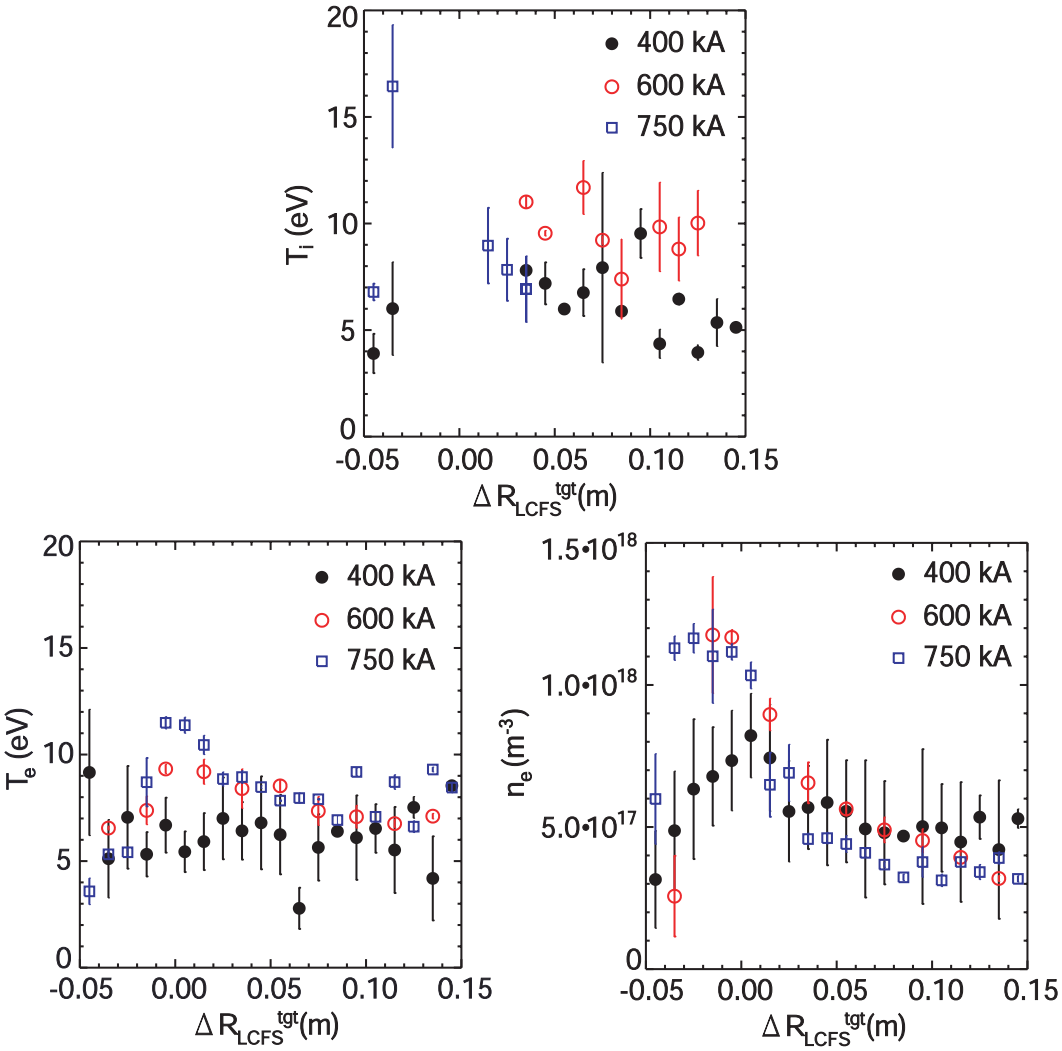

Figure 4.15: T_i measurements profiles for medium high density discharges with I_P = 400 kA (black solid circles), I_P = 600 kA (red hollow circles), I_P = 750 kA (blue hollow circles). Also shown are the corresponding T_e and n_e measurements from LPs at the target.

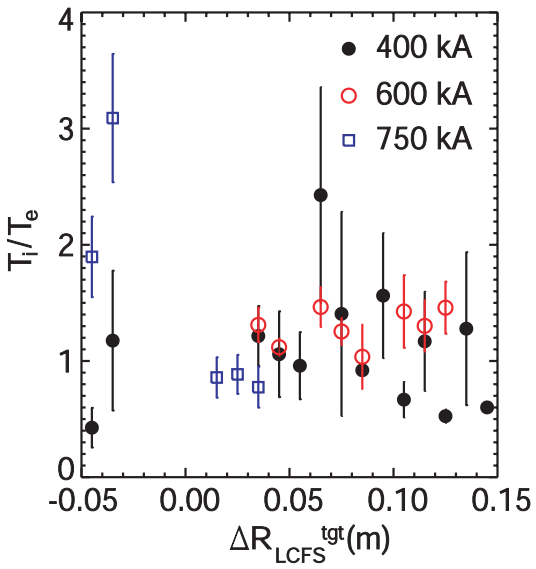

Figure 4.16: T_i/T_e profiles for medium high density discharges with $I_P = 400$ kA (black solid circles), $I_P = 600$ kA (red hollow circles), $I_P = 750$ kA (blue hollow circles).

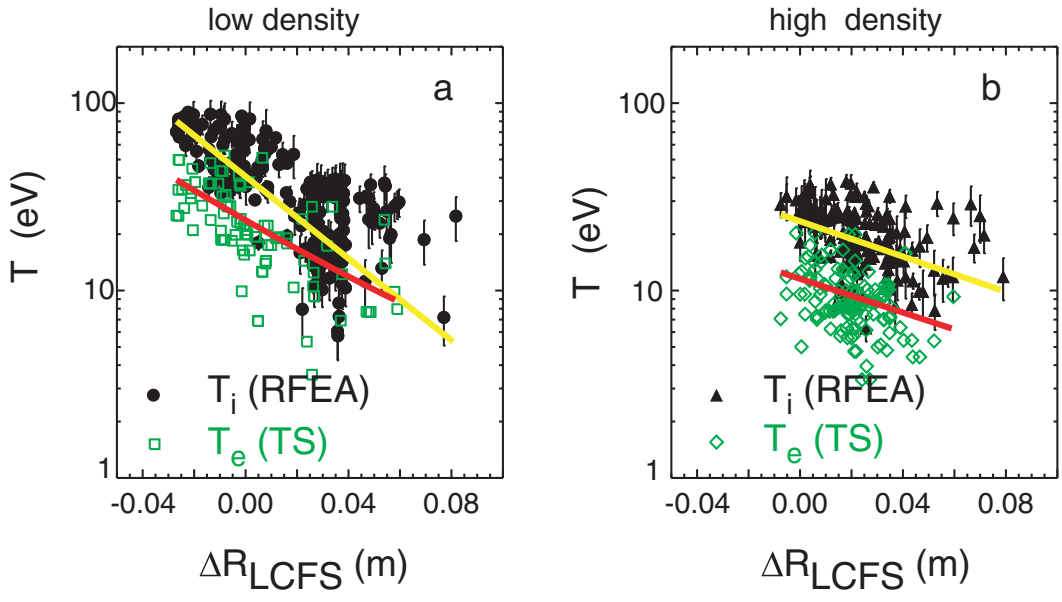

Figure 4.17: T_i measured as a function of LCFS in a low ($\bar{n}_e = 1.2 \times 10^{19}$ m^{-3}) and high ($\bar{n}_e = 2.2 \times 10^{19}$ m^{-3}) density discharge. Results for each density are combined from repeats of the same discharge with different midplane reciprocation depths. The black circles and black triangles are T_i measurements by RFEA and the green squares and green diamonds are T_e measurements from the TS system.

([79] and references therein). The factor of 3/2 in equation 4.1 represents the three degrees of freedom of the particles. $R_{th} < 1$ implies thermally decoupled ions and electrons whereas $R_{th} \gg 1$ implies strongly coupled ions and electrons. In MAST the parallel connection length is $L_{\parallel} \sim 20$ m and n_e, the electron density, was varied over the two discharges investigated by the midplane RFEA. For the high density case the thermal coupling of the ions and electrons reaching the target can be calculated from midplane measurements of $n_e \approx 0.4 \times 10^{20}$ m^{-3} and $T \sim 50$ eV. This gives $\tau_{\parallel} \approx 430$ μs and $\tau_{ie}^{th} \approx 520$ μs, showing thermally decoupled ions and electrons because $R_{th} \approx 4/5$. In the low density case it would be expected that the ions and electrons are further decoupled at the target since $n_e \approx 0.2 \times 10^{20}$ m^{-3} and $T \sim 100$ eV gives $\tau_{\parallel} \approx 300$ μs and $\tau_{ie}^{th} \approx 3000$ μs, meaning $R_{th} \sim 1/10$. These calculations assume $T_i = T_e$ upstream, however it has been shown by the midplane RFEA measurements (figure 4.17) that $T_i \sim 2T_e$. Calculating $\tau_{\parallel}$ for $T_i = 2T_e$ upstream gives reduced coupling of $R_{th} \sim 2/3$ and $R_{th} \sim 1/12$ for the high and low density respectively, showing that ions and electrons at the target are likely to be even more decoupled than the original calculation. This is consistent with low density target measurements which show $T_i/T_e \sim 1.2$ at the strike point. In the higher density the target ions and electrons should still be decoupled however the RFEA measurements in the far SOL show $T_i \sim T_e$. This suggests that closer to the strike point it may be that $T_i > T_e$ although only marginally since the coupling is still stronger than the lower density discharge.

4.3 Summary

Measurements of SOL ion temperatures have been made in a number of L-mode plasma discharges. The measurements made in double-null magnetic configuration plasmas with $I_P = 400$ kA have shown that target temperatures reduce with increased core plasma density, consistent with pressure balance. At the target a ratio of $T_i/T_e \sim 1$ has been measured in ohmic L-mode plasmas. For L-mode plasmas with additional heating by neutral beams higher ion temperatures have been measured at the target. $T_i/T_e \sim 2$ at the target has been measured constantly across divertor target profiles for higher power discharges, achieved through additional neutral beam heating. Measurements by the upstream RFEA have measured $T_i/T_e \sim 2$ in both a high and low density plasma at $I_P = 400$ kA. Since the same plasmas measured at the target show $T_i \sim T_e$ the upstream measurements are consistent with OSM predictions made when $T_i = T_e$ is assumed at the target.

Further upstream measurements will be made and analysed, beyond the scope of this thesis, in order to give more information on the relationship of upstream and target temperatures, particularly in the case of additional heating since this gives interesting target temperature ratios. The plasma discharge at low density with $I_P = 400$ kA, in which upstream and target ion temperature measurements have been

made by RFEA, will be investigated by the 1D fluid model, SOLF1D, in chapter 6.

Chapter 5

Results from high plasma confinement studies

H-mode studies have been carried out at the divertor with the RFEA to investigate the inter-ELM plasma and to make first measurements of T_i in ELMs arriving at the target. Inter-ELM H-mode measurements have been made in several scenarios to investigate the controlled plasma parameters which affect T_i and T_i/T_e at the target. T_i/T_e measured at the target has been used to address the issue of power into the SOL not balancing the total power arriving at divertor targets in inter-ELM H-mode on MAST. The average ELM temperature at the target has been measured for the first time and this has been compared to first measurements of T_i during an ELM made by the alternative fast voltage sweeping RFEA method. T_i measurements of ELMs are compared to modelling of the SOL and measurements of ELMs on other devices.

5.1 Inter-ELM divertor T_i profiles

Four inter-ELM H-mode plasma discharges have been measured by the target RFEA and compared to T_e measurements from Langmuir probes. Two of the discharges are in a connected double null (CDN) magnetic configuration with plasma current I_P = 900 kA and beam powers of P_{NBI} = 1.5 and 3.4 MW respectively; these are scenarios A and B. To investigate the effect of plasma current, T_i has been measured in a further CDN discharge with I_P = 600 kA and P_{NBI} = 3.4 MW; this will be referred to as scenario C. Finally to allow a comparison between different magnetic configurations, a lower single-null (LSN) discharge with I_P = 600 kA and P_{NBI} = 3.4 MW has been studied which will be referred to as scenario D.

The time traces of plasma current, I_P, beam heating power, P_{NBI}, line integrated density, $\bar{n}_e$, and D_α emission, for the plasma discharge with I_P = 600 kA and P_{NBI} = 3.4 MW (scenario C) can be seen in figure 5.1 as an example. A table of the discharge parameters can be found in table 5.1 where densities are averaged over the time data are taken by the RFEA.

Table 5.1: Inter-ELM H-mode discharge parameters for the range of discharges studied.

Scenario	Shot #	Mag Config	I_P (kA)	P_{NBI} (MW)	$\bar{n}_e$ (m^{-3})	T_e^{up} (eV)	n_e^{up} (m^{-3})	ν^*_{ped}
A	27730	CDN	900	1.5	3.0×10^{19}	21.5	1.4×10^{19}	4.11
B	27743	CDN	900	3.4	2.8×10^{19}	15.6	0.9×10^{19}	0.64
C	27870	CDN	600	3.4	2.7×10^{19}	23.4	0.8×10^{19}	1.77
D	27811	LSN	600	3.4	2.8×10^{19}	12.7	0.8×10^{19}	0.97

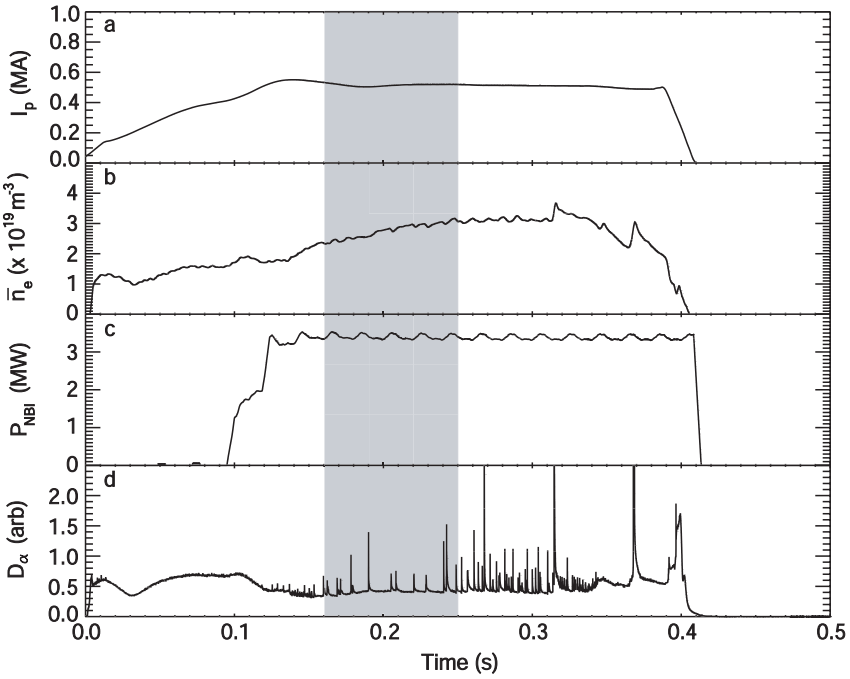

Figure 5.1: (a) Plasma current (I_P) trace, (b) line integrated density ($\bar{n}_e$) trace, (c) additional beam heating power, and (d) D_α emission for inter-ELM H-mode scenario C. The greyed area is the time window in which RFEA measurements are taken.

Inter-ELM H-mode divertor T_i profiles can be measured due to the sweeping of the divertor leg, however measurements are restricted to the radial range swept by the strike point relative to the RFEA position whilst the plasma is in H-mode. From the available radial profile, any data taken whilst the slit plate is not applying sufficient voltage ($\sim$ - 100 V) must be disregarded since the analyser is likely to be space charge limited (see section 3.2.2). Data taken during ELMs arriving at the target are also removed from the data used for T_i profiles since these profiles are measurements of the inter-ELM T_i.

A comparison of target ion and electron temperatures has been made for two discharges with $I_P = 900$ kA and different beam heating powers of $P_{NBI} = 1.5$ MW and $P_{NBI} = 3.4$ MW (scenarios A and B). Scenario A has regular type III ELMs and measurements of T_i data are extracted from the inter-ELM periods in the discharge. In scenario B, T_i data were collected in an extended inter-ELM period. In figure 5.2 T_i measurements from the RFEA are shown as a radial profile of solid black circles for scenario A and solid red squares for scenario B with T_e measurements for comparison by LP as the corresponding hollow symbols. For measurements made in the region $\Delta R^{tgt}_{LCFS} < 8$ cm, T_i increases with P_{NBI}. In scenario A, T_i has a generally flat profile with $T_i \sim 10$ eV; however in scenario B, T_i increases with proximity to the LCFS at the target to a maximum value of $T_i \approx 18$ eV. T_e is similar at both heating powers with flat profiles of $T_e \sim 6$ eV, which is consistent with measurements on Tore Supra which show that additional heating has a more noticeable effect on T_i than T_e [49]. In scenario A, this results in $T_i/T_e \sim 2$, dropping slightly to $T_i/T_e \sim 1.4$ at $\Delta R^{tgt}_{LCFS} > 0.9$ m. In scenario B, $T_i/T_e = 1 \rightarrow 3$ increasing with proximity to the LCFS at the target.

T_i and T_e measurements as a radial profile for a similarly shaped double-null discharge with a lower plasma current, $I_P = 600$ kA, with beam heating, $P_{NBI} = 3.4$ MW, can be seen in figure 5.3 (scenario C). Scenario C has regular type I ELMs, therefore the RFEA data has been extracted from inter-ELM periods during the ELMy H-mode. T_i measurements generally increase as a function of proximity to the LCFS at the target with a relatively flat temperature in the far SOL and a steeper increase in the region $\Delta R^{tgt}_{LCFS} \leq 7$ cm. T_i is higher in the higher plasma current discharge (scenario B) in the region 5 cm $\leq \Delta R^{tgt}_{LCFS} \leq 7$ cm than in scenario C. In the region $\Delta R^{tgt}_{LCFS} \geq 7$ cm, scenario C has temperatures of $T_i \sim 11$ eV and $T_e \sim 7.5$ eV which are higher than both scenarios at higher power. This is likely related to the target density, because scenario C has a lower target density of $n_e^{tgt} \sim 1 \times 10^{18}$ m^{-3}, whereas scenarios A and B have higher target densities of $n_e^{tgt} \sim 2.5 \times 10^{18}$ m^{-3} which makes it more likely that ions and electrons at the target will cool through collisions. Since measurements of T_i are closer to the LCFS, this scenario has the highest measured inter-ELM H-mode ion temperature of $T_i \sim 20$ eV. T_e measurements are relatively flat across the profile with $T_e \sim 7.5$ eV, therefore $T_i/T_e = 1.5$ - 2.5.

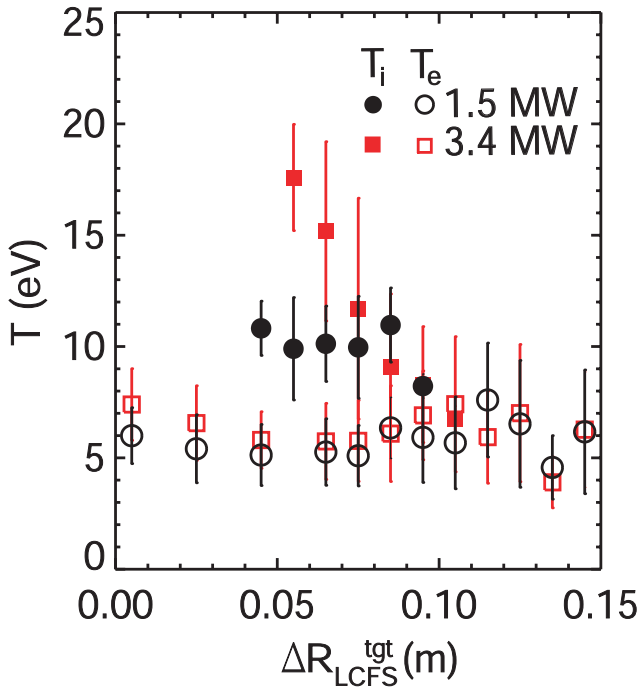

Figure 5.2: T_i measurements from the RFEA in scenario A (solid black circles) and in scenario B (solid red squares) and T_e from Langmuir probes in scenario A (hollow black circles) and in scenario B (hollow red squares), as a function of distance from the LCFS at the target.

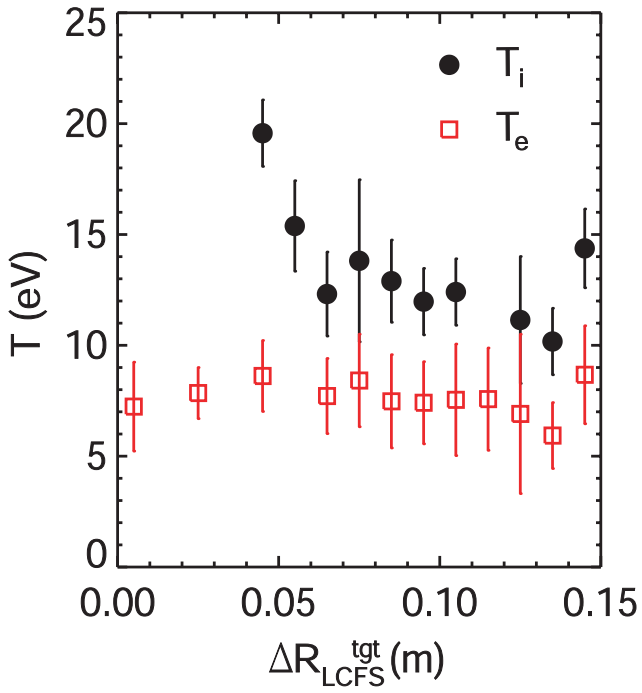

Figure 5.3: T_i measurements in scenario C from RFEA (solid black circles) and T_e from Langmuir probes (hollow red squares), as a function of distance from the LCFS at the target.

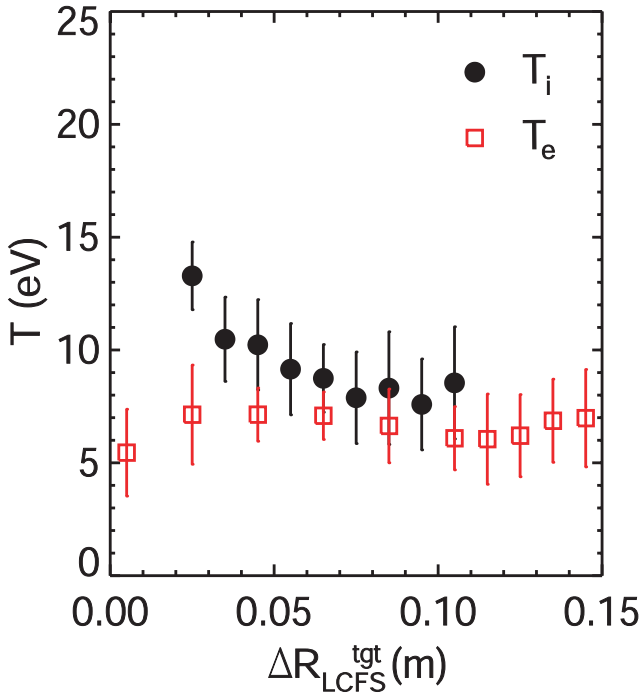

Figure 5.4: T_i measurements in scenario D from RFEA (solid black circles) and T_e from Langmuir probes (hollow red squares), as a function of distance from the LCFS at the target.

For the magnetic configuration comparison, a lower single null discharge with I_p = 600 kA, P_{NBI} = 3.4 MW and regular type I ELMs has been measured (scenario D). Figure 5.4 shows the temperature profile of T_i from RFEA and T_e from LP as a function of distance from the LCFS at the target. Ion temperatures are in the range $7 - 14$ eV over the range 2 - 11 cm from LCFS at the target where T_i increases with proximity to the LCFS at the target. The electron temperature is of a similar range to the previous inter-ELM H-mode discharges discussed, with T_e = $4 - 9$ eV, however the ion temperatures are the lowest in discharges with P_{NBI} = 3.4 MW and also lower than scenario A, at a lower beam power, over the same radial range. T_i values are low and do not peak until close to the LCFS at the target when compared to scenario C which is the equivalent CDN discharge, seen in figure 5.3. It is likely that the lower T_e in scenario D compared to scenario C is related to the increased target density in scenario D, where $n_e^{tgt} \approx 4 \times 10^{18}$ m^{-3}. The reduced target temperatures in scenario D compared to the inter-ELM H-mode CND scenarios could be related to a number of factors. It is likely the absorbed power in scenario D is lower than scenarios B and C, although the input power is the same, because the injected neutral beam will not pass through as wide a section of the plasma in the LSN due to the lower position of LSN discharges relative to DN discharges. The upstream temperature for the LSN discharge is also lower than scenario C which could be a result of the smaller amount of absorbed beam power. The longer connection length in the LSN discharge compared to the CDN discharge may also play a factor since there is a longer parallel distance over which ions can

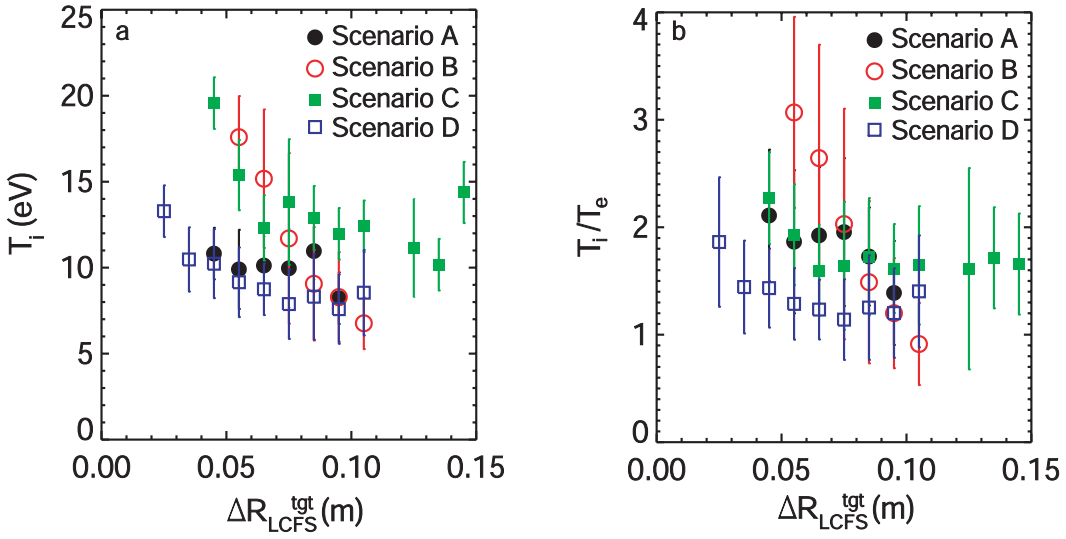

Figure 5.5: (a) Radial profiles at the target of T_i for all inter-ELM H-mode scenarios investigated; (b) T_i/T_e at the target in all inter-ELM H-mode scenarios as a radial profile.

thermally equilibrate with the electrons. In scenario D, $T_i/T_e \approx 1$ - 2; the lowest value of all the inter-ELM H-mode discharges, and therefore has the strongest ion and electron coupling of the inter-ELM H-mode discharges studied.

A summary of the measured T_i profiles from scenarios A - D and T_i/T_e as target profiles for these scenarios are shown in figure 5.5. It can be seen that scenarios B and C have the highest T_i measurements and also have the steepest profiles close to the LCFS at the target. Scenario D has a profile most similar to scenario A, possibly showing that the absorbed power in the LSN discharge is comparable to a single beam CDN plasma. T_i/T_e at the target in inter-ELM H-mode varies in the range $1 \rightarrow 3$ where scenario B, the discharge with the highest I_P and P_{NBI}, has the highest T_i/T_e ratio and scenario D, in LSN magnetic configuration, has the lowest T_i/T_e ratio measured in the region $\Delta R^{tgt}_{LCFS} > 0.10$ m.

5.2 Inter-ELM H-mode T_i/T_e interpretation

Since the LSN (scenario D) discharge has the lowest measured ratio of T_i/T_e and a difference between LSN and CDN magnetic configurations is the connection length, $L_\parallel$, in the SOL, this may be a factor affecting the thermal coupling of ions and electrons. This relation has been investigated by plotting T_i/T_e at a given radial position, $\Delta R^{tgt}_{LCFS} = 6.5$ cm, for each inter-ELM H-mode scenario against the connection length, $L_\parallel$, at the same radial position in the SOL, see figure 5.6. There is a clear trend of T_i/T_e at the target reducing with increased connection length. The reason for this may be because at longer $L_\parallel$ there is a greater time for ions and electrons to thermally equilibrate before reaching the target. This can be seen by the relation between $L_\parallel$ and the parallel transport time $\tau_\parallel \propto L_\parallel$. The thermal coupling

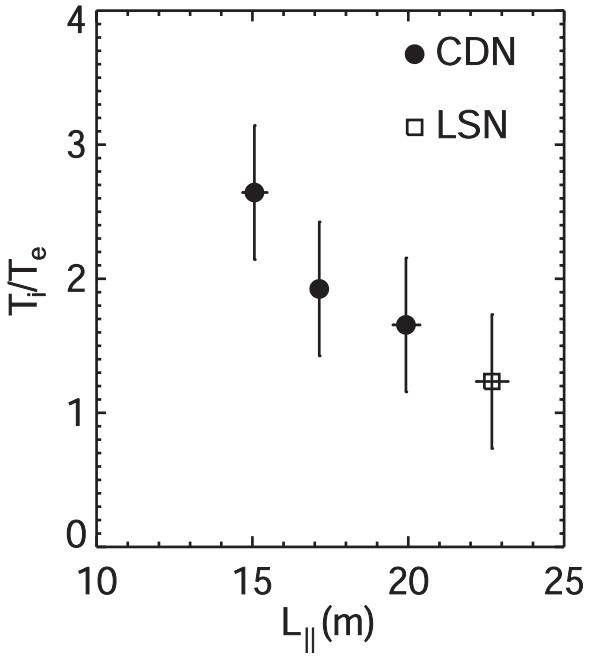

Figure 5.6: The ratio of T_i/T_e at $\Delta R^{tgt}_{LCFS} = 6.5$ cm plotted against the connection length, $L_{\|}$, for all inter-ELM H-mode discharges.

of electrons and ions at the target, R_{th}, calculated from upstream parameters, is also proportional to the SOL transit time, $R_{th} \propto \tau_{\|}$, and therefore $L_{\|}$, therefore at longer $L_{\|}$, R_{th} will be greater causing the ratio of T_i/T_e to tend to unity. As well as showing a decrease in T_i/T_e, figure 5.6 shows that at higher $L_{\|}$, T_i/T_e does tend to unity.

Since the thermal coupling, R_{th}, is proportional to $L_{\|}$, this should also scale with T_i/T_e in the inter-ELM H-mode scenarios studied. R_{th} as a function of upstream T_i/T_e can be investigated for each inter-ELM H-mode scenario since $R_{th} \propto L_{\|} n_e/(T_i + T_e)^{1/2} T_e^{3/2}$, see equations 4.1 and 4.2 in section 4.2 for the full equations. Since the upstream value of T_i has not been measured for all the inter-ELM H-mode scenarios studied here, R_{th} cannot be determined for each scenario as a single value. To account for the possible range of upstream T_i/T_e values, R_{th} is plotted as a function of upstream T_i/T_e in the range $0 \rightarrow 6$. This allows the values of $(T_i/T_e)^{up}$ which should give coupled electrons and ions at the target to be found for each scenario, see figure 5.7.

In the LSN scenario D (#28711), it can be seen that for values of upstream T_i/T_e up to six, ions and electrons at the target should be thermally coupled. We find $R_{th} \geq 1.5$ which are the highest values of R_{th} calculated for the range of $(T_i/T_e)^{up}$ investigated in the inter-ELM H-mode discharges here. This is consistent with T_i measured by RFEA at the target since scenario D had the lowest measured T_i/T_e at the target In the CDN scenario C (#27870) R_{th} values stay below unity even when upstream $T_i/T_e < 1$. This means, in contrast to the LSN discharge, we would expect the ions and electrons at the target never to be thermally coupled. This is

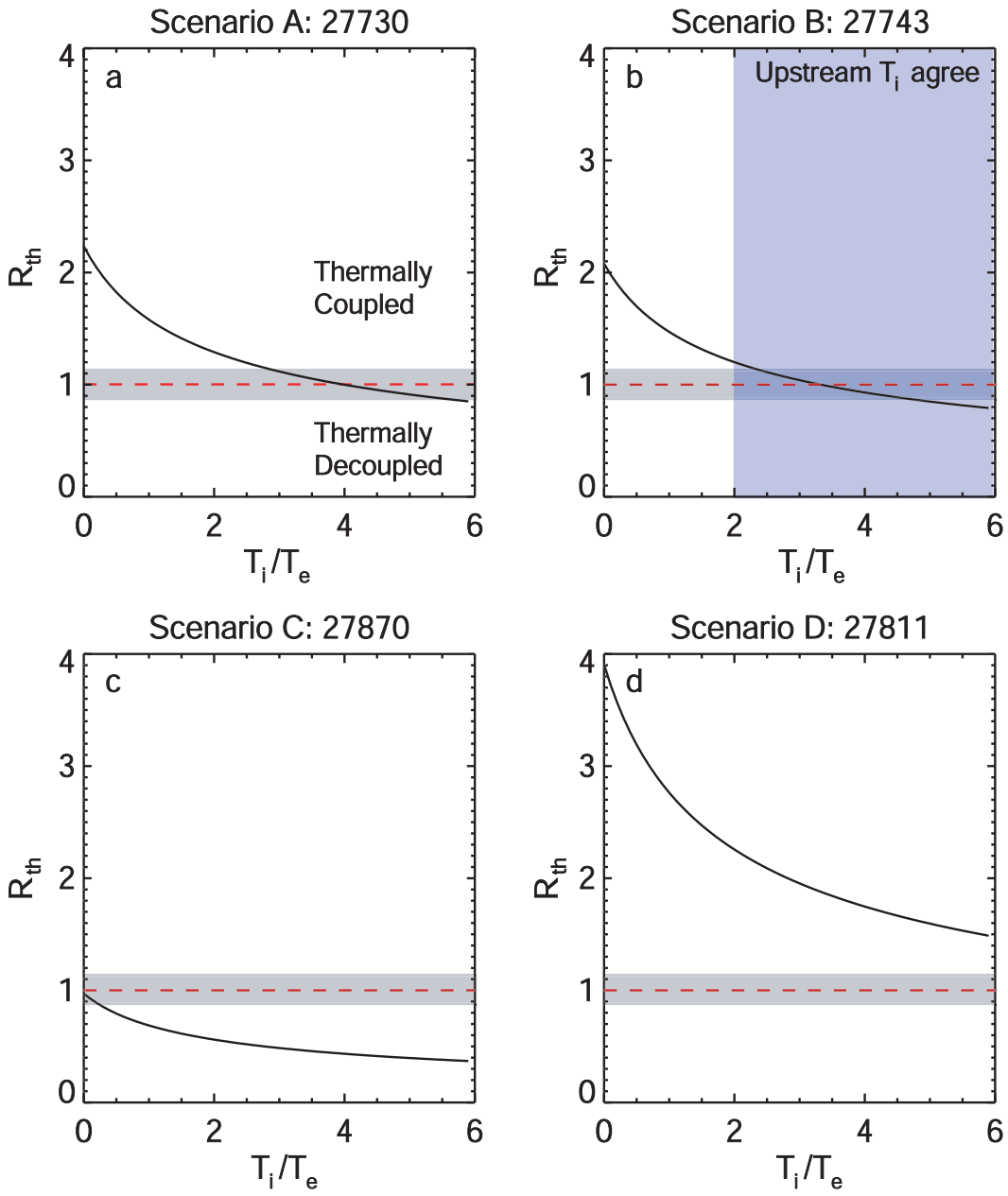

Figure 5.7: Thermal coupling of ions and electrons, R_{th}, as a function of upstream T_i/T_e for four inter-ELM H-mode discharges studied (a) Scenario A: CDN with I_P = 900 kA and P_{NBI} = 1.5 MW, (b) Scenario B: CDN with I_P = 900 kA and P_{NBI} = 3.4 MW, (c) Scenario C:CDN with I_P = 600 kA and P_{NBI} = 3.4 MW and (d) Scenario D: LSN with I_P = 600 kA and P_{NBI} = 3.4 MW. $R_{th} \geq 1$ implies coupled electrons and ions at the target.

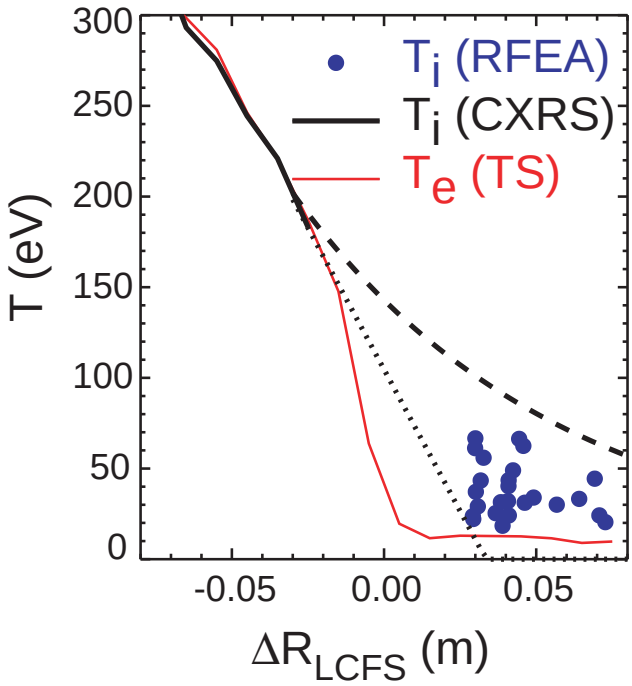

Figure 5.8: T_i measurements made using the midplane RFEA compared with T_e measurements made using Thomson scattering (TS) and T_i measurements made using charge exchange recombination spectroscopy (CXRS) as a function of radius during the inter-ELM period. The dotted and dashed lines are linear and exponential (fall off length 5 cm) fits to the CXRS T_i data [80].

consistent with the measured profile, see figure 5.3, where T_i remains higher than T_e even in the far SOL.

In scenarios A and B (#27730 and #27743) the coupling is dependant on T_i/T_e upstream with $R_{th} = 2.2$ showing thermally coupled ions and electrons and $R_{th} = 0.8$ showing uncoupled. At the same upstream T_i/T_e, scenario A should have more strongly coupled ions and electrons than scenario B and this is consistent with RFEA measurements of T_i which show higher T_i/T_e at the target for scenario B in the region $\Delta R^{tgt}_{LCFS} < 8$ cm, figure 5.2. The only inter-ELM H-mode scenario in which upstream measurements of T_i have been made by RFEA is scenario B, see figure 5.8 for midplane RFEA measurements by Allan et al [80]. These measurements show $(T_i/T_e)^{up} = 2 \rightarrow 6$. These measurements have been represented on figure 5.7(b) by the shaded area showing the values of R_{th} which corresponds to the measured upstream values for this plasma scenario. With these upstream measurements, ions and electrons at the target are likely to be thermally decoupled which is consistent with the measured target profile where a maximum $(T_i/T_e)^{tgt} = 3$ and $T_i > T_e$ is measured except in the far SOL, see figure 5.2. To further investigate the relationship between $(T_i/T_e)^{tgt}$ and thermal coupling, R_{th}, measurements of T_i^{up} would be valuable.

An effect which could help to explain the difference between T_i/T_e at the target in scenarios A and B is the ion Larmor radius. These two scenarios have different

temperature pedestals of $T_{e,ped} \approx 70$ eV and 170 eV for low and high beam powers respectively. Normally $T_i = T_e$ at the pedestal, therefore the ion Larmor radius can be estimated using $T_{e,ped}$ as $\rho_i \propto \sqrt{T_{e,ped}}$. This means scenario B will have a larger ion Larmor radius than scenario A where $\rho_i^A \approx 5.9$ mm and $\rho_i^B \approx 9.6$ mm. Although the size of the Larmor radius isn't large enough to extend the pedestal ions into the SOL; scenario B with larger ρ_i is more likely to have hot pedestal ions enter the SOL before as many cooling collisions can occur compared to the lower beam power discharge. This may help to explain why the value of T_i/T_e at the target is highest in the region closest to the LCFS at the target. Scenario B has the highest measured T_i/T_e at the target and also has the largest Larmor radius of ρ_i = 9.6 mm compared to all the inter-ELM H-mode scenarios.

5.3 Target heat flux dependence on T_i/T_e

The heat flux at the target, and therefore the power arriving at the divertor, P_{DIV}, can be calculated using target LP, however it requires an assumption for the value of T_i/T_e at the target which has not been measured in MAST until now. On MAST there are Langmuir probes at all four strike points which can be used to calculate the power to the divertor using $q = \gamma j_{sat} T_e$, where the sheath heat transmission coefficient, as defined in chapter 2, is $\gamma = 5 + 2T_i/T_e$ [24, 53], and j_{sat} is the ion saturation current density. To obtain P_{DIV}, j_{sat} is integrated over the power deposition area at the target. The total power arriving at the divertor targets should equal the power which enters the SOL, calculated from $P_{SOL} = P_{in} - \dot{W} - P_{rad}$, where P_{in} is the sum of the ohmic power and absorbed neutral beam power, $\dot{W}$ is the rate of change of the stored plasma energy and P_{rad} is the radiated power measured by bolometry [26]. Balance of the power into and leaving the SOL is found in L-mode plasmas in MAST using the assumption that $T_i = T_e$ at the target, see figure 5.9 [81].

Using the measured value for T_i at the target, the heat flux to the target, q, has been calculated using LP data and compared to the heat flux measured by the IR camera. The heat flux calculated from LP data assuming $T_i/T_e = 1$ is also compared to see if T_i measured by RFEA gives a better match to IR data than the assumption $T_i = T_e$. This comparison has been made for the lowest density double-null ohmic L-mode discharge with $I_P = 400$ kA, (see figure 4.2 in chapter 4 for the T_i and T_e profiles). Figure 5.10 compares the heat flux arriving at the target as a radial profile for the three diagnostic methods. LP data is shown by black circles which assumes $T_i = T_e$, data from the IR camera is shown by red hollow circles, and measurements by LP using T_i values measured by the target RFEA are shown by hollow blue squares (labelled as RFEA). Within the scatter across the profile all three methods agree relatively well. This is expected in L-mode since power balance can be found on MAST when $T_i = T_e$ is assumed [81] and T_i measurements shown

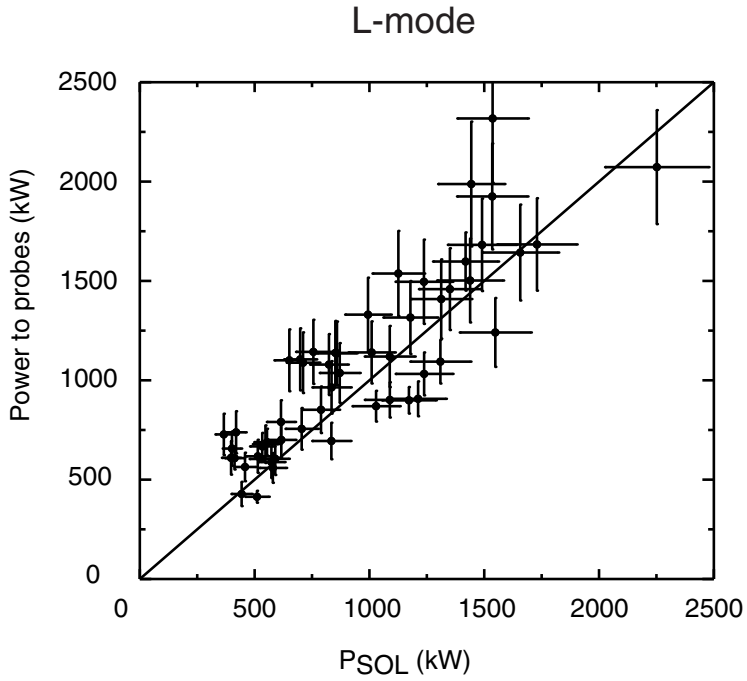

Figure 5.9: Total power arriving at the target probes versus the power into the SOL (P_{SOL}) for L-mode shots on MAST [81].

in chapter 4 confirm that $T_i/T_e \sim 1$ is a fair assumption for the ohmic $I_P = 400$ kA discharges.

On MAST in inter-ELM H-mode plasmas power balance cannot be found when $T_i = T_e$ at the target is assumed. Figure 5.11 shows the power entering the SOL, P_{SOL}, vs the power arriving at the Langmuir probes, for a number of inter-ELM H-mode discharges. If $T_i = T_e$ is assumed when calculating the power at probes from P_{DIV} then the total power arriving at the divertor is less than the power entering the SOL, as shown by the black circles. However, power balance could be achieved in inter-ELM H-mode if $T_i/T_e = 2 \rightarrow 4$ was used to calculate the power at probes as can be seen in figure 5.11 by the red squares and blue triangles which fall either side of power balance.

Figure 5.12 shows, for the inter-ELM period in scenario B, the heat flux to the lower outer divertor target from IR camera data (red hollow circles) and the heat flux calculated from Langmuir probes, assuming $T_i = T_e$ (black circles). Since the Langmuir probe heat flux does not match the IR data at the strike point when $T_i = T_e$ is assumed, it is likely $T_i/T_e > 1$ for the region around the strike point of the radial profile. In order to compare the heat flux calculated using T_i data measured by RFEA, a fit to the data in the region $4 - 10$ cm from the LCFS at the target has been used to produce a heat flux in the divertor SOL; this is also shown in figure 5.12 (hollow blue squares). Near the strike point, the LP calculation gives an underestimate of q, but the RFEA data within the error bars is consistent with the IR data. Therefore $T_i/T_e > 1$ would give an improved match to the IR data in the strike point region. In the region $\Delta R^{tgt}_{LCFS} = 4$ - 9 cm the LP data are greater

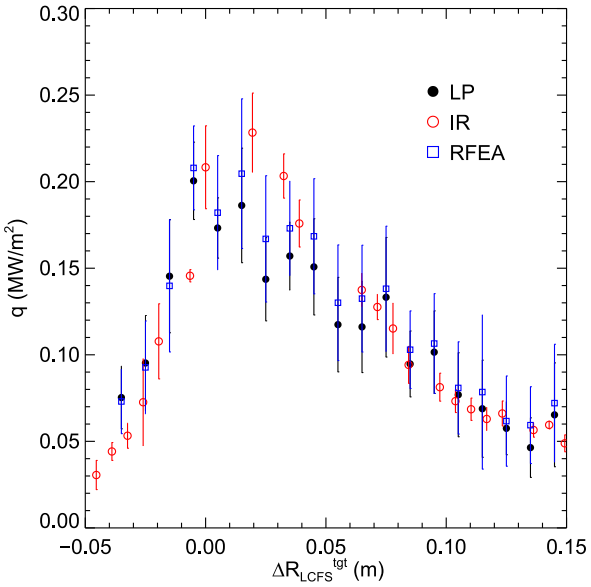

Figure 5.10: Heat flux profile at the target for an ohmic L-mode discharge with I_P = 400 kA at low density (26798) measured by infra-red camera (hollow red circles) and Langmuir probe measurements (solid black circles) assuming $T_i = T_e$. Also shown is the heat flux calculated from Langmuir probe measurements when using T_i measured by RFEA at the target with LP measurements (hollow blue squares).

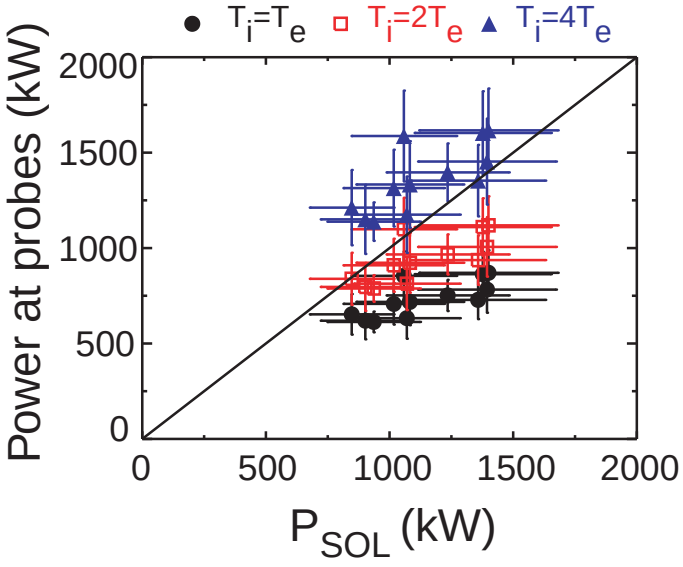

Figure 5.11: Inter-ELM H-mode energy balance showing the power into the SOL, P_{SOL}, for a number of discharges compared to the power arriving to the target Langmuir probes, power at probes, at all four strike points in MAST. The data is shown when assuming $T_i = T_e$ (black circles), $T_i = 2T_e$ (red squares) and $T_i = 4T_e$ (blue triangles) when calculating the power at probes.

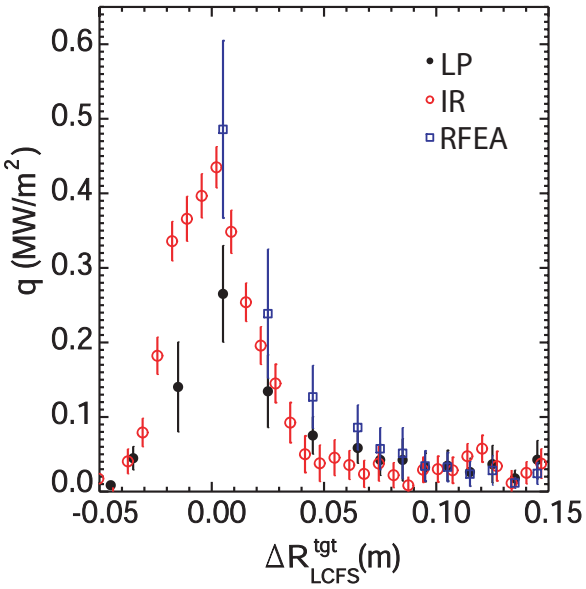

Figure 5.12: Heat flux profile at the target for inter-ELM H-mode scenario B ($I_P = 900$ kA, $P_{NBI} = 3.4$ MW) measured by infra-red camera (hollow red circles) and Langmuir probe measurements (solid black circles) assuming $T_i = T_e$. Also shown is the heat flux calculated from Langmuir probe measurements when using a fit to the measured RFEA data for T_i in the SOL with LP measurements (hollow blue squares).

than the IR data even when $T_i = T_e$ is assumed, therefore the increase in q when using the measured T_i/T_e by the RFEA will not give a better match, however this region contributes only a small amount of the total power to the target. When calculating the total power to the target the difference between IR and LP data at the strike point has a greater effect then the overestimate of the RFEA and LP data further into the SOL where q is lower. Therefore, in inter-ELM H-mode $T_i/T_e \sim 3$ would allow better power balance when calculating the power at the divertor from Langmuir probes.

5.4 T_i measurements in ELMs at the divertor

5.4.1 T_i during average type III ELMs at the divertor

As described in section 3.3.2, the temperature during an average ELM arriving at the target can be determined from a number of similar ELMs measured at the divertor RFEA provided they are measured at the same radial location. Measurements have been made of similar type III ELMs in a double-null ELMy H-mode discharge with $I_P = 600$ kA and $P_{NBI} = 1.8$ MW. The discharge has been designed to hold the plasma strike point at a set distance from the target RFEA, ΔR^{tgt}_{LCFS}, for the ELMy H-mode period allowing ELMs to be measured by the RFEA for a fixed position. The same discharge has been repeated with the strike point fixed at a different radial location to allow measurements of the average ELM T_i at the target for two ΔR^{tgt}_{LCFS} positions.

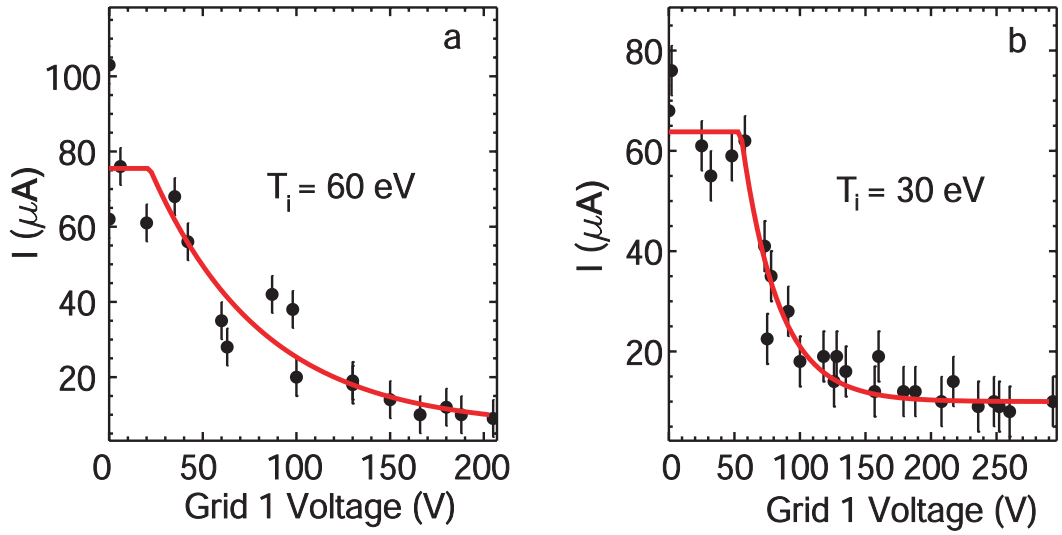

Figure 5.13: Composite I-V characteristic for type III ELMs at a) $\Delta R^{tgt}_{LCFS} = 5 - 7$ cm and b) $\Delta R^{tgt}_{LCFS} = 8$ - 9 cm.

Two I-V characteristics have been constructed by the slow voltage sweep method for each position of $\Delta R^{tgt}_{LCFS} = 5 - 7$ cm and $\Delta R^{tgt}_{LCFS} = 8 - 9$ cm. The I-V characteristic for ELMs measured at each position are shown in figure 5.13. It can be seen that the temperature of the average ELM at the target is $T_i^{ELM} \sim 60$ eV, much higher than inter-ELM, measured in the range $5 - 7$ cm from LCFS at the target. Further from the LCFS at the target ($\Delta R^{tgt}_{LCFS} = 8 - 9$ cm), the temperature of the average ELM is reduced to $T_i^{ELM} \sim 30$ eV. This result shows the expected reduction or 'fall-off' of the ion temperature of an average ELM with distance from the LCFS at the target; as seen in ASDEX Upgrade [43].

The temperatures measured by this method for an average ELM arriving at the divertor target should give an upper bound on the ion temperature in ELMs at the divertor. This is because the method used here constructs an I-V characteristic using the maximum current arriving at the RFEA from to the ELM and therefore this gives the peak T_i of ions released from the ELM. A further reason that this method may overestimate T_i in ELMs is because it is assumed for RFEA analysis that the velocity distribution is constant. Although similar ELMs are used, an ELM releasing more particles will cause a higher current to be measured at the RFEA collector plate for a given grid 1 voltage than the current due to an ELM releasing less particles of the same temperature. This would cause a higher temperature to be determined from the I-V characteristic for the average ELM. Despite the limitations of the average ELM ion temperature measurement technique it gives a simple comparison to the fast swept ELM measurements (see section 3.3.3 and section 5.4.2 for results) to check for consistency in the absence of any other diagnostic measurements.

Unfortunately due to the lower frequency of type I ELMs sufficient statistics could not be measured to give an average type I ELM ion temperature. Both type I and type III ELMs have been investigated by the fast swept grid 1 voltage method

which is studied in the following section.

5.4.2 Fast swept T_i measurements in ELMs at the divertor

The fast sweeping technique has been used to measure both type I and type III ELMs. The type III ELMs have been measured in the same discharge used for the average type III ELM T_i measurements in the previous section. The neutral beam heating power has been increased to $P_{NBI} = 3.4$ MW in the discharge used to measure type I ELMs. Unfortunately due to the high currents at the RFEA slit plate during ELMs, the slit plate power supply failed during many of the ELMs. Since insufficient voltage on the slit plate may lead to space charge limiting, see section 3.2.2, there are a limited number of both type I and type III ELM which can be analysed. Some of the ELMs analysed only have measurements of a few I-V characteristics which were not space charged limited and therefore usable in the fast swept ELM analysis.

Type I ELMs have been measured at a location of $\Delta R^{tgt}_{LCFS} = 8$ cm and type III ELMs have been measured at a location of $\Delta R^{tgt}_{LCFS} = 5$ cm. To allow a number of ELMs to be compared on the same time base the ELM time, t_{ELM}, is defined as the start of the ELM, determined from the time at which the midplane D_α signal increases from the inter-ELM level by 10% of the peak value at the ELM as used in [82], see figure 5.14(a). All measurements are plotted relative to t_{ELM}. Figure 5.14 shows the D_α signal at the midplane and the divertor along with the RFEA slit plate current, I_{SP}, as a function of t-t_{ELM}.

The I-V characteristics for an example of a type I and type III ELM are shown in figures 5.15 and 5.16 respectively. The current signal on the slit plate during the ELM is shown along with the individual I-V characteristics which were analysed during the ELM. On the slit plate current trace the red lines indicate the average time of the I-V characteristics and the blue lines show the extent of the voltage sweep of grid 1 in time. For the type III ELMs the slit plate current shows the I-V characteristic fits do not continue through the ELM after t-$t_{ELM} = 250$ μs because the RFEA may become space charge limited.

The slit plate current, I_{SP}, peaks at t-$t_{ELM} \approx 150$ μs which is consistent with the ion parallel transport time, $\tau_{i,\parallel} = L_\parallel/c_s$. The initial fits show a high sheath voltage with a maximum of $V_s \sim 60$ V occurring at t-$t_{ELM} = 0$ μs which is consistent with hot electrons arriving at the target almost instantaneously at t_{ELM}, on the electron parallel transport time, $\tau_{e,\parallel} = L_\parallel/v_{Te}$, and coincides with a peak in the electron temperature at the target. The sheath voltage generally decreases through the ELM duration from this initial peaking. The ion temperature peaks later than the sheath voltage to a maximum of $T_i \sim 30$ eV occurring at the same point as the peak in current at the slit plate at t-$t_{ELM} \sim 150$ μs, 150 μs after V_s peaks which is consistent with parallel transport of ions and electrons.

The type III ELM shows similar features to the type I, however slightly later

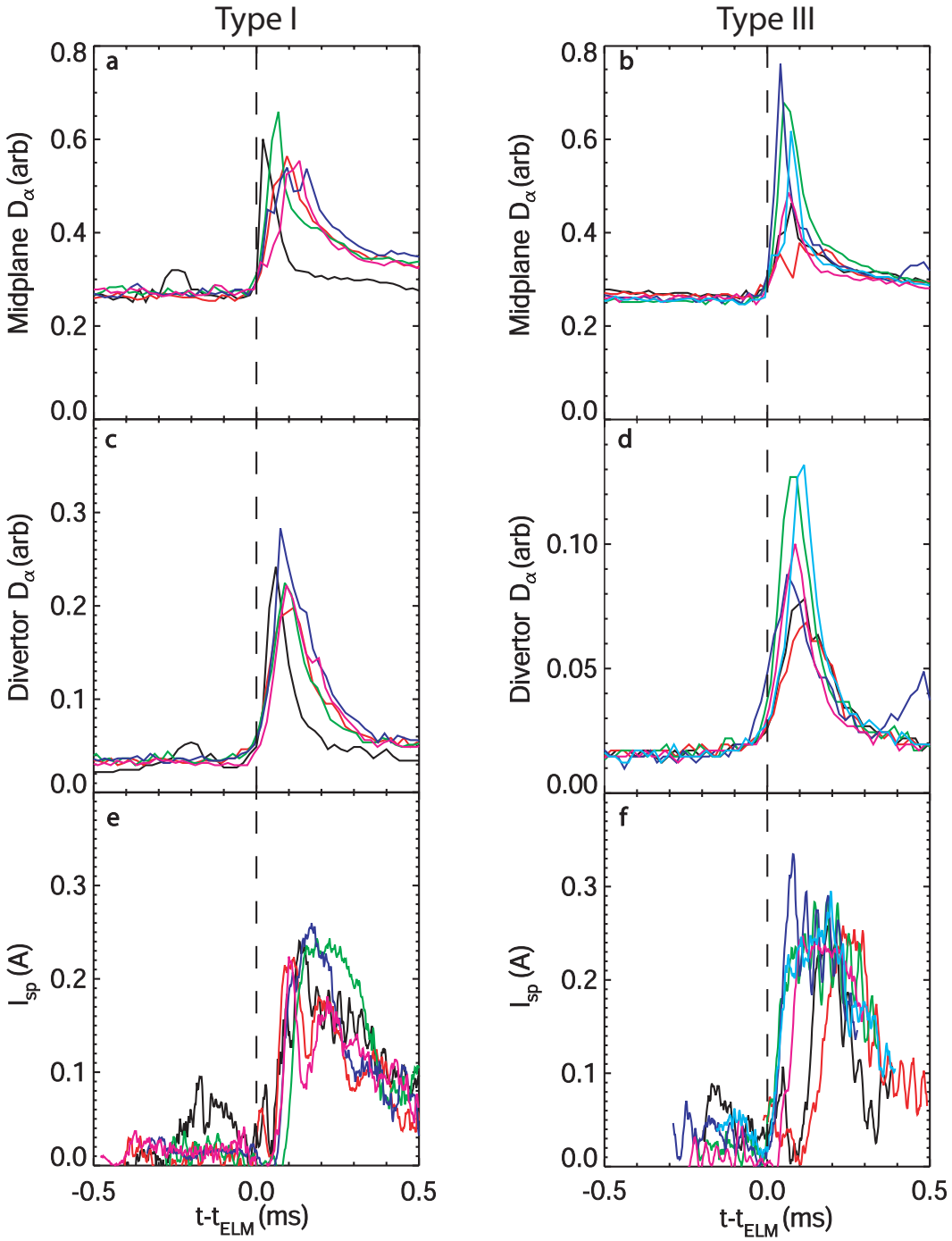

Figure 5.14: D_α traces for each analysed ELM at the midplane for type I (a) and type III (b) ELMs, and D_α traces at the divertor for type I (c) and type III (d) ELMs. Also shown is the slit plate current of the RFEA for type I (e) and type III (f) ELMs.

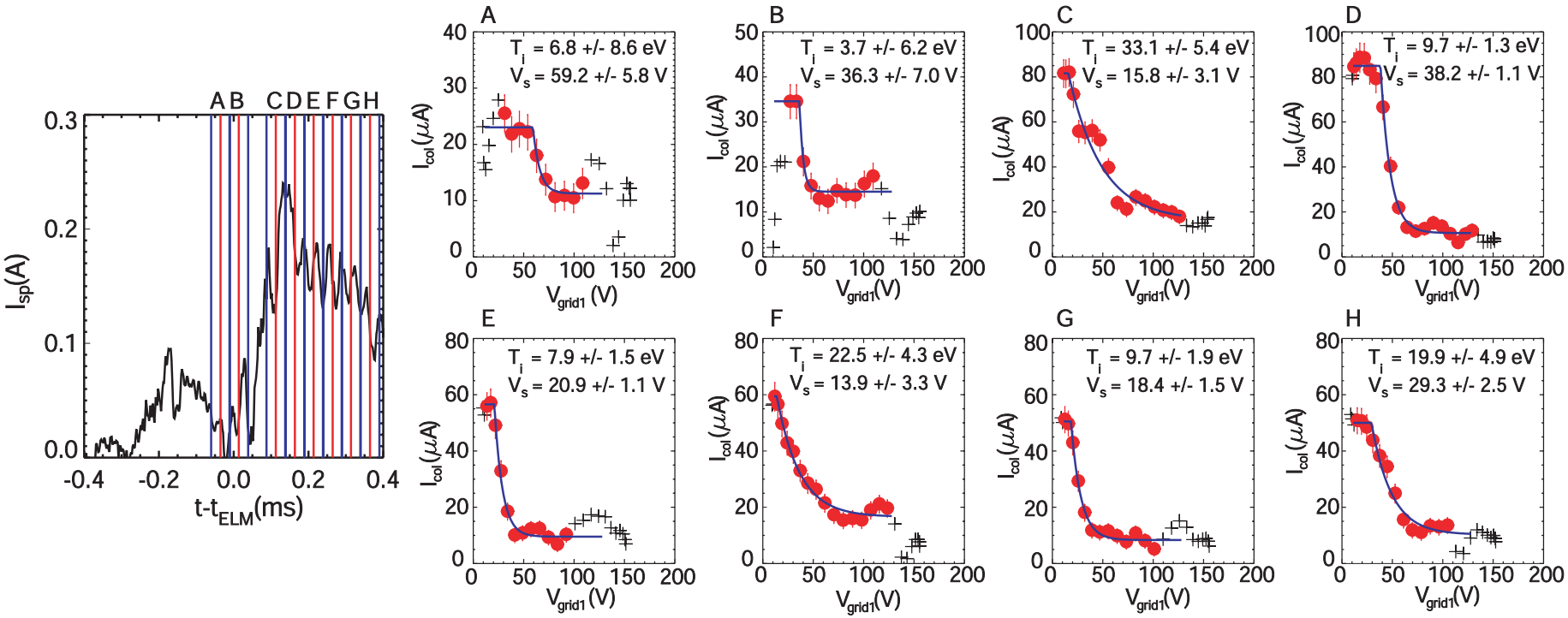

Figure 5.15: Fitted I-V characteristics during the ELM rise and peak for a type I ELM arriving at the target RFEA at $t_{ELM} \sim 0.203$ s. The red lines on the slit plate current indicate the average time of each I-V characteristics and the blue lines either side indicate the extent of the voltage sweep in time. For each fitted characteristic the red points are the chosen points which are fitted and the blue curve is the fit to this data.

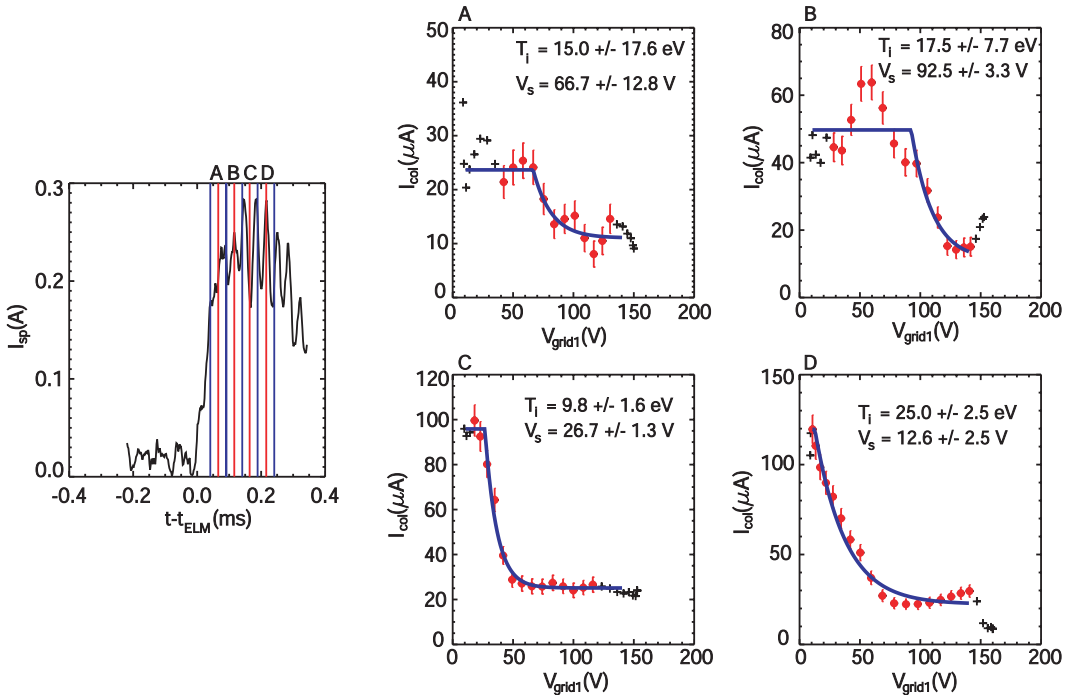

Figure 5.16: Fitted I-V characteristics during the ELM rise and peak for a type III ELM arriving at the target RFEA at $t_{ELM} \sim 0.22$ s. The red lines on the slit plate current indicate the average time of each I-V characteristics and the blue lines either side indicate the extent of the voltage sweep in time. For each fitted characteristic the red points are the chosen points which are fitted and the blue curve is the fit to this data.

in time relative to the start of the ELM, t_{ELM}. The sheath voltage can be seen to peak to a maximum of $V_s \sim 90$ V at t-$t_{ELM} = 100$ μs. The sheath voltage has reduced to a value more likely consistent with inter-ELM values 100 μs later. Ignoring the third characteristic, the ion temperature appears to be increasing with a peak later in time than the peak in V_s, similarly to the type I ELM. The increase of the sheath voltage closer in time to the current peak of the ELM for the type III ELM compared to the type I ELM may be due to the difference in relative position to the strike point that RFEA measurements have been made.

To further investigate the trends in the RFEA fitted parameters, T_i, V_s and I_0, the maximum ion current at the collector; these parameters have been plotted as a function of time relative to t_{ELM} for several type I and type III ELMs. These ELMs have been analysed in the same manner as the two ELMs shown in figures 5.15 and 5.16. The ELMs studied have been aligned in time as a function of t-t_{ELM} and are all shown in figure 5.14(a,c,e) for type I and 5.14(b,d,f) for type III ELMs. After the peak in the slit plate current, shown in figure 5.14(e) and 5.14(f), the type III ELMs behave very differently from one another which is partly due to the slit plate voltage failure after the peak of the ELM which affects the current measured by the power supply. All the RFEA measurements used for type III ELMs are taken only in the rise and peak of the ELM due to potential space charge limiting affecting T_i

measurements later in the ELM.

T_i, V_s and I_0 as a function of time relative to t_{ELM} are shown in figures 5.17 and 5.18 for type I and type III ELMs respectively. The type I ELM measurements show a broad peak in T_i with a maximum of $T_i \sim 40$ eV occurring at t-$t_{ELM} \sim 100$ μs. Although there is a scatter in the V_s measurements, there is a general trend of decreasing sheath voltage through the duration of the ELM. The measured peak value is $V_s \sim 80$ V at t-$t_{ELM} = 100$ μs however the general decrease in V_s is consistent with the peak in T_e at the target which occurs earlier at t-$t_{ELM} = 0$. I_0 has a broad peak around t-$t_{ELM} \sim 150$ μs. This measurement is related to the ion density arriving at the collector of the RFEA and shows that the ion density peaks < 50 μs after the peak in T_i.

Measurements in type III ELMs (figure 5.18) show similar trends to those seen for type I ELMs, however the parameters evolve over shorter timescales. The ion temperature, although scattered, shows a peak of $T_i \sim 35$ eV occurring at t-$t_{ELM} \sim 80$ μs. The sheath voltage shows a similar trend to type I ELMs although there is less scatter in V_s over time. The trend of decreasing sheath voltage with time shows a peak at a similar time to T_i, at t-$t_{ELM} \sim 80$ μs, however since no earlier measurements are made, V_s may be higher at $t < t_{ELM}$ which is consistent with peak T_e measurements by LP (shown in figure 5.20 and explained in the following paragraphs). I_0, which indicates the density of ions in the ELM at the collector plate, peaks around t-$t_{ELM} \sim 150$ μs. This time also coincides with the reduction of the sheath voltage which is expected since the sheath voltage is only enhanced while more electrons than ions released by the ELM have arrived at the target.

Type III ELMs measured by the fast swept method at $\Delta R^{tgt}_{LCFS} \approx 5$ cm are similar to the type III ELMs measured by the average ELM temperature measurement method made in the region $\Delta R^{tgt}_{LCFS} \approx 5$ - 7 cm; see figure 5.13. The average ELM measurement of T_i from the peak of the ELM ion currents shows a higher $T_i^{ELM} \approx 60$ eV, than most of the measurements obtained by the fast swept method. This is likely because, as mentioned in section 5.4.1, the average ELM measurement determines the temperature from the maximum ion current during each ELM and may be an overestimate of T_i due to fitting of the I-V characteristic. The measurements by the fast swept method are lower than those made by the slow swept method of the average ELM temperature which shows that the methods are consistent. This comparison allows the only confirmation that T_i measurements during ELMs arriving at the MAST divertor target are reasonable.

Measurements of j_{sat} and T_e during type I and type III ELMs made by LP at the same position as the RFEA are shown in figure 5.19 and 5.20 respectively. These measurements have been extracted by taking LP measurements at the RFEA position close to t_{ELM} in the same discharge. These measurements are converted to a function of t-t_{ELM} using the same definition of t_{ELM} as previously used [82]. The peak T_e for type I ELMs occurs at $t \sim t_{ELM}$ with $T_e^{max} \sim 20$ eV, see figure

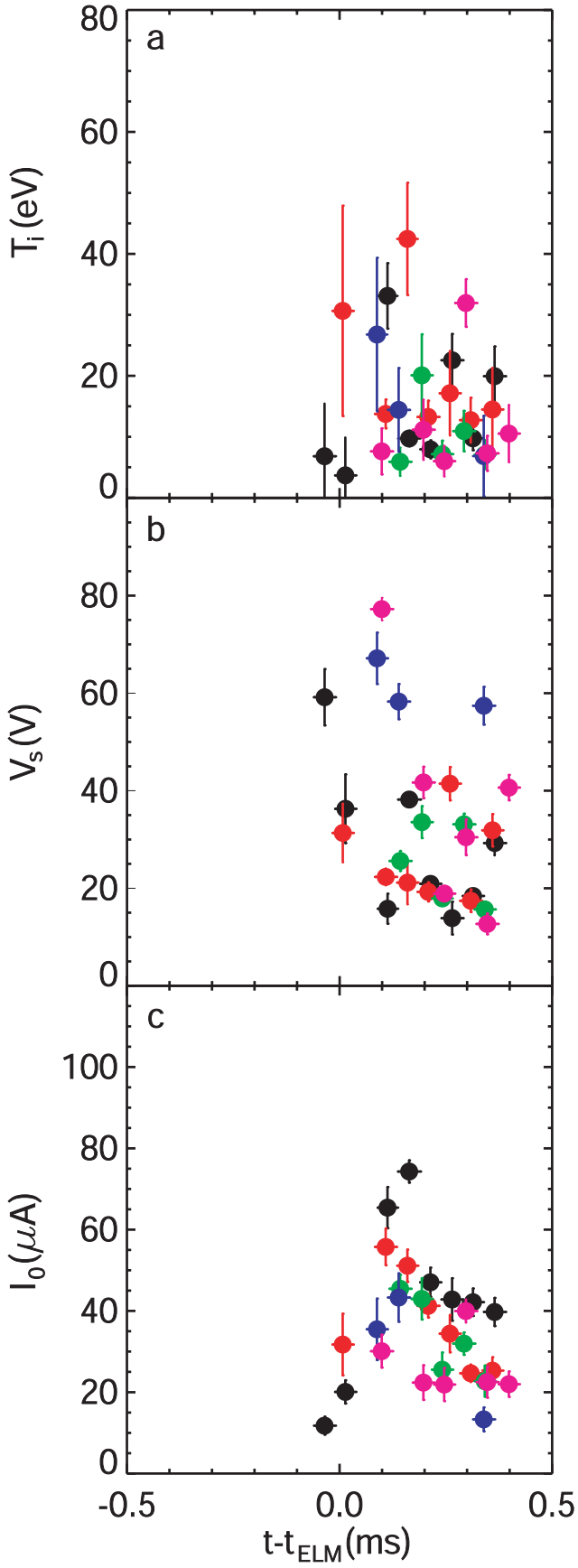

Figure 5.17: Measurements through the duration of a number of type I ELMs of a) ion temperature, T_i, b) sheath voltage, V_s, and c) maximum ion current, I_0.

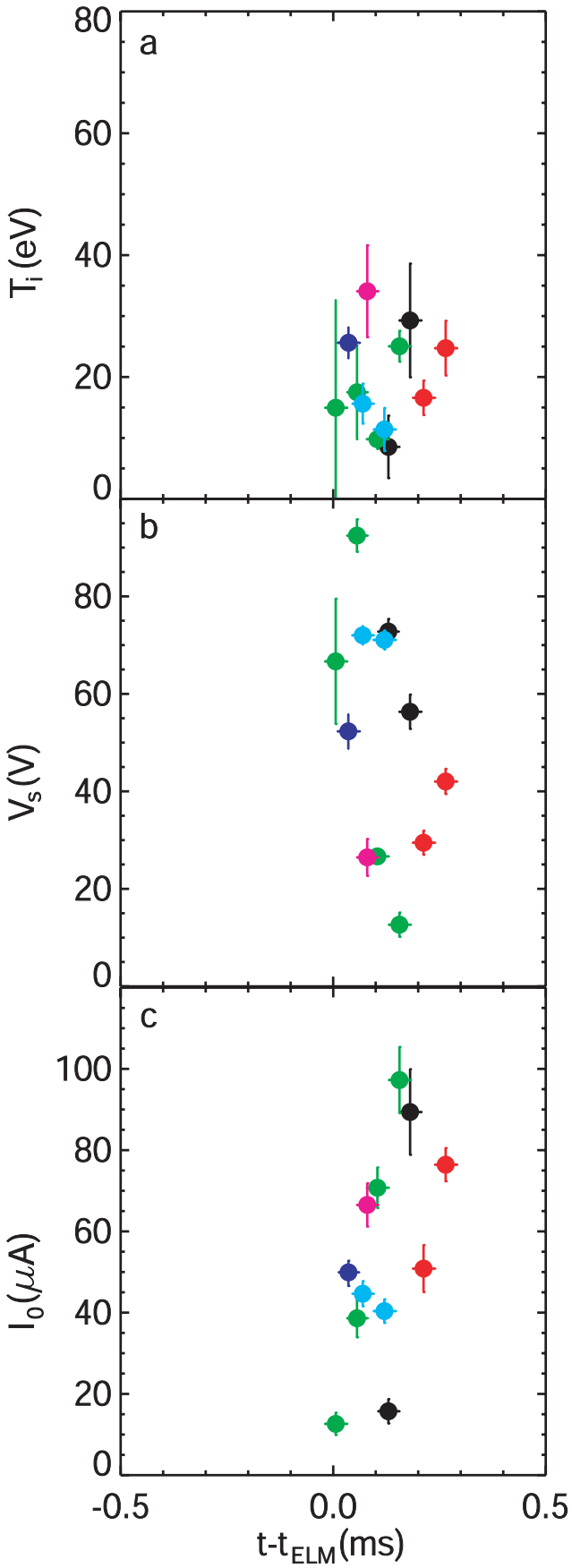

Figure 5.18: Measurements through the duration of a number of type III ELMs of a) ion temperature, T_i, b) sheath voltage, V_s, and c) maximum ion current, I_0.

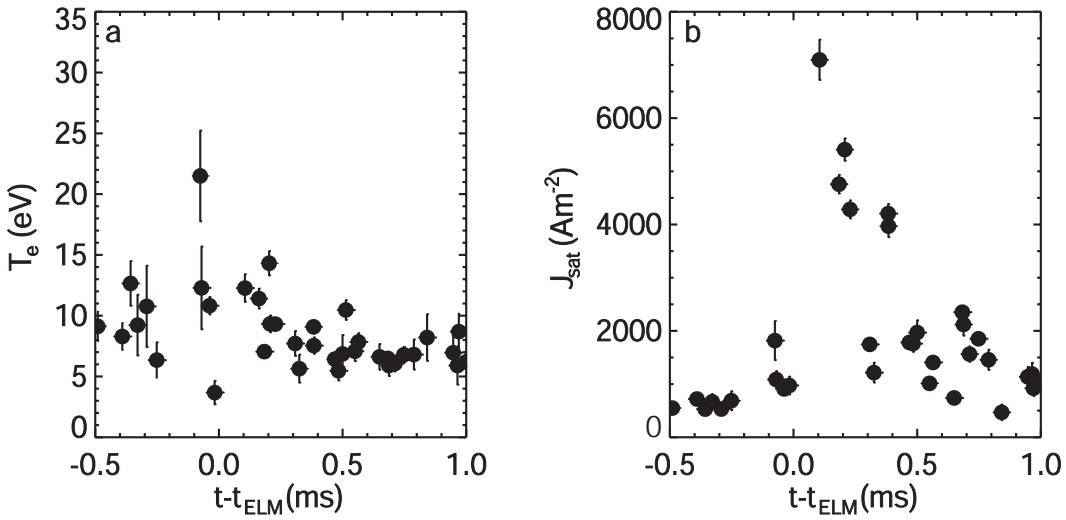

Figure 5.19: Langmuir probe measurements in time relative to a number of type I ELMs arriving at the same radial position as the target RFEA of a) the electron temperature, T_e, and b) the ion saturation current density, j_{sat}.

5.19. The inter-ELM T_e value measured furthest from the peak T_e is $\sim$ 7 eV which is consistent with inter-ELM measurements shown in figure 5.3 for a similar plasma discharge. The peak T_e during type III ELMs is $T_e \sim 25$ eV and occurs at t $\sim$ t_{ELM} as well, see figure 5.20. Both type I and type III ELMs have narrower peaking of the electron temperature during the ELM than the equivalent T_i measurements. This may be due to the difference in parallel transport times since $\tau_{e,\|} < \tau_{i,\|}$, which allows the hot electrons to arrive instantaneously whilst the remaining electrons are cooled whilst travelling to the target on the ion timescale. For LP analysis the inter-ELM measurements are not removed therefore, as mentioned previously, far from the T_e peak due to the ELM T_e measurements are inter-ELM values. The peak in T_e measured by LP is consistent with V_s measurements decreasing after t = t_{ELM} which is the earliest measurements made by the RFEA, therefore the peak in T_e is compatible with V_s measurements. For both type I and type III ELMs, an apparent peak in j_{sat} occurs in the range t-$t_{ELM} \sim$ 100 - 200 μs which is consistent with measurements of I_{SP} and I_0.

A comparison of T_i and T_e during the ELM cycle is shown in figures 5.21 and 5.22 for type I and III ELMs respectively. The peak in electron temperature occurs earlier than the peak in ion temperature by $\sim$ 150 μs for type I ELMs. T_e for type III ELMs shows a peak occurring $\sim$ 100 μs earlier than the peak in T_i. The peak in T_i is higher than T_e for both type I and type III ELMs, however the difference between the maximum T_i and T_e is lower in type III ELMs. During the ELM the ratio of T_i/T_e varies with time. At the beginning of the ELM, i.e when hot electrons arrive at the target, $T_i/T_e < 1$, since $T_e^{peak} \sim 20$ eV for type I ELMs occurs during a period of inter-ELM T_i at the target where $T_i \sim 12$ eV, giving $T_i/T_e \sim 0.6$. Later in time when T_i is measured by the RFEA, $T_i/T_e \sim$ 1 - 4 for type I ELMs and $T_i/T_e \sim$ 1 - 3 for type III ELMs.

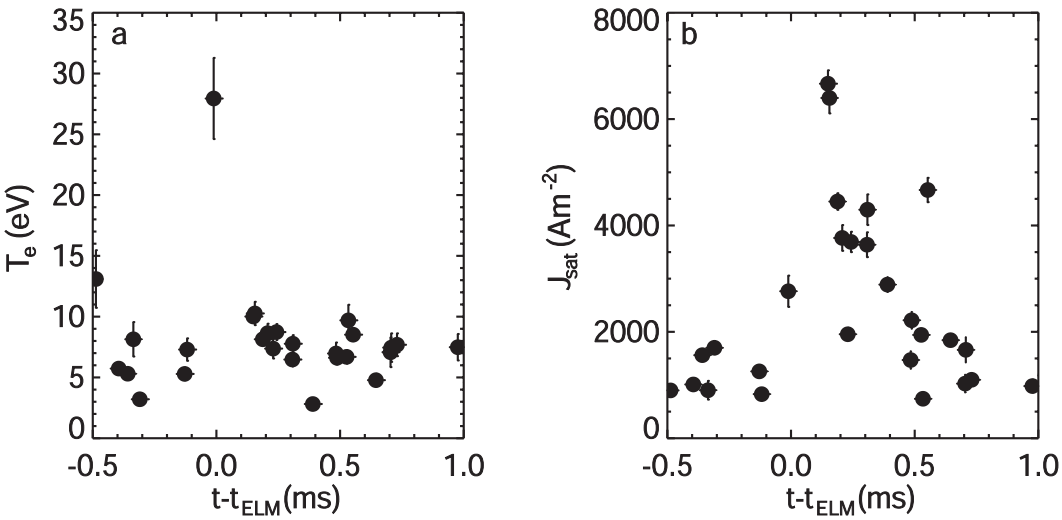

Figure 5.20: Langmuir probe measurements in time relative to a number of type III ELMs arriving at the same radial position as the target RFEA of a) the electron temperature, T_e, and b) the ion saturation current density, j_{sat}.

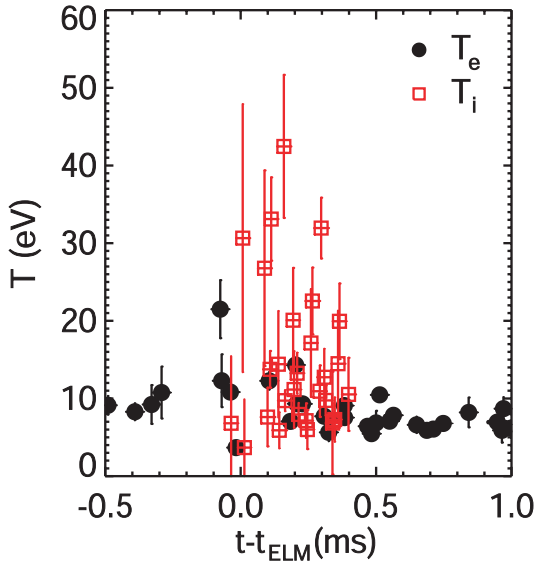

Figure 5.21: Comparison of the electron temperature, T_e (black circles), measured by LP and the ion temperature, T_i (red squares), measured by RFEA in time relative to t_{ELM} for type I ELMs.

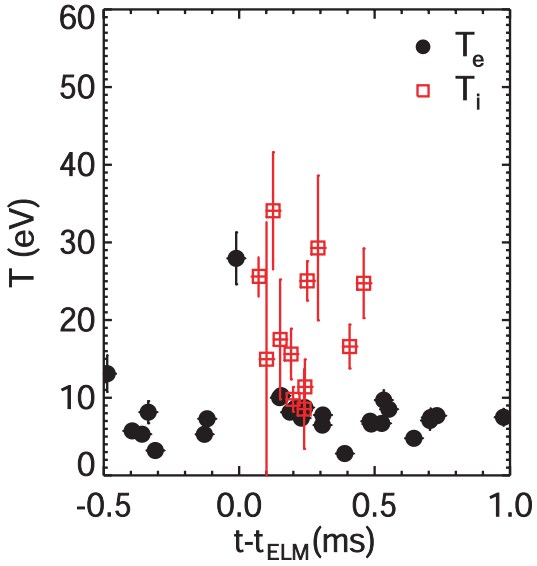

Figure 5.22: Comparison of the electron temperature, T_e (black circles), measured by LP and the ion temperature, T_i (red squares), measured by RFEA in time relative to t_{ELM} for type III ELMs.

For type I ELMs the T_e data has been fitted and also a high and low fit to the T_i data has been made through the ELM, see figure 5.23(a). Using these fits the ratio of T_i/T_e in time during the ELM at the target can be plotted for the high and low T_i fits, see figure 5.23(b). It can be seen that for type I there is a peak of $T_i/T_e = 2$ - 4.8, the equivalent peak for type III ELMs is $T_i/T_e \approx 3.5$. This variation of T_i/T_e through the ELM duration has implications for the sheath heat transmission factor, γ, which is used to calculate the power to the divertor during ELMs [24]. In type I ELMs, to see how γ changes through the ELM arriving at the target, equation 2.11 shown in chapter 2 has been used to calculate γ for both fitted T_i functions, shown in figure 5.23(c). Due to T_i/T_e varying through the ELM γ can rise by a factor of 1.3 - 2.3 giving a possible peak of $\gamma = 18$ because $T_i > T_e$.

5.4.3 Comparison with models and experimental measurements of ELMs

Simple ELM loss evolution

An ELM event leads to the ejection of an equal number of ions and electrons into the upstream SOL. Due to the high mobility of hot electrons in the ELM, these electrons travel by parallel transport to the divertor targets almost instantaneously as the plasma enters the SOL which produces a parallel electric field along the SOL. This retards further electrons and forces the rest of the ions and electrons released by the ELM to travel to the target on the ion timescale. The ions will be marginally accelerated due to the electric field caused by the hot fast electrons. The hot electrons arriving at the target produce a peak in the electron temperature and modify the sheath, enhancing the negative sheath potential, V_s. The bulk of the

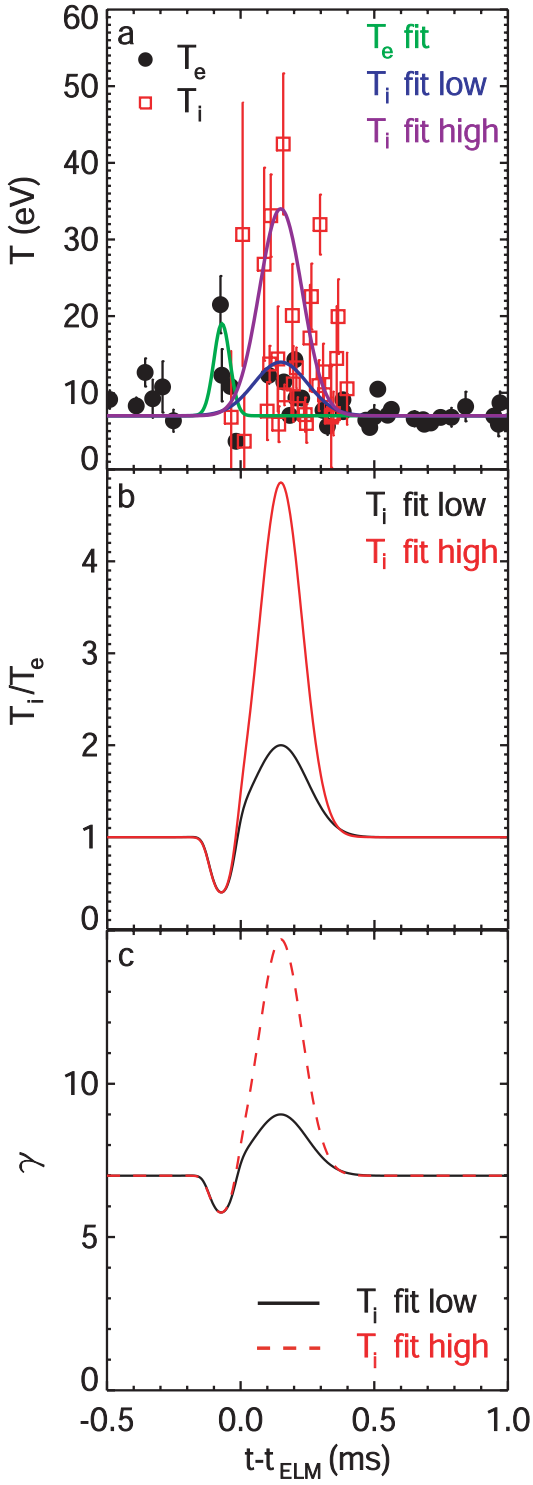

Figure 5.23: (a) T_i and T_e data in type I ELMs with fits to the data, (b) T_i/T_e as a function of time through the ELM for a low (black) and high (red) fit to the T_i data. Using equation 2.11 from chapter 2, γ has been calculated for the low T_i fit (black solid line) and for the high T_i fit (red dashed line).

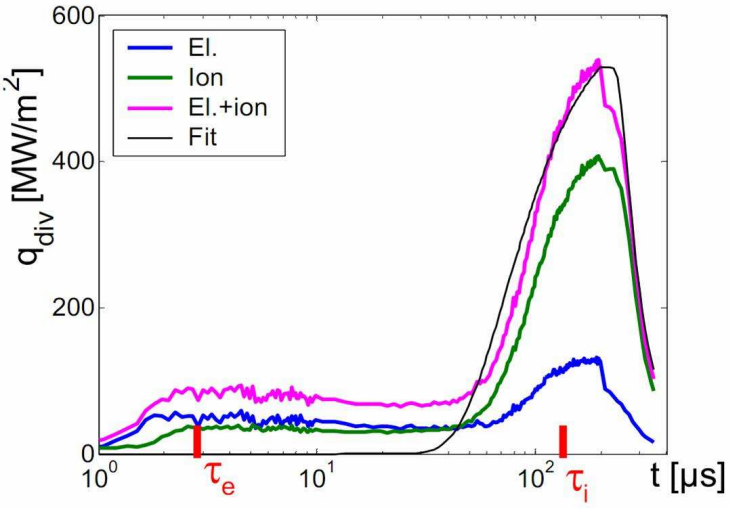

Figure 5.24: Power loads to the divertor plate during Type-I ELM with W_{ELM}=0.4 MJ from [83].

ELM energy is deposited to the divertor targets on the ion timescale, $\tau_{i,\|}$, however there will be a peak due to the hot electron flux which arrives on the hot electron timescale, $\tau_{e,\|}$.

This picture is consistent with measurements made by the divertor RFEA. A peak in V_s is seen at the start of the RFEA measurements which coincides with the increase in T_e seen by the LP. This is followed by an increase in T_i due to ions arriving later than the electrons. At a similar time the currents peak on both the RFEA slit plate and collector plate, suggesting the remaining particles released by the ELM arrive at the RFEA at a similar time to the hottest ions. The sheath potential also decreases at the time the ion current increases. This is consistent with ions from the ELM arriving at the target which reduces the sheath potential to the value for a quasi-neutral target plasma.

Comparison to ELM models and experimental measurements on other tokamaks

The kinetic 1D PIC model by Tskhakaya et al [83] used to make simulations of type I ELM parallel transport in the JET SOL shows agreement with the trends seen in the MAST measurements by RFEA. By modelling the transport of electrons and ions to the target the model shows an early arrival of electron heat loads on the electron timescale followed by the remaining ion and electron heat load which is deposited to the target on the ion timescale, see figure 5.24 [83]. The initial electron heat flux is expected due to their higher mobility but due to the parallel electric field resulting from the hot electrons travelling to the target, the remaining electrons travel with the ions and the electron heat load is deposited with the ion heat load $\sim$ 150 μs later. The time delay between the electron and ion heat loads is similar to the difference between the measured peaks in T_e and T_i on MAST.

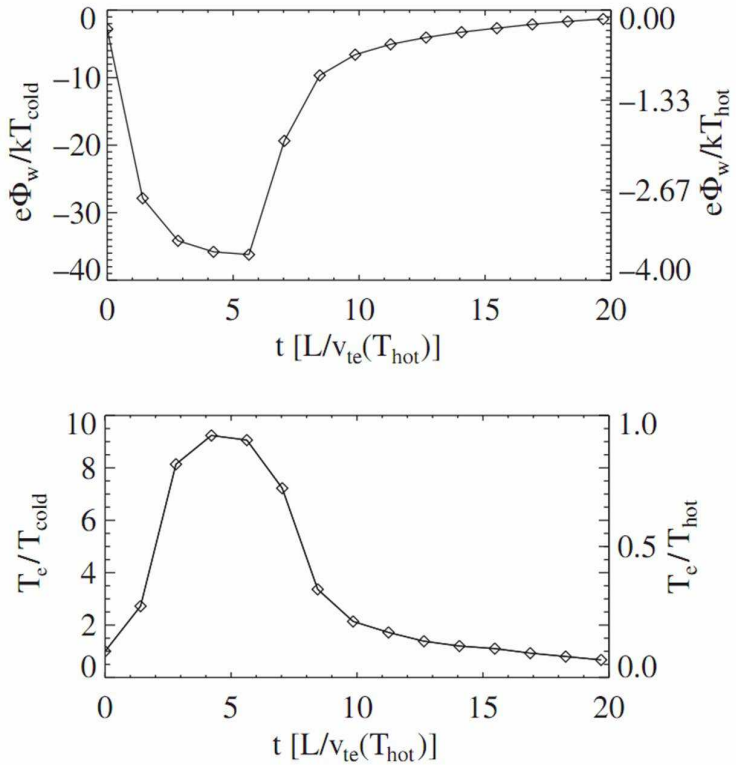

Figure 5.25: Top: electric potential at the target plate versus time; bottom: electron temperature in front of the sheath versus time from [84].

Similar results are found in the kinetic PIC model by Bergmann et al [84] where a portion of the electron energy is deposited on the electron timescale but the bulk of electron and ion energy is deposited on the ion timescale. Further results from Bergmann [84] show an increase in T_e and V_s on the electron timescale, see figure 5.25 [84], which is consistent with the increases seen in T_e and V_s in the MAST measurements, see figures 5.17 and 5.19. The values of T_e and V_s in the code can be seen to return to the pre-ELM values by $t = 20\tau_{e,\|}$. For type I ELMs on MAST $\tau_{e,\|} \sim 4$ μs and since the peak V_s occurs $\sim$ 50 - 100 μs before the peak in I_0 this is consistent with a time of $\sim 20\tau_e$.

The same trends for hot electrons arriving before the bulk particles released from the ELM due to their higher mobility can be seen in results from Fundamenski et al [85] where the energy flux peaks earlier in the ELM evolution than the particle flux, see figure 5.26 [85]. The fluid code used by Fundamenski et al [85] predicts a peak of $T_i/T_e \sim 3$ for ELMs in deuterium plasmas, see figure 5.27 [85]. These results are in agreement with transient modelling of ELMs on JET which predicts $T_i/T_e = 1$ - 2.5 [17]. They are also consistent with findings on MAST where $T_i/T_e = 1$ - 4.8 in ELMs arriving at the target, see figures 5.21 - 5.23.

Measurements made on JET by IR and LP of divertor particle and power profiles are used to calculate the sheath heat transmission at the target as it evolves during the ELM, see figure 5.28 [86]. These measurements have shown two peaks associated with the electron and ion heat flux, each arriving on the electron and

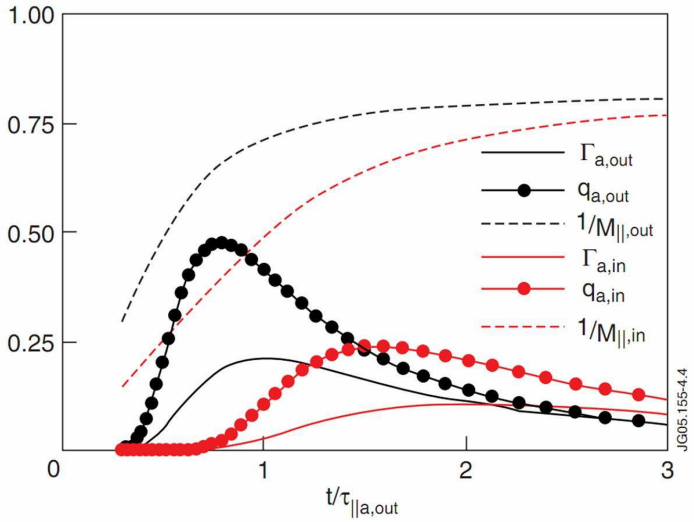

Figure 5.26: Temporal evolution of particle and energy fluxes deposited on the outer and inner divertors; corresponding Mach numbers are also indicated. Γ_a and q_a are given in units of $n_{0,a}/\tau_{||a}$ and $\epsilon_{0,a}/\tau_{||a}$, respectively from [85].

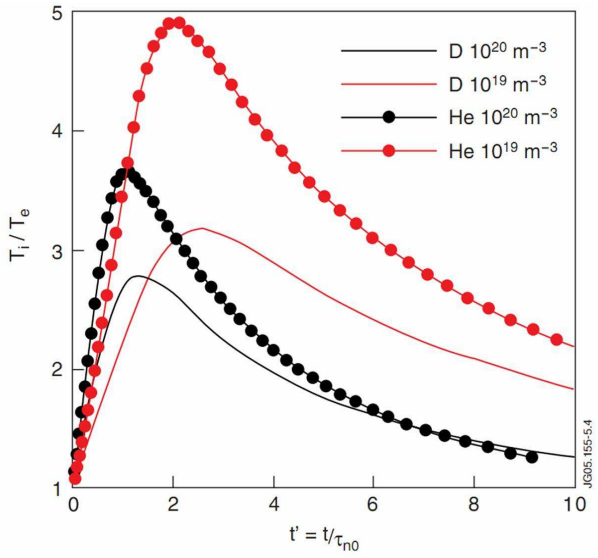

Figure 5.27: Temporal evolution of the ratio of the ion and electron temperatures based on results of the fluid model from [85].

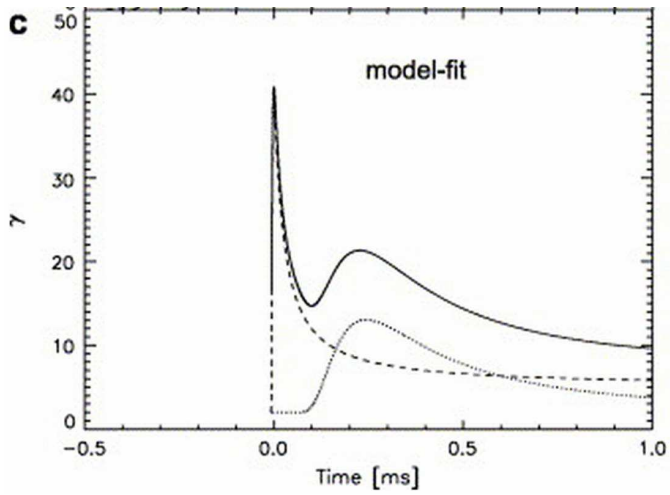

Figure 5.28: Modelled total (solid), electron (dashed) and ion (dotted) sheath transmission factor from [86].

ion timescales respectively. There is an almost instantaneous increase in the sheath heat transmission when the ELM arrives at the target, thought to be due to fast hot electrons arriving to the target first. Although the equation used to calculate the sheath heat transmission factor from measured T_i/T_e in MAST does not capture the peak due to hot electrons, a peak consistent with the ions is seen in figure 5.23(c).

Divertor target currents measured in TCV during ELMs by Pitts et al [87] show evidence of the fast electron component arriving before the bulk ELM. The measurements also show a rapid complex rearrangement of potential in the target vicinity before the D_α signal responds to the ELM. The TCV results are in qualitative agreement with 1D PIC modelling by Bergmann et al [84] showing an initial burst of fast electrons, as seen on MAST, followed by the ion heat pulse and the remainder of the energy deposited on the ion timescale, see figure 5.29 [84]. Average j_{sat} measurements at a similar distance from the strike point on TCV as the measurements made on MAST have a higher value of ~ 5 Acm^{-2} whereas on MAST the peak j_{sat} values are of 0.7 and 0.65 kAm^{-2} for type III and type I ELMs respectively. On TCV, T_e measurements are seen to peak at 1.7 $\times$ pre-ELM value ~ 100 μs before the peak j_{sat} measurements which is a similar delay to the type I ELMs on MAST. Measurements of type I ELMs in JET show an increase in T_e of 2.3 $\times$ pre-ELM T_e [88]. This is similar to the type I ELMs measured on MAST which show an increase of T_e in the ELM ~ 2.5 $\times$ pre-ELM value.

The measurements made by RFEA of T_i, V_s and I_0 and the comparison LP measurements are shown to be in qualitative agreement with modelling of ELMs and measurements on other fusion devices. RFEA measurements on MAST show evidence for hot electrons arriving before the remaining ions and electrons released by the ELM. Measurements also show $T_i > T_e$ through the ELM evolution with $T_i/T_e = 1$ - 4.8, which is in agreement with fluid modelling.

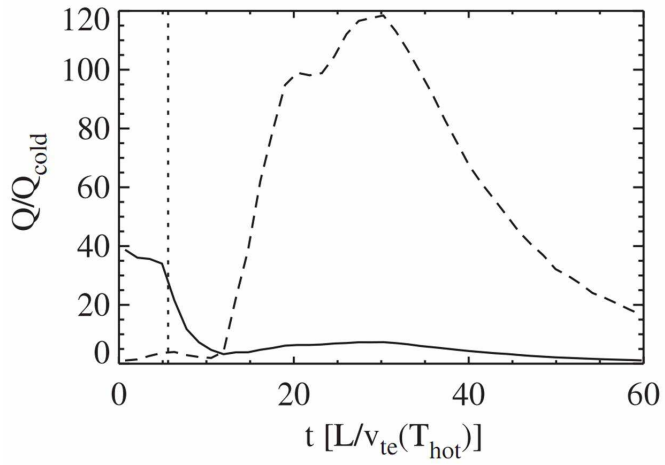

Figure 5.29: Energy fluxes at the entrance to the sheath in front of the target plate; solid line: electrons, dashed line: ions from [84].

5.5 Summary

Measurements have been made of the ion temperature at the divertor in inter-ELM H-mode and have shown that across a radial target profile $T_i = 6-20$ eV with $T_i/T_e = 1-3$ over a range of plasma parameters. It has been shown that for a position of $\Delta R^{tgt}_{LCFS} = 6.5$ cm, T_i/T_e scales with connection length as may be expected since for longer parallel distances the electrons and ions have a longer parallel transport time over which to equilibrate before they reach the divertor target. The differences of T_i/T_e over the range of discharges measured can be explained to some extent by the thermal coupling, R_{th}, of ions and electrons although upstream T_i measurements would be a valuable additional measurement to explain the trends seen at the target. Scenario B with the highest I_P and P_{NBI} gives the highest value of T_i/T_e measured at the target in MAST, although measurements at the strike point could not be made. This plasma discharge will be investigated by the 1D fluid model, SOLF1D, in chapter 6.

The first attempt to measure ELMs at the target of MAST by RFEA have been made using two operational methods. An average ELM temperature measurement has been made in type III ELMs at two different locations which show a fall off of temperature with distance from the LCFS at the target. Further measurements have been made with the fast swept voltage method which allows measurements during the arrival of particles released by the ELM at the target. These measurements have shown in both type I and type III ELMs an early arrival of hot electrons, followed by hot ions slightly ahead of the bulk ion and electrons which arrive on the ion timescale. These measurements are consistent with kinetic modelling of ELMs and measurements made on other tokamak devices. Further measurements of ELMs arriving at the target will be made in MAST by RFEA to give more statistics and also more radial profile information, however these measurements will not be part of this thesis.

Chapter 6

Effect of SOL flows on T_i measurements

6.1 SOLF1D modelling of the MAST SOL

As mentioned in section 3.1, parallel Mach flows, $M_{\parallel}$, in the SOL can cause measurements of T_i made by RFEA probes to be overestimates of the local T_i. The accuracy of RFEA T_i measurements can be improved by a correction factor to remove this effect which has been determined by Valsaque et al [65], however $M_{\parallel}$ must be known at the RFEA entrance. There are currently no experimental measurements for $M_{\parallel}$ near the MAST target so the 1D fluid model of the SOL, SOLF1D, has been used to model the MAST SOL for two plasma discharges measured by the target RFEA in chapters 4 and 5, to investigate the plasma flow at the entrance of the target RFEA probe.

SOLF1D models the SOL plasma as individual flux tubes between two targets. In order to produce simulated measurements equivalent to the measurements made by the RFEA, several flux tubes are modelled at different radial positions across the SOL. To produce equivalent flux tubes to those in experiment, field line tracing is used to follow field lines intercepting the target at 1 cm intervals upstream to the midplane so that SOLF1D runs are initiated from the equivalent ΔR^{up}_{LCFS} position. The ΔR^{up}_{LCFS} position is used to choose input sources for SOLF1D of T_e and n_e from experimental measurements by Thomson scattering. The upstream T_i input can be defined separately to T_e which allows different upstream T_i models to be investigated, for example $T^{up}_i = 2T^{up}_e$. The flux tube geometry in MAST is represented in SOLF1D using the connection length between the targets, $L_{\parallel}$, found by field line tracing, and the magnitude of the magnetic field along $L_{\parallel}$, which SOLF1D uses to calculate flux expansion along the simulated flux tube.

Modelled target profiles, which are directly comparable to experimental measurements by LP, are produced by taking T_e and n_e values at the target for each SOLF1D flux tube arriving at a given ΔR^{tgt}_{LCFS}. T_i measurements are taken from the modelled flux tube at the position equivalent to the entrance of the RFEA along

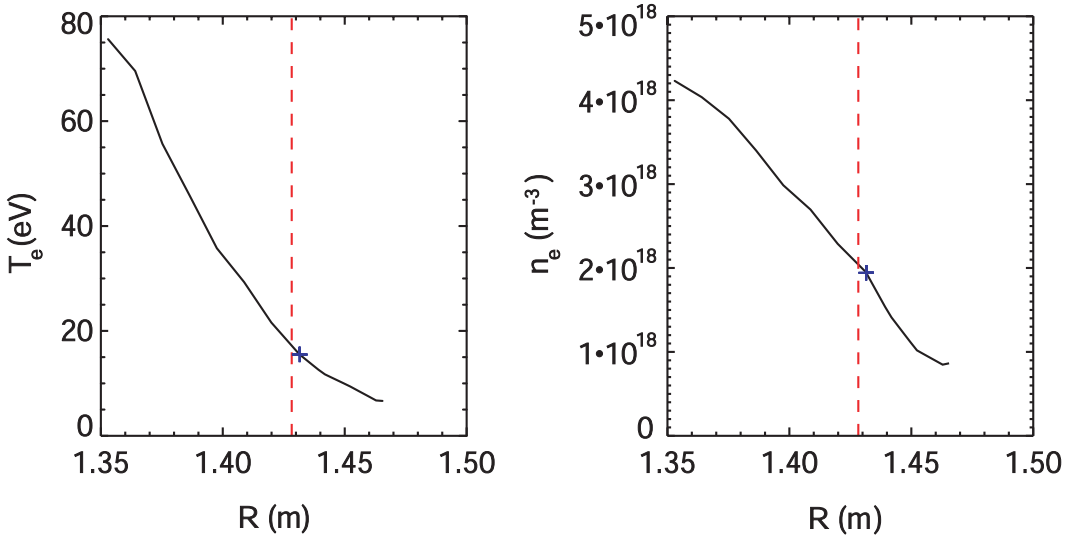

Figure 6.1: Example midplane Thomson scattering input profiles used for L-mode SOLF1D modelling. The blue crosses show the inputs used for the flux tube modelled closest to the LCFS at $\Delta R^{tgt}_{LCFS} = 0.01$ m. The red dashed lines show the position of the LCFS.

$L_{\parallel}$, which is found using the divertor RFEA probe geometry in the target and the magnetic pitch angle for a particular plasma discharge.

Figure 6.1 shows example upstream input profiles for the low density $I_P = 400$ kA L-mode discharge in chapter 4 (26798); target measurements are shown in figure 4.2. Once the position of the LCFS is determined in radius from EFIT and camera data, shown in figure 6.1 as a red dashed line, the input temperature and density are found for each modelled flux tube by using ΔR^{up}_{LCFS} found by field line tracing. The input values of T_e and n_e used for the flux tube at $\Delta R^{tgt}_{LCFS} = 0.01$ m are shown on figure 6.1 as blue crosses. This flux tube has been used to give a comparison between SOLF1D and the two point model by comparing the target pressure determined from each model. Figure 6.2 shows the target pressure determined from the two point model in black and SOLF1D in red. SOLF1D calculates a lower pressure at the target than the two point model. This is because there is additional physical processes included in SOLF1D, for example flux expansion which will be discussed below, which are not in the two point model and these processes cause pressure loss along the flux tube between the upstream plasma and the target. This can be illustrated by removing flux expansion from the SOLF1D model for the same upstream parameters and calculating the pressure at the target from SOLF1D, see blue bar in figure 6.2. Removing flux expansion from SOLF1D increases the target pressure compared to the full SOLF1D model, therefore without flux expansion SOLF1D becomes more similar to the two point model. A further process which is included in SOLF1D is neutral recycling at the target. If no neutrals are included in the SOLF1D model then the target pressure calculated from SOLF1D for the same upstream inputs is higher, shown as the green bar in figure 6.2. In this case SOLF1D calculates the target pressure to be almost equal to the two point model.

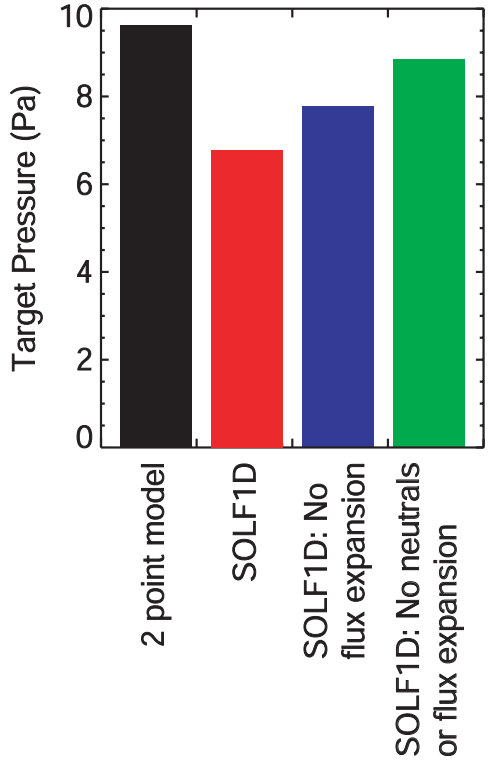

Figure 6.2: Target pressure calculated from the same upstream parameters for an L-mode plasma flux tube at $\Delta R^{tgt}_{LCFS} = 0.01$ m using (i) the two point model, shown in black, (ii) the full SOLF1D model, shown in red, (iii) SOLF1D without flux expansion, and (iv) SOLF1D without flux expansion or neutrals included.

The two point model is most applicable for sheath-limited or simple SOL regimes where there are no parallel temperature gradients in the SOL [24]. Since the L-mode plasma which has been modelled by SOLF1D is in the conduction limited regime with collisionalities in the range $10 \leq \nu^*_{SOL} \leq 50$ it is likely that the two point model description of the SOL will not be sufficient and therefore SOLF1D would give a better description which will not necessarily match the two point model description. Figure 6.3 shows a comparison between the two point model and SOLF1D of the target pressure for several upstream inputs with different collisionalities. As the upstream SOL collisionality increases, the SOLF1D calculation for the target pressure reduces and therefore is further from the target pressure calculated from the two point model. This trend is expected to continue so that at high collisionallities where $\nu^*_{SOL} > 50$, there would be larger discrepancies between SOLF1D and the two point model.

To investigate the effect of the neutral coefficient, R_{ec}, on SOLF1D modelling and to ensure a reasonable choice of R_{ec} is used when modelling target profiles, one flux tube at $\Delta R^{tgt}_{LCFS} = 0.01$ m has been used to compare neutral coefficients of $R_{ec} = 0$, 0.1, 0.2, 0.5 and 0.99. Figure 6.4 shows the plasma and neutral densities, the parallel Mach number, the total pressure, and the ion and electron temperatures along the flux tube as a function of $L_{\|}$ for the range of neutral coefficients investigated. Since

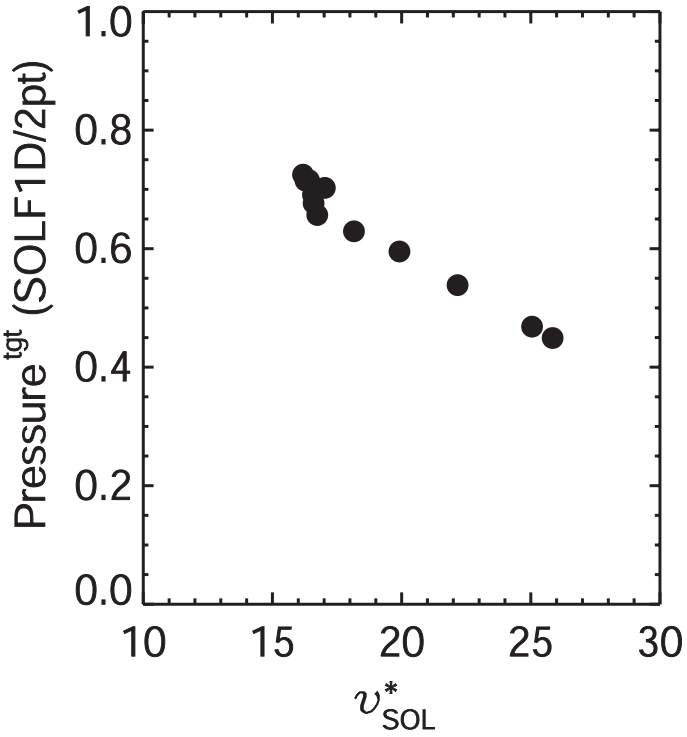

Figure 6.3: Ratio of the target pressure as calculated from SOLF1D and the two point model as a function of SOL collisionality calculated at the midplane.

present day tokamaks operate with R_{ec} close to unity [24], $R_{ec} = 0.99$ was initially chosen, however as can be seen from figure 6.4, the target density when using such a high recycling coefficient gives large density peaks close to the targets which is not seen on MAST [89]. This behaviour is common on other devices such as JET [90], however due to the open divertor on MAST it does not give a good description of the MAST SOL which has a comparatively smaller particle source due to recycling than JET [91]. The density from SOLF1D without neutrals gives no peaking at the target which is a better match to typical Onion Skin Modelling (OSM) of MAST plasmas where only slight peaking is seen at the targets [92]. Recycling coefficients in the range $R_{ec} = 0-0.2$ would be a reasonable choice for MAST, because although this is lower than expected in a typical tokamak divertor, in order to give a more realistic description of MAST, a low R_{ec} is necessary since in reality not all of the neutrals resulting from ion impact on the target will return along the same field line as the incident ion. In fact due to the open divertor in MAST a large number of neutrals will be lost to the vessel without significant interaction with the divertor plasma, unlike the divertor in JET for where the target is vertical [90]. The divertor geometry affects the neutral recycling at the target [93] and therefore the modelling must be chosen to reflect the MAST divertor. At high R_{ec} there is a large unphysical drop in total pressure in front of the targets. This steep drop in total pressure is not expected before the target and recycling coefficients of $R_{ec} < 0.5$ give a better match to the total pressures modelled by OSM on MAST [92].

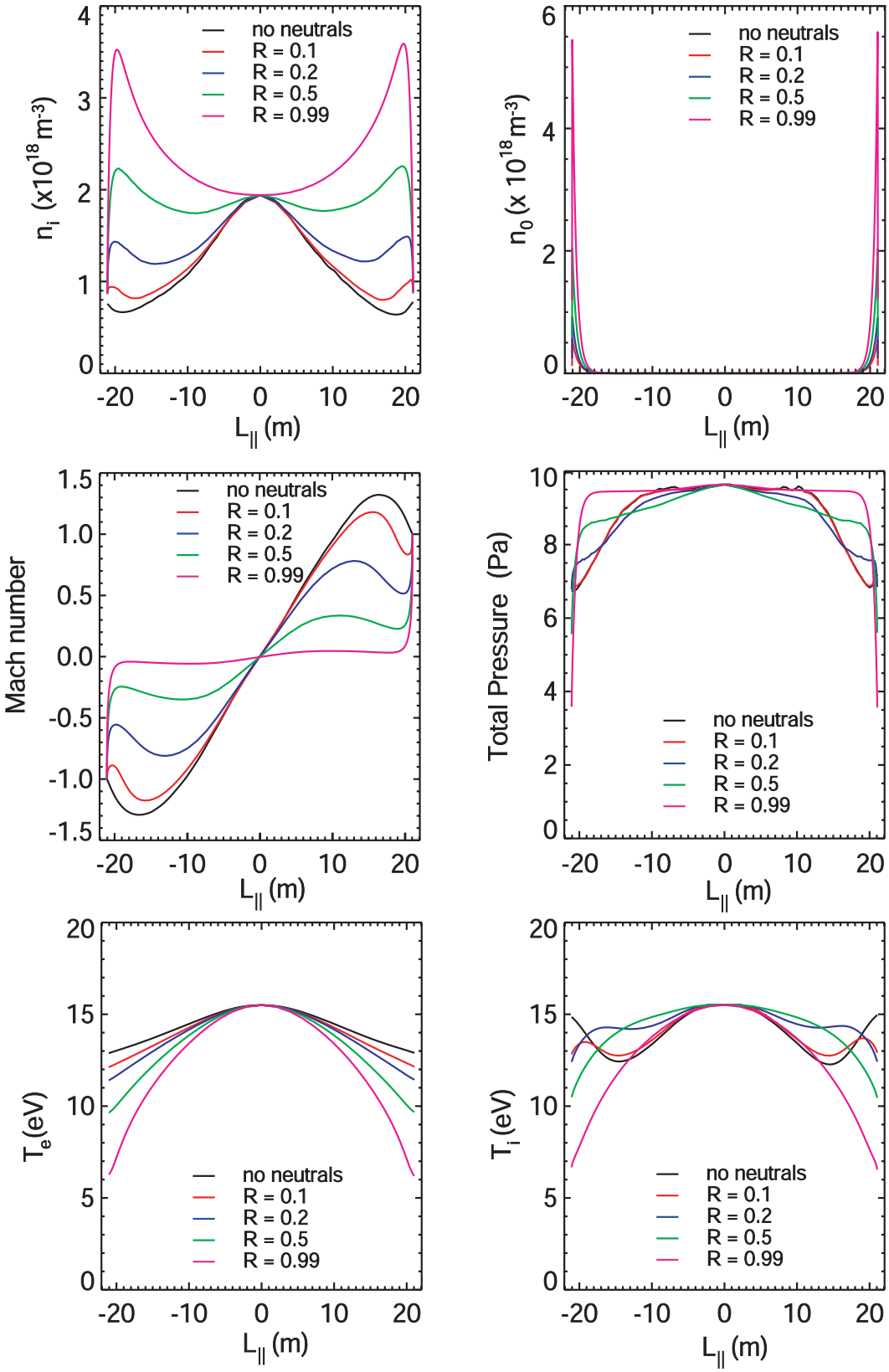

Figure 6.4: Effect of different neutral recycling coefficients, R_{ec} on plasma and neutral density, parallel Mach number, total pressure and ion and electron temperatures along a SOL flux tube at $\Delta R^{tgt}_{LCFS} = 0.01$ m as a function of $L_{\parallel}$.

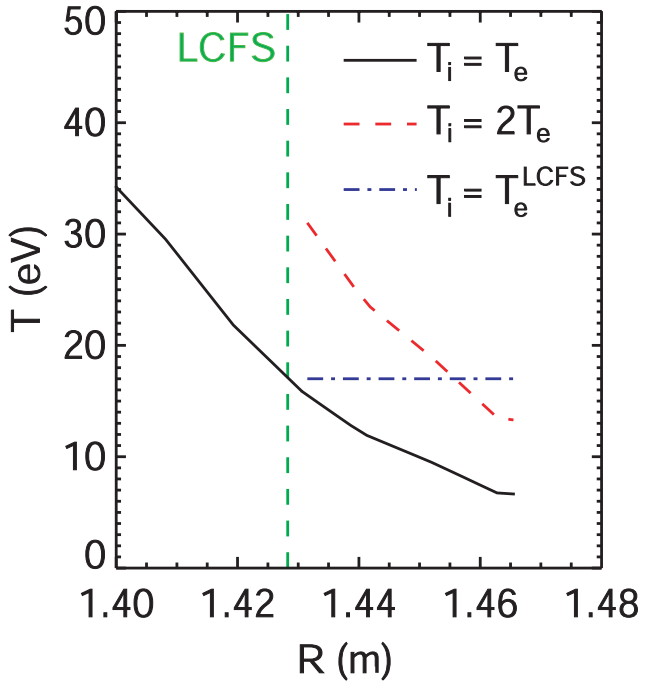

Figure 6.5: Upstream T_i profile models used as inputs for SOLF1D to investigate the effect of T_i^{up} on target parameters.

When comparing experimental measurements of T_i and T_e and SOLF1D it is important to choose the correct recycling coefficient since it can be seen in figure 6.4 that R_{ec} can affect the temperatures close to the target. For $R_{ec} = 0$ - 0.1 the Mach flow profile, shown in figure 6.4, becomes supersonic before reaching the targets and since this is not physical, neutral coefficients below 0.1 will not be used in SOLF1D. To give the most physical match to a typical MAST discharge $R_{ec} = 0.2$ has been used for all SOLF1D modelling which will follow in this chapter.

6.1.1 L-mode target parameter modelling

The lowest density L-mode discharge with $I_P = 400$ kA (#26798: see figure 4.2 in chapter 4) has been modelled by SOLF1D. From upstream measurements of T_i made by the midplane RFEA it was found that $T_i^{up} \sim 2T_e^{up}$, however since the upstream T_i and T_e can be specified in SOLF1D three upstream models for T_i have been investigated. The upstream T_i models are $T_i = T_e$, $T_i = 2T_e$ and $T_i = T_e^{LCFS}$, where T_e^{LCFS} is the value of T_e at the upstream LCFS kept constant in radius for SOLF1D inputs, see figure 6.5 for profiles of T_i^{up}. All T_e and n_e inputs are taken from TS measurements in the same plasma discharge at the midplane.

Profiles have been produced using 14 flux tubes modelled by SOLF1D at different radial positions through the SOL. The input parameters: T_e, T_i, n_e and $L_{\|}$ have been changed dependent on the radial position of each flux tube. No upstream flows have been used, but these will be investigated later since on MAST flows of $M_{\|} \sim 0.2$ have been measured at the midplane [60]. The resulting target 'profiles' from

SOLF1D are shown in figure 6.6, where T_i from SOLF1D is taken at the effective entrance to the target RFEA (i.e above the target along $L_{\|}$ calculated using the pitch angle at the target) and measurements of n_e and T_e are taken at the target. The temperature and density have been used to calculate j_{sat} at the target using the measured T_e, n_e and T_i so that it is equivalent to j_{sat} measurements by LP. Experimental measurements from 4.2 are repeated in figure 6.6 to allow comparison.

Figure 6.6(a) shows T_e and T_i at the target for the three upstream models of T_i. $T_i = T_e$ upstream gives the closest match to experimental target profiles of T_i and T_e. $T_i^{up} \sim 2T_e^{up}$ has been measured by an RFEA at the midplane in MAST, see figure 4.17, however which shows that SOLF1D does not give a good match to experimental measurements in the MAST SOL. T_e values close to the strike point are similar to those measured by LP however the measured T_e has a flatter radial profile than SOLF1D. J_{sat} as calculated from the modelled T_e, T_i and n_e at the target is similar to j_{sat} measured by LP but slightly higher. SOLF1D profiles of T_e and j_{sat} match well to LP close to the strike point however the fall off length is noticeably difference between SOLF1D and experiment. Since SOLF1D is a 1D code with no radial transport information it is possible that the modelled profiles will have shorter fall off lengths than experimentally measured profiles. Considering the effect of cross field transport of both plasma particles and neutrals it is likely that the temperatures near the strike point would be reduced and the SOL profile would flatten. Therefore with the added cross field information a better match may be found between experimental measurements and the SOLF1D modelling with $T_i = 2T_e$ upstream which is consistent with experiment, see figures 4.2 and 4.17. A two dimensional model of the SOL, SOLPS [54, 55], which includes cross-field transport in the SOL would give an improved description of the experimental measurements made in MAST, however this is beyond the scope of this thesis. The most important result from SOLF1D modelling is $M_{\|}$ at the entrance to the RFEA which will be explored in section 6.1.3. Comparison between SOLF1D and the more complex SOLPS model has shown that SOLF1D provides a good match to SOLPS for parallel flows, $M_{\|}$, close to the target [56] which is the region of most interest in this thesis.

The target profiles from SOLF1D shown in figure 6.6 have a fixed upstream flow of $M_{\|} = 0$, however since flows of $M_{\|} \sim 0.2$ have been measured at the midplane in MAST [60], the effect of upstream flows on the temperature and density at the target have been studied. Figure 6.7 shows the temperature and density as a function of upstream flow for two flux tubes at $\Delta R_{LCFS}^{tgt} = 0.01$ m and 0.10 m for each of the three upstream T_i models; (a) $T_i = T_e$, (b) $T_i = 2T_e$, and (c) $T_i = T_e^{LCFS}$.

Increasing the flow upstream can be seen to decrease the density at the target and marginally increase the target temperatures. Upstream flows do not have a large effect on the target temperature profiles which have been modelled by SOLF1D. If the flow is $M_{\|} \sim 0.2$, which is consistent with measurements on MAST [13, 42, 60], then the modelled target temperatures will not change greatly but the modelled

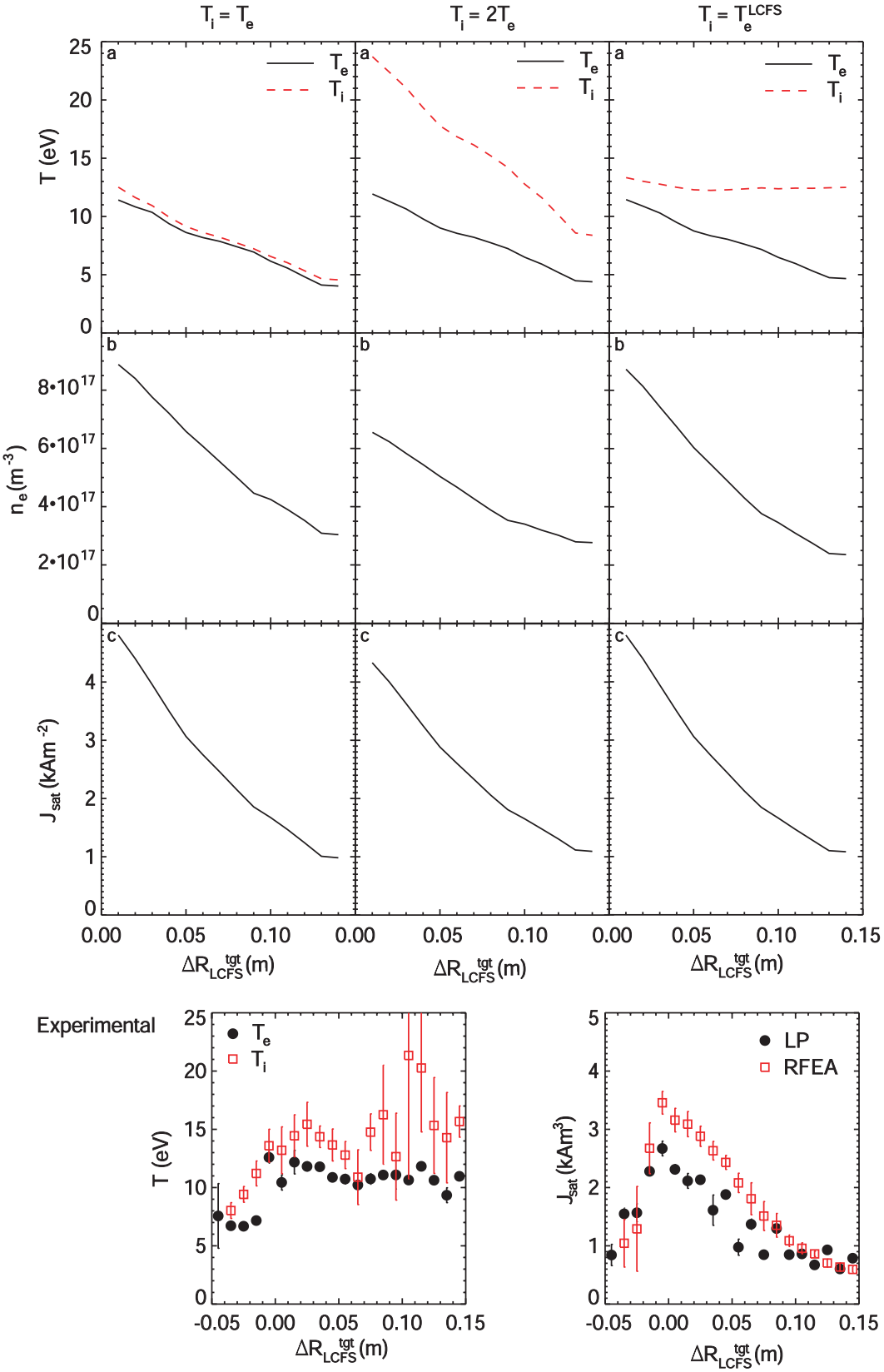

Figure 6.6: Simulated target profiles of (a) T, (b) n_e and (c) calculated j_{sat} for three T_i upstream models of $T_i = T_e$, $T_i = 2T_e$ and $T_i = T_e^{LCFS}$. Also shown are the experimental profiles from figure 4.2 for comparison.

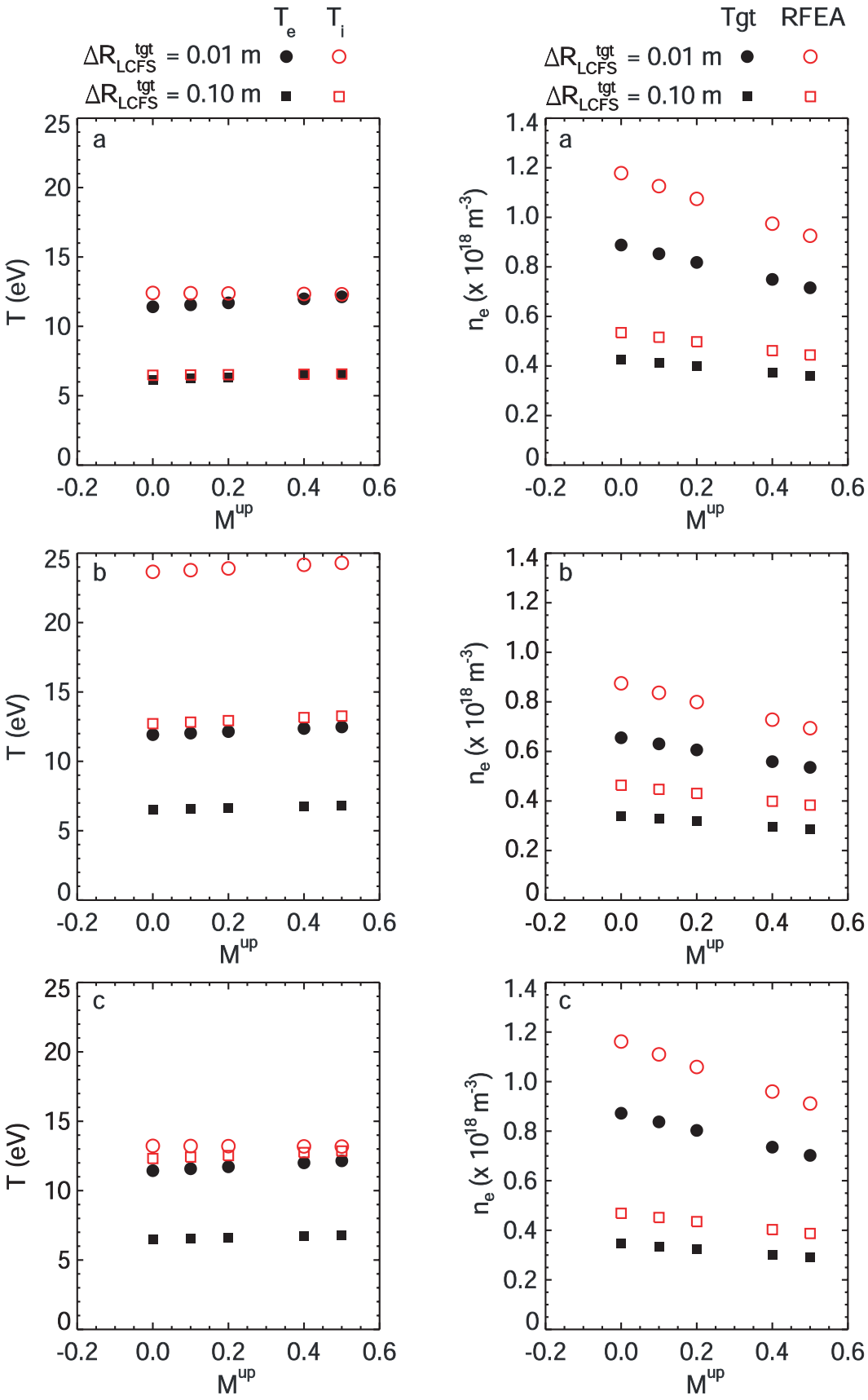

Figure 6.7: Target temperatures and densities as a function of upstream Mach number for two flux tubes in the SOL at $\Delta R^{tgt}_{LCFS} = 0.01$ m and $\Delta R^{tgt}_{LCFS} = 0.10$ m for (a) $T_i = T_e$; (b) $T_i = 2T_e$; and (c) $T_i = T_e^{LCFS}$.

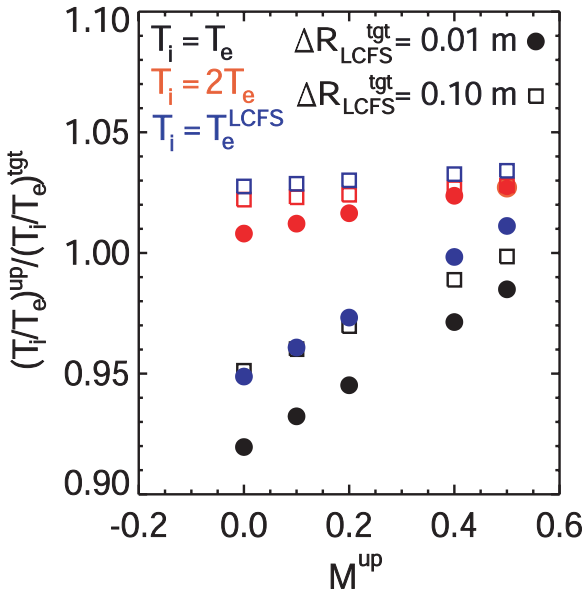

Figure 6.8: Effect of upstream Mach flows on the ratio of T_i/T_e upstream to target.

densities at the target and therefore the calculated j_{sat} from modelling will be closer to RFEA and LP measurements.

A comparison of $(T_i/T_e)^{up}$ to $(T_i/T_e)^{tgt}$ is shown in figure 6.8 as a function of upstream $M_{\|}$. For the upstream T_i model of $T_i = T_e$ there is a greater ratio of T_i/T_e at the target than the input parameters upstream with $(T_i/T_e)^{tgt}$ reduced further into the SOL. As $M_{\|}^{up}$ increases the difference between T_i/T_e upstream and at the target is smaller so that at higher values of M^{up} T_i/T_e remains constant along the flux tube. The upstream T_i model of $T_i = 2T_e$ shows that T_i/T_e is slightly reduced at the target compared to upstream but upstream flows have little affect on how this changes. For the upstream T_i model of $T_i = T_e^{LCFS}$ it can be seen that at $\Delta R_{LCFS}^{tgt} = 0.01$ m where T_i/T_e upstream is low, the ratio of T_i/T_e at the target is higher and here the upstream flows have a larger effect than at $\Delta R_{LCFS}^{tgt} = 0.10$ m where T_i/T_e upstream is large and the ratio is reduced at the target. Generally T_i/T_e is maintained over the flux tube and $(T_i/T_e)^{up} \sim (T_i/T_e)^{tgt}$. This result is important when attempting to model target inter-ELM H-mode ion temperatures where $(T_i/T_e)^{tgt}$ measured by the RFEA and LP is larger.

6.1.2 Inter-ELM H-mode target parameter modelling

An inter-ELM H-mode plasma with $I_P = 900$ kA and $P_{NBI} = 3.4$ MW (Scenario B: # 27743) has been modelled by SOLF1D because this plasma has the largest T_i/T_e experimentally measured at the target. Upstream T_e and n_e inputs have been taken from TS measurements at the midplane. Upstream T_i models of $T_i = T_e$, $T_i = 2T_e$ and $T_i = 3T_e$ were tested initially however these did not give T_i values at the target in the range of the experimental measurements, even when a reasonable match was found to T_e at the target. In an attempt to simulate the experimental T_i/T_e at the

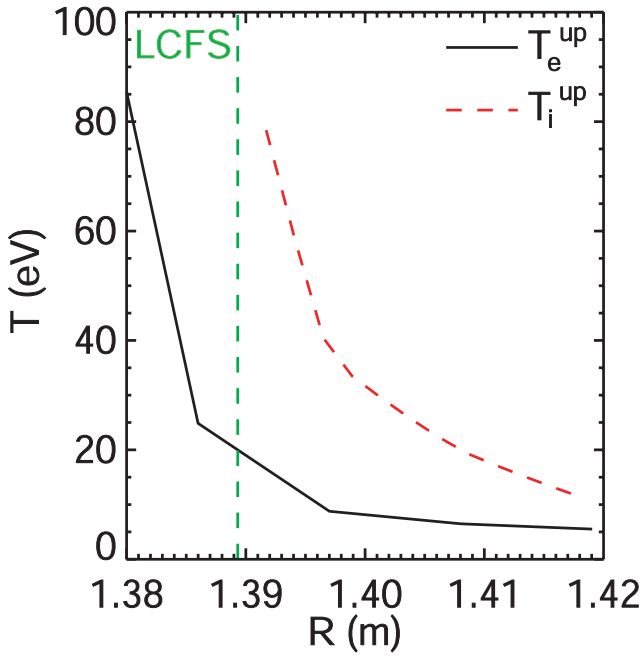

Figure 6.9: Upstream inputs for SOLF1D of T_e from Thomson scattering and the T_i model from experimental target measurements of T_i/T_e.

target, a model for the upstream T_i was used where $(T_i/T_e)^{up} = (T_i/T_e)^{tgt}_{exp}$. This was achieved by extrapolating T_i/T_e at the target over the range of ΔR^{tgt}_{LCFS} to be modelled in SOLF1D and using field line tracing to map up to the midplane and apply $(T_i/T_e)^{tgt}_{exp} = (T_i/T_e)^{up}$ to experimental T_e measurements from TS. Figure 6.9 shows the upstream T_e from TS and the upstream T_i model (as explained above) used as inputs for SOLF1D. Again, the radial measurements have been produced by modelling flux tubes radially into the SOL intercepting the target at 1 cm intervals over the range $\Delta R^{tgt}_{LCFS} = 0.01$ - 0.12 m.

The target profiles of T_e, T_i, n_e and the calculated j_{sat} are shown in figure 6.10. Also shown are experimental measurements of T_e, T_i and j_{sat} from figure 5.2 for comparison. T_e close to the LCFS at the target is higher than experimental measurements, however due to the lack of cross field transport in the SOLF1D model it would be expected that the modelled temperatures close to the LCFS could be higher than those measured experimentally. T_e modelled further into the SOL is consistent with measurements by LP. T_i from SOLF1D is similar to the experimental measurements made by RFEA in the range $\Delta R^{tgt}_{LCFS} = 0.05$ - 0.11 m, however this is only achieved when $(T_i/T_e)^{up} = (T_i/T_e)^{tgt}_{exp}$ is used for the T_i inputs. This means upstream $T_i/T_e = 2{-}4.75$ is required. This value is consistent with experimental measurements made of T_i upstream by RFEA in MAST which show $T_i/T_e = 2 \rightarrow 6$ [80], see figure 5.8 in chapter 5, however SOLPS modelling would be needed to further study the reasons for high T_i/T_e at the target.

Since the electron density calculated from LP measurements assumes $T_i = T_e$ the density from SOLF1D will not be compared to experiment but is included in figure

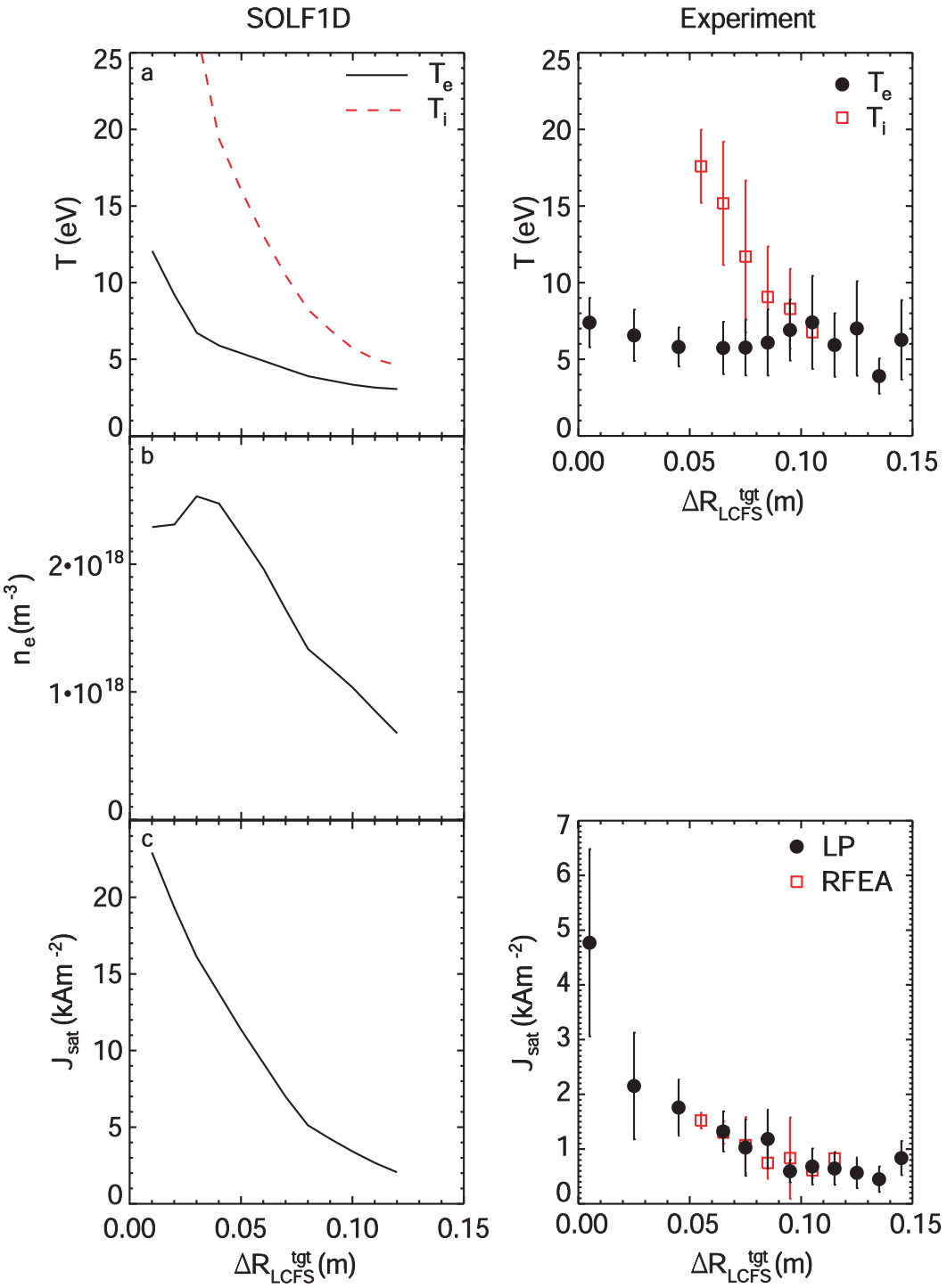

Figure 6.10: SOLF1D target profiles of T_e, T_i, n_e and calculated j_{sat} at the target. Also shown are the experimental measurements from figure 5.2 for comparison.

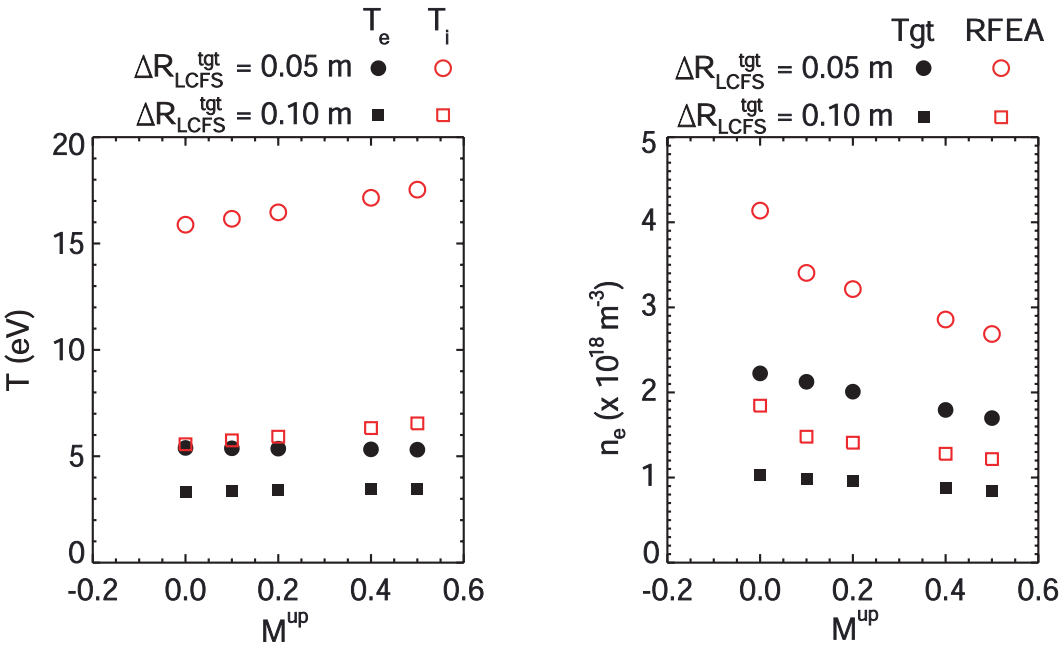

Figure 6.11: Temperature and density at the target as a function of upstream Mach flow for two flux tubes at ΔR^{tgt}_{LCFS} 0.05 m and 0.10 m.

6.10 for reference. J_{sat} as calculated from SOLF1D is higher than experimental measurements by LP however this may be due in part to the unrealistically high values of T_e, T_i and n_e from SOLF1D close to the LCFS which are likely due to the lack of cross field information in the model.

Upstream flows have been included at the midplane for SOLF1D runs of two flux tubes at ΔR^{tgt}_{LCFS} = 0.05 m and 0.10 m since these are the extremes of the experimental radial range of T_i measurements. Again the target temperatures increase with $M^{up}_{||}$ and the target densities decrease. Figure 6.12 shows the comparison between T_i/T_e upstream and at the target as a function of upstream $M_{||}$. Unlike the L-mode case where generally the ratio of T_i/T_e was maintained from the upstream to the target, in H-mode T_i/T_e decreases between upstream and the target. This is consistent with measurements made on MAST that show upstream T_i/T_e = 2 $\rightarrow$ 6 [80] whilst target measurements show T_i/T_e = 1 $\rightarrow$ 3. In the H-mode modelling, $(T_i/T_e)^{up}/(T_i/T_e)^{tgt}$ reduces with $M^{up}_{||}$ which is the opposite trend to L-mode modelling suggesting that as $M^{up}_{||}$ increases the ratio tends to unity so that the value of T_i/T_e is maintained along a flux tube in SOLF1D.

6.1.3 Estimates of $M_{||}$ from SOLF1D

As previously discussed in section 3.1, flows in the SOL affect measurements made by RFEA probes. In particular if a unidirectional RFEA is used in the SOL in the presence of flows a correction will be needed to give the correct ion temperature in the absence of the RFEA perturbation. This will be expanded on in the following section, however in order to determine the correction needed, the flow at the entrance

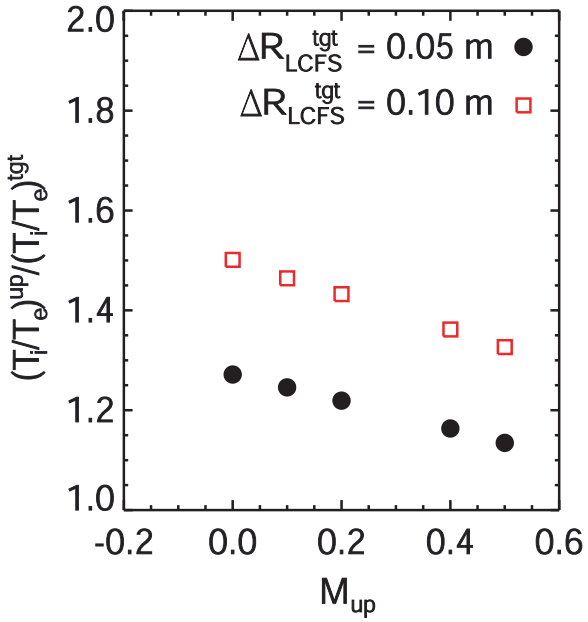

Figure 6.12: Effect of upstream Mach flows on the ratio of T_i/T_e upstream to at the target.

to the RFEA must be known. On MAST there is no diagnostic to measure $M_{||}$ near the target RFEA entrance however the modelled value for $M_{||}$ by SOLF1D can be used as an estimate.

Figure 6.13 shows the parallel flow, $M_{||}$, along the flux tube as a function of $L_{||}$ for two L-mode flux tubes modelled at (a) $\Delta R_{LCFS}^{tgt} = 0.01$ m and (b) $\Delta R_{LCFS}^{tgt} = 0.10$ m. $L_{||} = 0$ m represents the midplane and negative values of $L_{||}$ indicate the region between the midplane and the lower target. It can be seen that in front of the targets $M_{||}$ increases to $M_{||} = \pm 1$, which is the enforced boundary condition since we know that at the sheath entrance $v_{se} = c_s$ [24]. Again negative values indicate flows towards the lower target. From the pitch angle at the target, found by field line tracing, the distance between the point where a field line intercepts the target and the entrance to the RFEA can be calculated. For the L-mode discharge shown in figure 6.13 the RFEA entrance is ~ 6 cm above the target along the distance $L_{||}$. Although this distance is not large compared to $L_{||}$ in the MAST SOL, because $M_{||}$ changes greatly in the 10 cm in front of the target, $M_{||} < 1$ is expected at the RFEA entrance.

The flow at the target, $M_{||}^{tgt}$, and the flow at the RFEA entrance is shown in figure 6.14 as a function of distance from the LCFS at the target for the L-mode discharge modelled in section 6.1.1. The flow at the target is bounded by SOLF1D so that $M_{||}^{tgt} = 1$, however at the entrance to the RFEA, the flow is reduced to the range $M_{||} = 0.7$ - 0.8; the negative values are because the profile is at the lower target. The flow at the entrance to the RFEA is relatively unchanged radially across the target and over the varied upstream models for T_i. This gives a good indication that the flow is relatively unaffected by the upstream parameters and therefore a

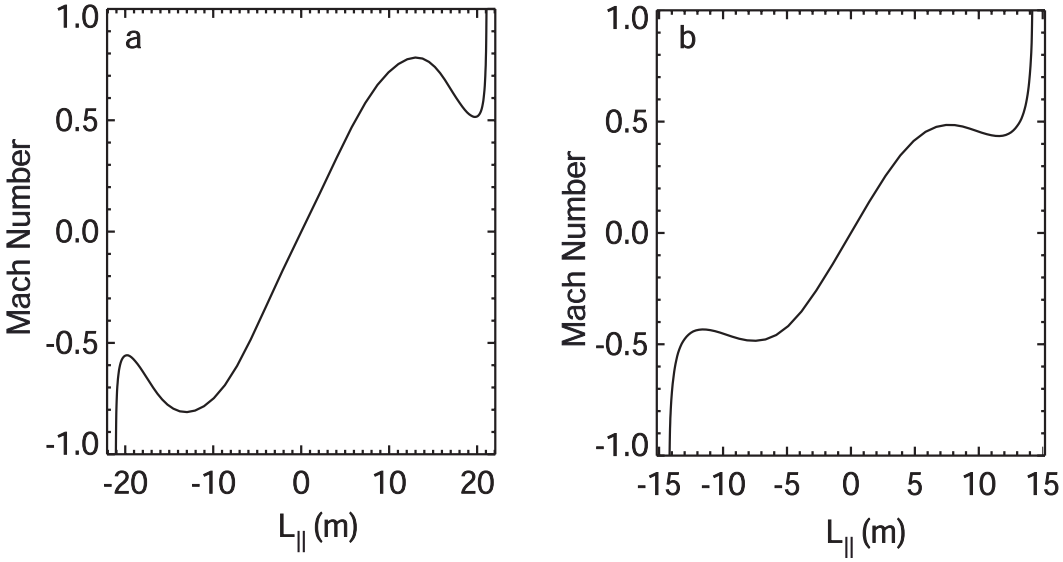

Figure 6.13: Example of the flow along two modelled flux tubes at (a) $\Delta R^{tgt}_{LCFS} = 0.01$ m and (b) $\Delta R^{tgt}_{LCFS} = 0.10$ m in the SOL for the modelled L-mode discharge.

value of $M_{||} = 0.7$ - 0.8 would be a reasonable estimate to give the correction to the RFEA T_i measurements.

Figure 6.15 shows the flow at the target ($M_{||} = 1$) and the flow at the entrance to the RFEA as a function of distance from the LCFS at the target for the modelled inter-ELM H-mode discharge. $M_{||}$ does not change dramatically over the flux tubes modelled and is in the range $M_{||} = 0.6$ - 0.7. This is a lower Mach number than the L-mode modelling however it is possibly because the RFEA entrance is further from the target as a function of $L_{||}$ in the inter-ELM H-mode discharge due to a lower pitch angle. The estimation for the flow in each discharge will be used to give a correction to each set of target T_i measurements by RFEA.

6.2 Effect of SOL flows on RFEA measurements of T_i

Bidirectional RFEAs in stationary SOL plasmas, i.e with no net Mach flow, measure the same temperature on both sides on the RFEA probe. For a Maxwellian distribution centred on zero parallel velocity, the RFEA sees the same distribution on both sides of the analyser and measures the temperature, which is the width of the distribution. In this case an I-V characteristic for each side of a bidirectional RFEA will have the same slope and therefore the same temperature is determined on both sides. In the presence of a parallel flow in the SOL this gives a shifted Maxwellian distribution in the frame of reference of the RFEA probe. Figure 6.16(a) shows a Maxwellian distribution with no flow and the shifted Maxwellian in the presence of parallel flows. The side of the RFEA facing the SOL flow, as is the case of the divertor RFEA, will see a larger part of the distribution which is the high energy end. Therefore the I-V characteristic for each side of the RFEA has a different slope,

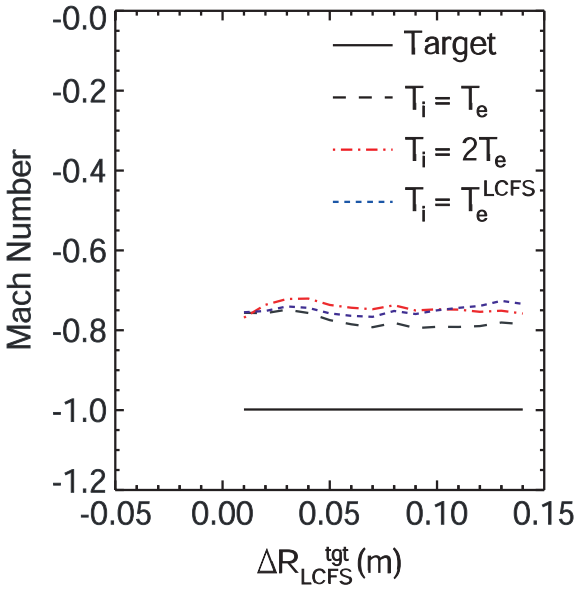

Figure 6.14: Simulated flows at the entrance to the RFEA for all three upstream T_i models and the flow at the target ($= c_s$) in the modelled L-mode discharge.

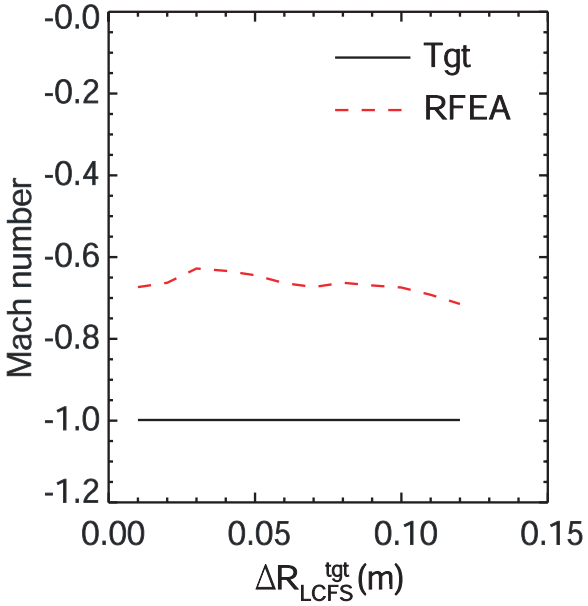

Figure 6.15: Simulated flow at the entrance to the target RFEA in the inter-ELM H-mode discharge modelled by SOLF1D.

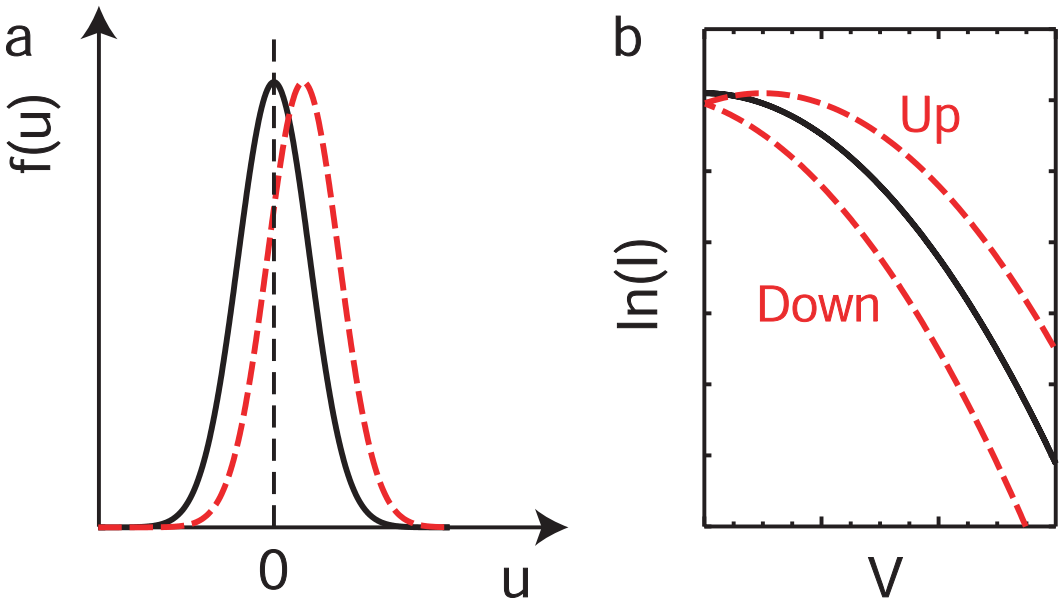

Figure 6.16: a) Maxwellian distribution of the parallel ion velocity (black line) compared to a shifted Maxwellian distribution in the presence of SOL Mach flows (red dashed line). b) Simulated I-V characteristics for an RFEA with no net SOL flow (black line) and in the presence of flows (red dashed lines). The labelled lines for the I-V characteristic in the presence of SOL flow shows the difference in temperature measured by the upstream and downstream sides of the RFEA.

where the upstream side is shallower and therefore measures a higher T_i as shown in figure 6.16(b). For measurements made on both the upstream and downstream sides of the RFEA the average of these two temperatures can be taken as the effective temperature at the position of the RFEA [65, 66]. For the divertor RFEA, however, the downstream temperature cannot be measured so the average can not be used. Instead the measurements by the divertor RFEA are likely to be an overestimate of the temperature at the target and a correction related to the parallel flow at the RFEA entrance can be found using modelling by Valsaque et al [65].

6.2.1 Valsaque model for correction to RFEA T_i measurements

Valsaque et al [65] have addressed the issue of estimating ion temperatures in the absence of the RFEA probe perturbation by applying correction factors. Kinetic modelling of the collisionless pre-sheath has been used to predict how these factors change when the SOL is characterized by different flow velocities and a range of T_i/T_e ratios. The data presented by Valsaque et al [65] have been extracted and a functional form of the data, for $T_i/T_e > 0.5$, has been used to produce figure 6.17. This shows the relationship between the Mach number in the SOL and the ratio of $T_i^{real}/T_i^{upstream}$ for values of $T_i/T_e = 0.5{-}2$, where $T_i^{upstream}$ is the experimentally measured T_i from an RFEA facing the parallel flow. It can be seen that the correction necessary for T_i measurements is not a strong function of T_i/T_e so this will be ignored when seeking a correction for the experimental data. The

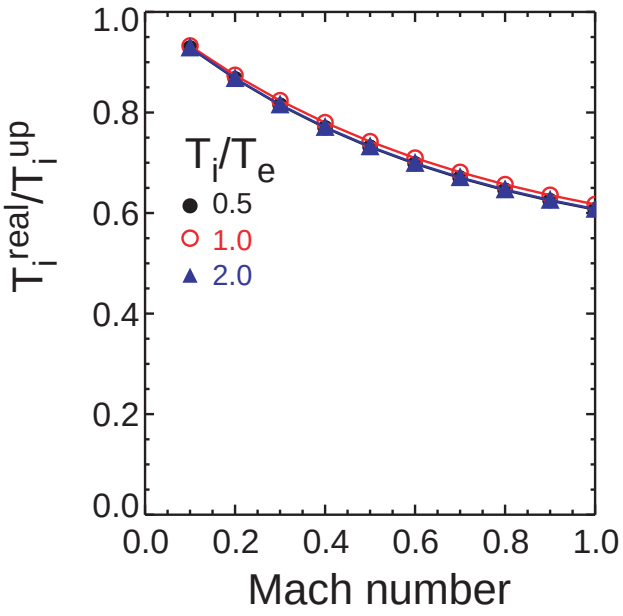

Figure 6.17: Correction necessary for unidirectional RFEAs facing a parallel flow as a function of $M_{\|}$ for $T_i/T_e = 0.5-2$.

correction factor is a stronger function of the parallel SOL Mach flow, showing for subsonic flows, a correction of up to 0.6 will need to be applied to the experimental measurements and therefore the target RFEA measurements will be an overestimate of the real target ion temperature.

In order to apply the appropriate correction to the data measured by the target RFEA the Mach flow at the entrance to the RFEA is needed. The SOL ions will be accelerated to the Bohm criterion, $v_{se} \geq c_s$ at the sheath edge [24], however the measurements made by the RFEA are above the target and therefore before this condition affects the parallel SOL flow. An estimate for the parallel Mach flow at the RFEA entrance was given by SOLF1D modelling of $M_{\|}$. These estimated values of $M_{\|} = 0.7-0.8$ in the L-mode discharge (#26798) and $M_{\|} = 0.6-0.7$ in the inter-ELM H-mode scenario B discharge (#27743) will be used to apply the appropriate correction to experimental measurements of T_i in the following section.

6.2.2 Corrections due to flows at the divertor RFEA

Using figure 6.17 the correction needed for the L-mode and H-mode discharges which have been modelled by SOLF1D can be estimated. For the L-mode discharge, Mach flows in the range $M_{\|} = 0.7$ - 0.8 are equivalent to a correction in the range 0.67 - 0.65. Applying this correction to the experimental RFEA measurements of T_i reduces T_i so that $T_i \leq T_e$. Figure 6.18 shows the T_i and T_e measurements made by RFEA and LP respectively. Also plotted are the corrected T_i measurements where $T_i^{real}/T_i^{upstream} = 0.67$ (blue circles) and 0.65 (blue square). T_i/T_e as a function of distance from the LCFS at the target is also shown in figure 6.18 and it can be seen that T_i/T_e has reduced from the experimental measurements of T_i/T_e

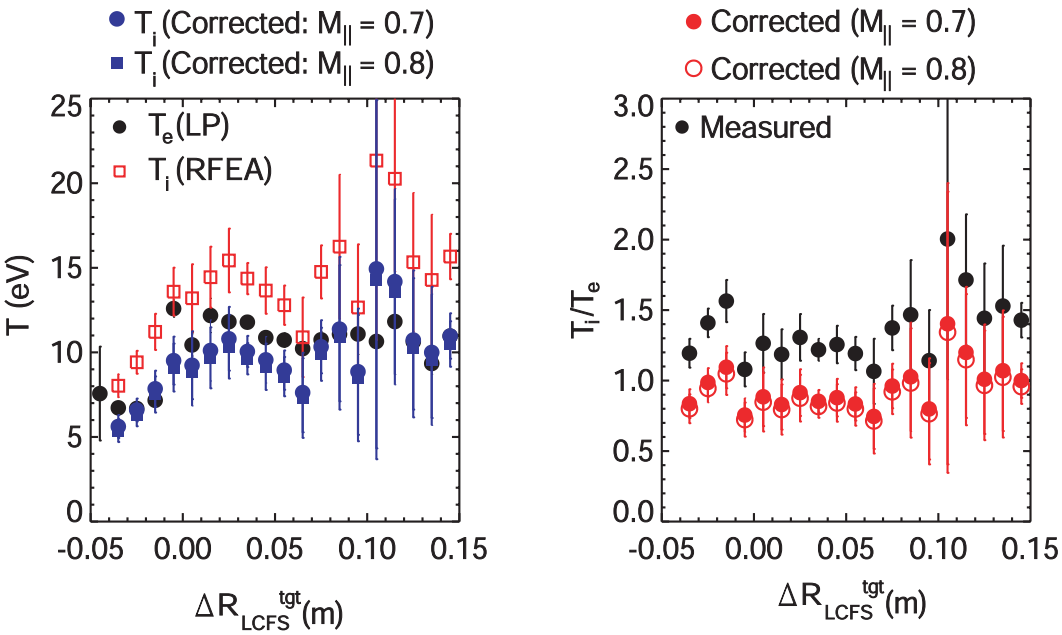

Figure 6.18: L-mode T_i and T_e profiles as a function of ΔR^{tgt}_{LCFS} compared to corrected T_i profiles. Also shown is T_i/T_e at the target compared to corrected ratios.

= 1 - 1.5 to $T_i/T_e \leq 1$.

Since the measurement of the flow at the RFEA entrance did not alter greatly over the range of parameters used to modelled this L-mode plasma discharge it is likely a similar correction would be needed for the other L-mode discharges. This would bring all ohmic L-mode discharges (not shown) to a ratio of $T_i/T_e \sim 1$ or lower. In the beam heated L-mode discharges (not shown) T_i/T_e would remain greater than the ohmic discharges, however the ratio would be reduced to $T_i/T_e \sim$ 1.3 instead of the measured $T_i/T_e \sim 2$ in the SOL.

The flows simulated by SOLF1D at the RFEA for the inter-ELM H-mode discharge are in the range $M_{||} = 0.6$ - 0.7. This is equivalent to a correction factor as determined by Valsaque [65] of 0.67 - 0.70. Figure 6.19 shows the experimental measurements of T_i and T_e by RFEA and LP respectively along with T_i with the corrections of 0.67 (blue solid circles) and 0.7 (blue hollow circles) applied. This reduces T_i to a maximum of $T_i \sim 12$ eV in the measured radial range. Also shown in figure 6.19 is T_i/T_e as a function of distance along the target for the measured values by RFEA and LP and using corrected T_i. It can be seen that with the correction $(T_i/T_e)^{max} \sim 2$ and further into the SOL $T_i < T_e$.

Applying a similar correction to the experimental T_i values measured in further inter-ELM H-mode scenarios (not shown) would show $T_i/T_e \approx 0.7$ - 1.5 at the target. Lower values of T_i/T_e are expected at the target compared to the midplane since OSM modelling predicts that $T_i = T_e$ at the target even when $T_i > T_e$ at the midplane [40]. These corrected target values for T_i/T_e are consistent with being lower than midplane T_i/T_e values which have been measured as $2 \rightarrow 6$ [80].

The corrections applied using Valsaque's modelling [65] give a good estimate

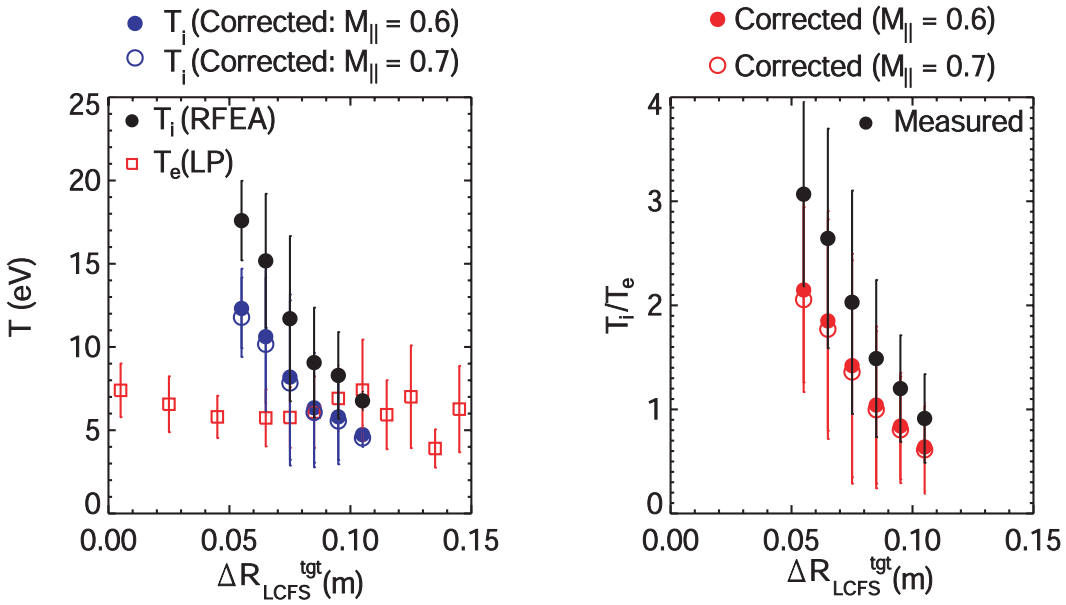

Figure 6.19: Inter-ELM H-mode T_i and T_e profiles as a function of ΔR^{tgt}_{LCFS} compared to corrected T_i profiles. Also shown is T_i/T_e at the target compared to corrected ratios.

for the real T_i at the target from experimental measurements by the target RFEA. Ideally to give an accurate correction, the flow at the target would be experimentally measured, however since this is not available, using modelling of the plasmas is the best estimate for $M_{||}$. The modelling by Valsaque et al [65] was designed to determine the correction needed for unidirectional RFEAs installed at the midplane of tokamaks. This means there may be limits for using this model for RFEAs close to the target. Since the RFEA intercepts the plasma above the sheath, in theory, the point at which the measurements are made is equivalent to a measurement made anywhere along the SOL. However, further modelling of RFEAs in the SOL using bounded targets would be beneficial to compare to the corrections determined from modelling by Valsaque. This will be investigated as part of further work with the RFEAs.

It should be noted that RFEA measurements of ions released from ELMs are also subject to errors in the presence of parallel SOL flows. Currently there is no simple method to estimate the flow at the target in MAST during an ELM, therefore the RFEA measurements in section 5.4 have not been corrected. Since the target measurements are facing the flows to the target, RFEA measurements of particles released by ELMs are likely to be overestimates.

6.3 Summary

Modelling of an L-mode and an inter-ELM H-mode discharge has been performed using the 1D SOL code SOLF1D. The L-mode modelling produced target profiles similar to those measured by the RFEA, however of the three upstream models for T_i used for comparison, $T_i = T_e$ gave the best match to experimental measurements.

This is not consistent with measurements made with the RFEA upstream where $T_i \sim 2T_e$, however limits in the 1D model may be the reason SOLF1D does not match experimental measurements well. H-mode modelling gave reasonable matches to the measured target profiles when the upstream T_i model was produced using $(T_i/T_e)^{up} = (T_i/T_e)^{tgt}_{exp}$. This is consistent with experimental measurements of T_i and T_e made upstream in the same discharge by RFEA and TS respectively [80]. J_{sat} measurements did not match in inter-ELM H-mode modelling which is again likely related to the lack of cross field transport in the SOLF1D model. The most important results from SOLF1D modelling was an estimate of $M_{\|}$ at the RFEA which is needed to improve the accuracy of T_i measurements.

In the presence of SOL flows, experimental measurements by RFEA probes can overestimate the real local T_i. Modelling by Valsaque et al has determined a correction for T_i measured by RFEA as a function of parallel flow, $M_{\|}$, at the entrance to the RFEA probe. Using $M_{\|}$ predicted by SOLF1D a correction for the L-mode and inter-ELM H-mode discharges has been determined. Applying the appropriate corrections to the RFEA measurements, in the range $0.65-0.7$, reduces T_i at the target so that in L-mode $T_i/T_e \leq 1$ and in inter-ELM H-mode $T_i/T_e = 0.6-2$. These corrections give a good indication of the experimental T_i at the target however real measurements of the parallel SOL flow at the target and more sophisticated modelling of RFEA measurements in a bounded SOL would be needed to give the most reliable correction to the experimental RFEA T_i measurements.

Chapter 7

Conclusions and future work

7.1 Conclusions

Knowledge of the ion temperature (T_i) at the edge of tokamak devices is important for determining heat and power exhaust and also potential damage to plasma facing components. The limited number of measurements available for T_i compared to the electron temperature (T_e) in the scrape-off layer of tokamaks have shown that often $T_i > T_e$. This will have implications for the derivation of quantities from experimental measurements and modelling which often assumes ions and electrons to be thermally coupled in the scrape-off layer (SOL).

Retarding field energy analysers (RFEA) are considered the most suitable diagnostic for measurements of the ion temperature in the tokamak SOL. MAST has been equipped with RFEA probes at the midplane and the target. An RFEA based on the design of the RFEA used at Tore Supra, CEA in Cadarache, France has been installed on the MAST reciprocating probe (RP) and commissioned. The operation of the probe was developed in order to measure radial profiles of T_i in steady state. A further RFEA was designed for use on the existing divertor science facility (DSF) system which allows the RFEA to measure T_i at the divertor target. The divertor RFEA was installed and commissioned to allow measurements to be made at the target. These diagnostics have been successfully used on MAST to measure T_i in a varied range of plasma conditions including low confinement (L-mode), during edge localised modes (ELM) and in inter-ELM high confinement (H-mode) plasmas. These measurements have been compared to measurements of T_e from other diagnostics such as Langmuir probes (LP) situated at the target and Thomson scattering (TS) measurements at the midplane of the plasma.

Measurements made of T_i by RFEA at the midplane in L-mode plasmas have shown that $T_i \sim 2T_e$ when no additional neutral beam heating is used. Measurements made at the target show $T_i \sim T_e$, which is consistent with OSM modelling and previous measurements at the midplane on MAST. In ohmic L-mode plasmas T_i has been found to reduce with increased core plasma density which is consistent with predicted pressure balance in the SOL. The plasma current has not been found

to give a noticeable scaling with T_i, however including beam heating in L-mode plasmas up to $P_{NBI} = 2$ MW has shown a stronger increase in T_i than T_e. T_i was found to scale with increasing power into the SOL. When additional heating was used in L-mode, $T_i \sim 2T_e$ was found at the target, suggesting that either neutral beam heating produces a source of hot ions or electrons and ions become less thermally coupled at the higher temperatures.

The heat flux at the divertor has been measured in L-mode using infra-red (IR) thermography camera data and LP data using the assumption $T_i = T_e$. Both diagnostic methods match well, which is consistent with T_i measurements by RFEA that confirmed $T_i \sim T_e$ in ohmic L-mode. This is also consistent with power balance which is found on MAST in L-mode using LP at all four strike points. In inter-ELM H-mode, power balance is not found when $T_i = T_e$ is assumed, suggesting $T_i > T_e$. Comparing IR data and LP measurements, assuming $T_i = T_e$, there is a discrepancy between the diagnostic methods which can be accounted for at the strike point when $T_i/T_e \sim 3$ is used. This is consistent with measurements made by RFEA in a range of inter-ELM H-mode scenarios which show $T_i/T_e = 1 \rightarrow 3$ in the range $\Delta R^{tgt}_{LCFS} =$ 0.02 - 0.15 m at the target. At a particular radial position at the target, T_i/T_e has been seen to scale with the connection length in the SOL, because longer connection lengths allow a longer distance for ions and electrons to thermally equilibrate. The equilibration of ions and electrons at the target has been determined for the range of plasma scenarios investigated which corresponds to the measurements of T_i/T_e made at the target. An inter-ELM H-mode plasma scenario in which upstream RFEA measurements of T_i were made showed $T_i/T_e = 2 \rightarrow 6$ which is consistent with target measurements of $T_i > T_e$.

First ELM T_i measurements at the target have been made by two different measurement techniques. T_i measurements of ions released from an average type III ELM have been made at two radial positions at the target. These showed that T_i in type III ELMs reduces with distance from the strike point, with temperatures of 30 eV and 60 eV. This method for the average ELM temperature gives an upper bound for T_i from an ELM since the temperature is determined from the maximum current at the RFEA. This measurement allows a comparison to the more developed ELM measurement technique which has also been studied. The fast swept ELM measurement technique allows T_i and V_s measurements to be taken on a timescale shorter than an ELM. RFEA measurements made of T_i from this method have shown peak temperatures of $T_i \sim 40$ eV in type I ELMs and $T_i \sim 35$ eV in type III ELMs. Measurements of V_s during the ELM are consistent with peaks in T_e measured by LP at the target and are evidence of hot electrons released by the ELM arriving at the target before hot ions and the remaining particles released by the ELM. The measurements made for both type I and type III ELMs are consistent with a simple model of the particles and energy released by an ELM arriving to the target and are comparable to both SOL modelling of ELMs and measurements

made on other tokamak devices.

Finally, the effect of SOL parallel flows has been considered because all measurements made by the RFEA are subject to inaccuracies in the presence of parallel flows. Corrections to two of the measured scenarios, one in L-mode and one in inter-ELM H-mode, have been made by previously known corrections determined for RFEA probes. Modelling of the two plasma scenarios has been carried out by SOLF1D in order to provide an estimate of the SOL parallel flow at the target RFEA entrance to allow a correction to be determined for the T_i measurements. The corrections applied to the ohmic L-mode measurements of ~ 66 % have shown that the corrected T_i would give $T_i \leq T_e$ at the target. In inter-ELM H-mode, similar corrections of ~ 68 % are applied to RFEA measurements which reduce the largest measurement of $T_i/T_e \sim 3$ to $T_i/T_e \sim 2$. Although these corrections are only an estimate, all measurements made by RFEA before correction should be taken as an upper limit on T_i and corrections of up to ~ 60 % may be necessary.

7.2 Future work

The work presented here are the first measurements of ion temperatures at the target in any plasma scenarios on MAST. However, although these allow new insights into the behaviours of the SOL, further measurements and studies are required.

An area which would particularly benefit the existing studies would be further radial measurements at the target. To facilitate such measurements improvements to the existing power supplies would be required to allow full profiles to be measured in all plasma scenarios. Specifically full radial profile measurements in higher density plasma discharges and inter-ELM H-mode measurements at the strike point would complete T_i data sets for steady state target plasmas. Further measurements in different magnetic configurations would also allow more information on the relationship between the connection length and T_i at the target. Further upstream measurements would be valuable since this would allow more comparisons between the upstream and target plasmas. Additionally, with improved power supply capabilities it would be possible to make more measurements of particles released by ELMs at the target.

Finally, more sophisticated evaluation of RFEA T_i measurements should be carried out. A measurement of the SOL parallel flow would be a valuable comparison to the estimate from SOLF1D modelling. Coherence imaging, now installed on MAST, which measures the flow of impurities in the divertor may allow an experimental comparison to the modelling estimates of the parallel flow at the RFEA entrance. Also the use of a bounded model of the SOL for determining the necessary correction for RFEA measurements in the presence of parallel flows would be beneficial as a comparison to the existing work on RFEA corrections to allow the best estimates of T_i to be obtained from the MAST RFEA diagnostics.

Bibliography

[1] D. Ward and S. Dudarev, "Economically competitve fusion," *Materials Today*, vol. 11, pp. 46–63, 2008.

[2] J. Wesson, *Tokamaks*. Oxford University Press, 2011.

[3] J. D. Lindl, R. L. McCroy, and E. M. Campbell, "Progress towards ignition and burn propagation in inertial confinement fusion," *Physics Today*, vol. 45, p. 32, 1992.

[4] C. M. Braams and P. E. Stott, *Nuclear Fusion: Half a century of Magnetic Confinement Fusion Research*, J. Navas, Ed. Institute of Physics, 2002.

[5] M. Hirsh *et al.*, "Major results from the stellarator Wendelstein 7-AS," *Plasma Phys. Control. Fusion*, vol. 50, p. 053001, 2008.

[6] V. P. Smirnov, "Tokamak foundation in USSR/Russia 1950-1990," *Nucl. Fusion*, vol. 50, p. 014003, 2010.

[7] R. A. Pitts *et al.*, "A full tungsten divertor for ITER: Physics issues and design status," *J. Nucl. Mater.*, vol. 438, pp. S48–S56, 2013.

[8] G. M. McCracken and P. E. Stott, "Plasma-surface interactions in tokamaks," *Nucl. Fusion*, vol. 19, p. 889, 1979.

[9] J. W. Coenen *et al.*, "Evolution of surface melt damage, its influence on plasma performance and prospects of recovery," *J. Nucl. Mater.*, vol. 438, pp. S27–S33, 2013.

[10] A. C. Darke, J. R. Harbar, and H. J. H, "MAST: a Mega Amp Spherical Tokamak," *in Proc. 18th Symp. on Fusion Technology (Karlsruhe,Germany)*, vol. 1, pp. 799–802, 1994.

[11] Y. Yang, G. F. Counsell, and the MAST team, "Observations with a mid-plane reciprocating probe in MAST," *J. Nucl. Mater.*, vol. 313-316, pp. 734–7, 2003.

[12] G. De Temmerman *et al.*, "Dust creation and transport in MAST," *Nucl. Fusion*, vol. 50, p. 105012, 2010.

[13] S. Elmore *et al.*, "Upstream and divertor ion temperature measurements on MAST by retarding field energy analyser," *Plasma Phys. Control. Fusion*, vol. 54, p. 065001, 2012.

[14] M. Kočan *et al.*, "Edge ion-to-electron temperature ratio in the Tore Supra tokamak," *Plasma Phys. Control. Fusion*, vol. 50, p. 125009, 2008.

[15] F. F. Chen, *Introduction to Plasma Physics and Controlled Fusion.* Springer, 2010.

[16] F. Wagner *et al.*, "Regime of improved confinement and high beta in neutral-beam-heated divertor discharges of the ASDEX tokamak," *Phys. Rev. Lett.*, vol. 49, pp. 1408–1412, 1982.

[17] R. A. Pitts *et al.*, "Far SOL ELM ion energies in JET," *Nucl. Fusion*, vol. 46, pp. 82–98, 2006.

[18] V. K. Gusev, F. Alladio, and A. W. Morris, "The basis of spherical tokamaks and progress in European research," *Plasma Phys. Control. Fusion*, vol. 45, pp. A59 – A82, 2003.

[19] A. Sykes *et al.*, "The spherical tokamak programme at Culham," *Nucl. Fusion*, vol. 39, pp. 1271–1282, 1999.

[20] M. Ono *et al.*, "Exploration of spherical torus physics in the NSTX device," *Nucl. Fusion*, vol. 40, p. 557, 2000.

[21] S. M. Kaye *et al.*, "Progress towards high performance plasmas in the National Spherical Torus Experiment (NSTX)," *Nucl. Fusion*, vol. 45, p. S168, 2005.

[22] H. Meyer *et al.*, "Overview of physics results from MAST," *Nucl. Fusion*, vol. 49, p. 104017, 2009.

[23] A. Darke *et al.*, "The MAST improved divertor," *Fusion Engineering and Design*, vol. 75-79, pp. 285–289, 2005.

[24] P. C. Stangeby, *The Plasma Boundary of Magnetic Fusion Devices.* Taylor & Francis Group, 2000.

[25] I. H. Hutchinson, *Principles of Plasma Diagnostics.* Cambridge University Press, 2005.

[26] G. De Temmerman *et al.*, "Thermographic study of heat load asymmetries during MAST L-mode discharges," *Plasma Phys. Control. Fusion*, vol. 52, p. 095005, 2010.

[27] N. J. Peacock *et al.*, "Measurements of the electron temperature by Thomson scattering in tokamak T3," *Nature*, vol. 224, pp. 488–490, 1969.

[28] A. W. DeSilva, "The evolution of light scattering as a plasma diagnostic," *Contrib. Plasma Phys.*, vol. 40, pp. 23–25, 2000.

[29] R. Scannell *et al.*, "Design of a new Nd:YAG Thomson scattering system for MAST," *Rev. Sci. Instrum.*, vol. 79, p. 10E730, 2008.

[30] G. Staudenmaier, P. Staib, and W. Poschenrieder, "Determination of ion temperatures in the edge plasma from ion flux transmission of apertures," *J. Nucl. Mater.*, vol. 93 &94, pp. 121–126, 1980.

[31] N. Asakura *et al.*, "SOL plasma profiles under radiative and detached divertor conditions in JT-60U," *J. Nucl. Mater.*, vol. 241-243, pp. 559–563, 1997.

[32] A. Huber *et al.*, "Spectroscopic measurements of the ion temperature profile in front of a limiter in TEXTOR-94," *Plasma Phys. Control. Fusion*, vol. 42, pp. 569–578, 2000.

[33] M. Reich *et al.*, "Lithium beam charge exchange diagnostic for edge ion temperature measurements at the ASDEX Upgrade tokamak," *Plasma Phys. Control. Fusion*, vol. 46, pp. 797–808, 2004.

[34] M. Kočan *et al.*, "Ion temperature measurements in the tokamak scrape-off layer," *J. Nucl. Mater.*, vol. 363-365, pp. 1436–1440, 2007.

[35] A. S. Wan *et al.*, "Janus, a bidirectional, multifunctional plasma diagnostic," *Rev. Sci. Instrum.*, vol. 57, pp. 1542–1551, 1986.

[36] G. F. Matthews, "A combined retarding field analyser and E×B probe for measurement of ion and electron energy distribution in tokamak edge plasma," *J. Phys. D: Appl. Phys.*, vol. 17, pp. 2243–2254, 1984.

[37] R. A. Pitts, "Ion velocity distributions at the tokamak edge," *Phys. Fluids B*, vol. 3, pp. 2871–2876, 1991.

[38] S. Raychaudhuri, "Ion temperature measurement in the edge region of SINP tokamak by retarding field analyser," *Contrib. Plasma Phys.*, vol. 39, pp. 359–365, 1999.

[39] R. A. Pitts *et al.*, "Retarding field energy analyzer for the JET plasma boundary," *Rev. Sci. Instrum.*, vol. 74, p. 4644, 2003.

[40] A. Kirk *et al.*, "A comparison of mid-plane scrape-off-layer measurements with model predictions in MAST and the calculation of cross-field transport coefficients," *Plasma Phys. Control. Fusion*, vol. 46, pp. 1591–1603, 2004.

[41] M. Kočan *et al.*, "On the reliability of scrape-off layer ion temperature measurements by retarding field analyzers," *Rev. Sci. Instrum.*, vol. 79, p. 073502, 2008.

[42] P. Tamain *et al.*, "Ion energy measurements in the scrape-off layer of MAST using a retarding field analyzer," *J. Nucl. Mater.*, vol. 415, pp. S1139–42, 2011.

[43] M. Kočan *et al.*, "First measurements of edge localized mode ion energies in the ASDEX Upgrade far scrape-off layer," *Plasma Phys. Control. Fusion*, vol. 53, p. 065002, 2011.

[44] M. Kočan *et al.*, "Elm ion energies in the ASDEX Upgrade far scrape-off layer," *Proceedings - 38th EPS conference on Controlled Fusion and Plasma Physics*, p. P2.072, 2011.

[45] M. Kočan *et al.*, "Ion energies and currents of type I and mitigated ELMs in the ASDEX Upgrade far scrape-off layer," *Nucl. Fusion*, vol. 52, p. 023016, 2012.

[46] M. Kočan *et al.*, "Ion temperature fluctuations in the ASDEX Upgrade scrape-off layer," *Plasma Phys. Control. Fusion*, vol. 54, p. 085009, 2012.

[47] M. Kočan *et al.*, "Inter-ELM ion transport in the ASDEX Upgrade far scrape-off layer," *Contrib. Plasma Phys.*, vol. 53, pp. 22–26, 2013.

[48] D. Brunner *et al.*, "Scanning retarding field analyzer for plasma profile measurements in the boundary of the Alcator C-Mod tokamak," *Rev. Sci. Instrum.*, vol. 84, p. 033502, 2013.

[49] M. Kočan *et al.*, "Measurements of ion energies in the tokamak plasma boundary," *J. Nucl. Mater.*, vol. 415, pp. S1133–1138, 2011.

[50] F. Matthews, G, "Plasma detachment from divertor targets and limiters," *J. Nucl. Mater.*, vol. 220-222, pp. 104–116, 1995.

[51] A. Loarte *et al.*, "Plasma detachment in JET Mark I divertor experiments," *Nucl. Fusion*, vol. 38, p. 331, 1998.

[52] M. Kočan, "Ion temperature measurements in the scrape-off layer of the tore supra tokamak," Ph.D. dissertation, L'Université Henri Poincaré, Nancy, 2009.

[53] S. Elmore *et al.*, "Scrape-off layer ion temperature measurements at the divertor target in MAST by retarding field energy analyser," *J. Nucl. Mater.*, vol. 438, pp. S1212 – S1215, 2013.

[54] D. Reiter, "Progress in two-dimensional plasma edge modelling," *J. Nucl. Mater.*, vol. 196-198, pp. 80–89, 1992.

[55] R. Schneider *et al.*, "B2-EIRENE simulation of ASDEX and ASDEX-Upgrade scrape-off layer plasmas," *J. Nucl. Mater.*, vol. 196-198, pp. 810–815, 1992.

[56] E. Havlícková *et al.*, "Benchmarking of a 1D scrape-off layer code SOLF1D with SOLPS and its use in modelling long-legged divertors," *Plasma Phys. Control. Fusion*, vol. 55, p. 065004, 2013.

[57] E. Havlícková *et al.*, "Steady-state and time-dependent modelling of parallel transport in the scrape-off layer," *Plasma Phys. Control. Fusion*, vol. 53, p. 065004, 2011.

[58] D. Brunner and B. LaBombard, "Surface thermocouples for measurement of pulsed heat flux in the divertor of the Alcator C-Mod tokamak," *Rev. Sci. Instrum.*, vol. 83, p. 033501, 2012.

[59] M. A. Lieberman and A. J. Lichtenberg, *Principles of Plasma Discharges and Material Processing.* Wiley, 1994.

[60] P. Tamain *et al.*, "Edge turbulence and flows in the presence of resonant magnetic perturbations on MAST," *Plasma Phys. Control. Fusion*, vol. 52, p. 075017, 2010.

[61] D. M. Planck, *The Theory of Heat Radiation.* P. Blakiston's Son & Co., 1914.

[62] A. Thornton, "The impact of transient mitigation schemes on the MAST edge plasma," Ph.D. dissertation, University of York, 2011.

[63] A. Herrmann *et al.*, "Energy flux to the ASDEX-Upgrade divertor plates determined by thermography and calorimetry," *Plasma Phys. Control. Fusion*, vol. 37, pp. 17–29, 1995.

[64] R. Nachtrieb, B. LaBombard, and E. Thomas, "Omegatron ion mass spectrometer for the Alcator C-mod tokamak," *Rev. Sci. Instrum.*, vol. 71, pp. 4107–18, 2000.

[65] F. Valsaque *et al.*, "Kinetic simulations of ion temperature measurements from retarding field analyzers," *Phys. Plasmas*, vol. 9, pp. 1806–1814, 2002.

[66] R. A. Pitts *et al.*, "Retarding field analyser measurements in the JET plasma boundary," *Proceedings - 30th EPS conference on Controlled Fusion and Plasma Physics*, vol. 27A, pp. P–2.84, 2003.

[67] H. Y. Guo *et al.*, "Ion temperature measurements in JET boundary plasmas using a retarding field analyser," *Contrib. Plasma Phys.*, vol. 36, pp. S81–86, 1996.

[68] R. Nachtrieb, "Ion mass spectroscopy on the Alcator C-Mod tokamak," Ph.D. dissertation, University of Illinois, 1993.

[69] T. Eich *et al.*, "Inter-ELM power decay length for JET and ASDEX Upgrade: Measurement and comparison with heuristic drift-based model," *Phys. Rev. Lett.*, vol. 107, p. 215001, 2011.

[70] A. Kirk *et al.*, "Filament structures at the plasma edge on MAST," *Plasma Phys. Control. Fusion*, vol. 48, pp. B433–B441, 2006.

[71] G. L. Squires, *Practical Physics.* Cambridge University Press, 2001.

[72] A. Kirk *et al.*, "Evolution of the pedestal on MAST and the implications for ELM power loadings," *Plasma Phys. Control. Fusion*, vol. 49, pp. 1259–75, 2007.

[73] L. C. Appel *et al.*, "A unified approach to equilibrium reconstruction," *Proceedings - 33rd EPS conference on Controlled Fusion and Plasma Physics*, pp. P–2.160, 2006.

[74] L. L. Lao *et al.*, "Reconstruction of current profile parameters and plasma shapes in tokamaks," *Nucl. Fusion*, vol. 25, pp. 1611–1622, 1985.

[75] R. A. Pitts, "Ion energy, sheath potential and secondary electron emission in the tokamak edge," Ph.D. dissertation, University of London, 1991.

[76] G. F. Matthews *et al.*, "Edge ion analysis in DITE," *Nucl. Fusion*, vol. 31, p. 1495, 1991.

[77] P. Bogen *et al.*, "Spectroscopic measurements of the ion temperature in front of a tokamak limiter," *J. Nucl. Mater.*, vol. 220-222, p. 472, 1995.

[78] V. Basiuk *et al.*, "Stuides of suprathsupra electron loss in the magnetic ripple of tore supra," *Nucl. Fusion*, vol. 41, p. 477, 2001.

[79] W. Fundamenski *et al.*, "Dissipative processes in interchange driven scrape-off layer turbulence," *Nucl. Fusion*, vol. 47, p. 417, 2007.

[80] S. Y. Allan *et al.*, "Ion energy measurements on MAST using a midplane RFEA," *J. Nucl. Mater.*, vol. 438, pp. S1192 – S1195, 2013.

[81] A. Kirk *et al.*, "ELM characteristics on MAST," *Plasma Phys. Control. Fusion*, vol. 46, pp. 551–572, 2004.

[82] A. Kirk *et al.*, "Structure of ELMs in MAST and the implications for energy deposition," *Plasma Phys. Control. Fusion*, vol. 47, pp. 315–333, 2005.

[83] D. Tskhakaya *et al.*, "PIC simulations of ELM particles and heat loads to the JET divertor targets," *Proceedings - 34th EPS conference on Controlled Fusion and Plasma Physicso*, vol. 31F, pp. O–2.002, 2007.

[84] A. Bergmann, "Transport of edge-localized mode energy in a scrape-off layer in the presence of collisionless fast electrons," *Nucl. Fusion*, vol. 42, pp. 1162–1167, 2002.

[85] W. Fundamenski, R. A. Pitts, and J. E. contributors, "A model of ELM filament energy evolution due to parallel losses," *Plasma Phys. Control. Fusion*, vol. 48, pp. 109–156, 2006.

[86] S. Jachmich *et al.*, "Divertor particle and power deposition profiles in JET ELMy H-mode discharges," *J. Nucl. Mater.*, vol. 363-365, pp. 1050–1055, 2007.

[87] R. A. Pitts *et al.*, "ELM driven divertor target currents on TCV," *Nucl. Fusion*, vol. 43, pp. 1145–1166, 2003.

[88] A. Herrmann *et al.*, "Stationary and transient divertor heat flux profiles and extrapolation to ITER," *J. Nucl. Mater.*, vol. 313-316, pp. 759–767, 2003.

[89] J. Harrison *et al.*, "Interpretive modelling of scrape-off plasmas on the MAST tokamak," *J. Nucl. Mater.*, vol. 390-391, pp. 392–394, 2009.

[90] R. D. Monk *et al.*, "Determination of JET scrape-off layer transport coefficients using an interpretive "onion-skin" plasma model," *J. Nucl. Mater.*, vol. 220-222, p. 612, 1995.

[91] A. Kirk *et al.*, "Parallel SOL transport in MAST and JET: the impact of the mirror force," *Plasma Phys. Control. Fusion*, vol. 45, pp. 1445–1463, 2003.

[92] J. Harrison, "Characterisation of detached plasmas on the mast tokamak," Ph.D. dissertation, University of York, 2010.

[93] A. Loarte, "Effects of divertor geometry on tokamak plasmas," *Plasma Phys. Control. Fusion*, vol. 43, pp. R183–R224, 2000.